# Modeling radiation on Mars for solar particle events and galactic cosmic rays

by

Michael Paul Pfeifer

B.S., Kansas State University, 2016

---

A THESIS

submitted in partial fulfillment of the
requirements for the degree

MASTER OF SCIENCE

Department of Mechanical and Nuclear Engineering
Carl R. Ice College of Engineering

KANSAS STATE UNIVERSITY
Manhattan, Kansas

2019

Approved by:

Major Professor
Dr. Amir A. Bahadori

# Copyright

# Abstract

Using the PHITS code system, Monte Carlo simulations of solar particle events (SPEs) and galactic cosmic rays (GCRs) were performed. The SPE model uses tally data to form kernel response functions that determine twelve different particle fluences when folded with measured solar spectra. A database of 577 solar events was analyzed to determine the probability and intensity of a large-scale event. As a shielding benchmark, the largest recorded SPE of October 19, 1989, was considered for absorbed dose and effective dose estimates. Since solar energetic particles have a high flux in the low energy domain, surface altitude makes a large difference in the dose received. To capture these effects, 11 locations on the Martian surface were simulated with special focus on the Hellas Planitia, Datum, and Olympus Mons. Simulation showed that the October 1989 SPE would have delivered an effective dose of 153 mSv at the Hellas Planitia, 230 mSv at the Datum, and up to 1 Sv at Olympus Mons. It was determined that unshielded dose rates at high altitudes could put astronauts in jeopardy of reaching their lifetime effective dose limits, 30 d organ absorbed dose limits, and could possibly cause acute radiation sickness. To minimize these risks, subterranean shelters using regolith as a passive shield were investigated. It was found that 25 cm of Martian regolith is enough shielding to reduce proton absorbed dose rates by more than 75% bringing absorbed dose and effective dose to tolerable levels.

A second model exploring dose rates for GCRs was also created to provide the full picture of the Mars radiation environment. The GCR source term was based on measured particle data from March 1, 2018, to July 1, 2018, which included particles ranging from protons to fully-stripped nickel ions. The geometry consisted of concentric spheres of true Mars size with density discretizations following atmospheric profiles defined by the NASA Glenn Research Center. A surface tally and volumetric tally were positioned at a column depth of $20\,\mathrm{g\,cm^{-2}}$, which is the average column depth measured by the Curiosity rover in the March to July 2018

time frame. An averaged flux density was tallied and converted to dose using coefficients defined in ICRP Publication 123 *"Assessment of Radiation Exposure of Astronauts in Space"*. It was found that GCRs are estimated to deliver 215.8 µGy of absorbed dose per day. The effective dose was calculated to be 491 µSv per day. For validation of these results, a surface crossing tally that estimated the particle flux within 30° from the zenith was compared to Mars Science Laboratory Radiation Assessment Detector (MSLRAD) data. It was found that the radiation flux for light ions had relatively good agreement with measured data. The integral particle fluxes were also shown to agree with measured data for protons and nuclei larger than boron.

# Table of Contents

# List of Figures

# List of Tables

# Acknowledgments

I would like to thank my advising professor Dr. Amir A. Bahadori for his support and guidance throughout this project. I would also like to thank Dr. William Dunn, Dr. Jeremy Roberts, and Dr. Kenneth Shultis for serving on my supervisory committee, and for their guidance throughout the years regarding radiation protection.

I would like to thank Rajarshi Pal Chowdhury, Luke Stegeman, and Faisal Ahmed Alghamdi for their help in simulation efforts.

I would also like to acknowledge Dr. Tatsuhiko Sato for his work on the Particle and Heavy Ion Transport code System (PHITS), his work on PHITS-based Analytical Radiation Model in the Atmosphere (PARMA), and for providing fluence to dose conversions coefficients which helped inspire this research.

I would like to thank Dr. Don Hassler for inviting us to the second Mars Radiation Modeling Workshop, Dr. Daniel Matthiae for providing source spectra for cosmic rays, and Dr. Dan Fry for providing the solar fluence database.

Lastly, I would like to thank my family and friends for their support throughout the completion of this degree.

RAD is supported by NASA (HEOMD) under Jet Propulsion Laboratory (JPL) subcontract 1273039 to Southwest Research Institute and in Germany by the German Aerospace Center (DLR) and DLRs Space Administration grants 50QM0501, 50QM1201, and 50QM1701 to the Christian-Albrechts-Universitt zu Kiel. Data supporting RAD are archived in the NASA Planetary Data Systems Planetary Plasma Interactions Node at the University of California, Los Angeles. The archival volume includes the full binary raw data files, detailed descriptions of the structures therein, and higher-level data products in human-readable form. The PPI node is hosted at the following URL: http://ppi.pds.nasa.gov/.

# Chapter 1

# Introduction

## 1.1 Space Radiation

The ionizing radiation environment in space is much different from the neutron and photon radiation typically dealt with on Earth in that it is comprised primarily of proton radiation, alpha particles, and a small fraction of high atomic number, high energy particles referred to as HZE particles. On the surface of Earth, the electromagnetic field produced by the rotation of Earth's core is able to significantly reduce the amount of ionizing radiation by deflecting charged particles away from the path of Earth's atmosphere. Additionally, the Earth has a relatively thick atmosphere of approximately $1000\,\mathrm{g\,cm^{-2}}$ that is able to provide additional passive shielding from primary radiation. While this is enough to reduce levels of ionizing radiation to safe levels on Earth, the radiation environment becomes exceedingly dangerous in high-orbit, deep space, or on another planet, or satellite body.

Mars is often regarded as the next frontier for space travel with the first crewed mission to Mars anticipated some time in the 2030s.[1] Due to a thin atmosphere and lack of a consistent magnetic field, the radiation environment on Mars is much harsher than that on Earth's surface.[2] Additionally, when radiation from solar particle events (SPEs) and galactic cosmic rays (GCRs) enters the thin Martian atmosphere, a cascade of secondary or higher orders of radiation, known as atmospheric showering[3], can occur. These atmospheric showers increase

the particle flux in the low energy domain, which may cause increased radiation absorbed dose with altitude, and at the surface of Mars. Elevated radiation levels could put astronauts on Mars at high risk to develop short-term and long-term health effects such as acute radiation sickness or cancers.[4]

NASA has imposed many radiation limits for astronauts to minimize the risk of developing adverse health effects. These include career limits, short term absorbed dose limits, and individual organ dose limits. Career limits are set based on the astronaut's age and sex corresponding to a 3% lifetime excess risk of cancer mortality at the upper 95% tolerance limit. For younger astronauts, the career dose limits are reduced since large amounts of radiation early in their career could lead to the development of health effects later in their life time.[5] Career dose limits are shown in Table 1.1. To put these values into perspective, an astronaut will on average receive 80 mSv of radiation dose in a six month stay in the International Space Station (ISS) during solar maximum, and 160 mSv for a six month stay during solar minimum.[5] It is also predicted that an astronaut could receive around 1200 mSv of exposure for a three year long mission to Mars.[5] NASA also has imposed non-cancer standards on the radiation absorbed dose allowed for certain organs. These organs include the eye lens, to reduce the risk of cataracts; blood forming organs, to reduce the risk of nausea, vomiting, and fatigue; and the skin, heart, and central nervous system, to prevent risks of degenerative tissue diseases such as dementia, stroke, or coronary heart disease.[6] The limits for organ absorbed dose weighted for relative biological effectiveness for important organs of interest is given in Table 1.2.

| Age (Years) | Male | Female |
|---|---|---|
| 25 | 700 mSv | 400 mSv |
| 35 | 1,000 mSv | 600 mSv |
| 45 | 1,500 mSv | 900 mSv |
| 55 | 3,000 mSv | 1,700 mSv |

**Table 1.1**: *Career effective dose limits set by NASA based on age and gender corresponding to a 3% increase in excess cancer risk.*[7]

| Organ | 30 d limit mGy-Eq | 1 y limit mGy-Eq | Career limit mGy-Eq |
|---|---|---|---|
| Lens | 1,000 | 2,000 | 4,000 |
| Skin | 1,500 | 3,000 | 6,000 |
| Blood-forming organs | 250 | 500 | 1,000-4,000 |
| Heart | 250 | 500 | 1,000 |
| Central Nervous System | 500 | 1,000 | 1,500 |

**Table 1.2**: *Non-cancer forming absorbed dose limits for organs of interest.*[8]

To understand the significance of NASA-defined absorbed dose and effective dose limits, it is important to understand the difference between SPEs and GCRs. For career dose limits, GCRs are of interest because they are difficult to shield, always present, and will contribute most of the dose over the course of a space mission. For organ absorbed dose limits, however, SPEs are typically of interest since they can deliver high amounts of dose in a relatively short amount of time, possibly leading to acute radiation sickness. This SPE and GCR behavior is demonstrated in radiation measurements by the Mars Science Laboratory Radiation Assessment Detector (MSLRAD) shown in Figure 1.1. It can be seen from the figure that the GCR dose remains relatively consistent over the year with slight dose fluctuations from diurnal cycles. It can also be seen that there was a weak solar event that increased the radiation dose on the surface by approximately $40\,\mu\text{Gy}\,\text{d}^{-1}$. While this is expected behavior, there are many factors that can greatly affect SPE and GCR dose. To explain these factors, previous studies of SPE and GCR dose on Mars were explored.

## 1.2 Solar Particle Events

SPEs are caused by irregularities in the complex magnetic field of the Sun when magnetic plasma reconnects causing nearby particles to accelerate to high energies. In a re-connection event, the Sun may produce a solar flare (acceleration of solar winds), a coronal mass ejection (CME)(emission of solar material), or both. Ninty nine percent of the particles accelerated by these events are protons, but they can also include small amounts of helium ions and occasional HZE particles. SPEs have been observed to fluctuate widely in their frequency

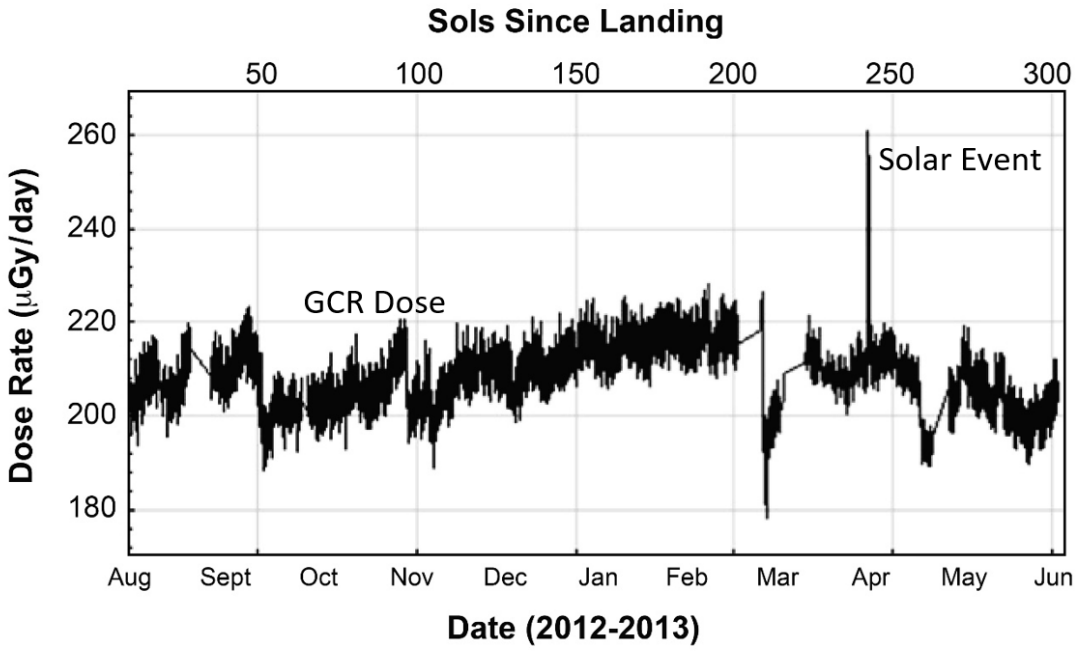


**Figure 1.1**: *Radiation measurement from Curiosity Rover showing diurnal cycles from GCR dose and dose increase for a SPE from https://www.nasa.gov/jpl/msl/ .*[9]

and intensity depending on the Sun's 11-year cycle. In this cycle, the number of sun spots occurring on the surface of the Sun will peak, indicating a solar maximum, or diminish, indicating a solar minimum. During solar minimum, CMEs have been observed to occur approximately once per day, and up to two or three times per day during solar maximum.[5] While the chance of a CME directly impacting Mars is relatively low, CMEs typically result in a harder spectrum of protons, at higher flux density, than solar flares. A few of the most noteworthy SPE events are shown in Figure 1.2. When these events occur, proton radiation has the greatest potential to penetrate the Martian atmosphere and cause biological or electronics damage. Based on the continuous slowing down approximation, primary protons will reach the surface at Gale Crater at a kinetic energy between 150 MeV and 200 MeV, where the range of protons is 17.8 g cm$^{-2}$ to 29.3 g cm$^{-2}$ in $CO_2$. This energy range is of interest, since the primary protons reaching the surface will be sufficiently slowed to deposit the remainder of their energy. Based on this observation, the transport should show that the maximum proton dose occurs within this energy range.

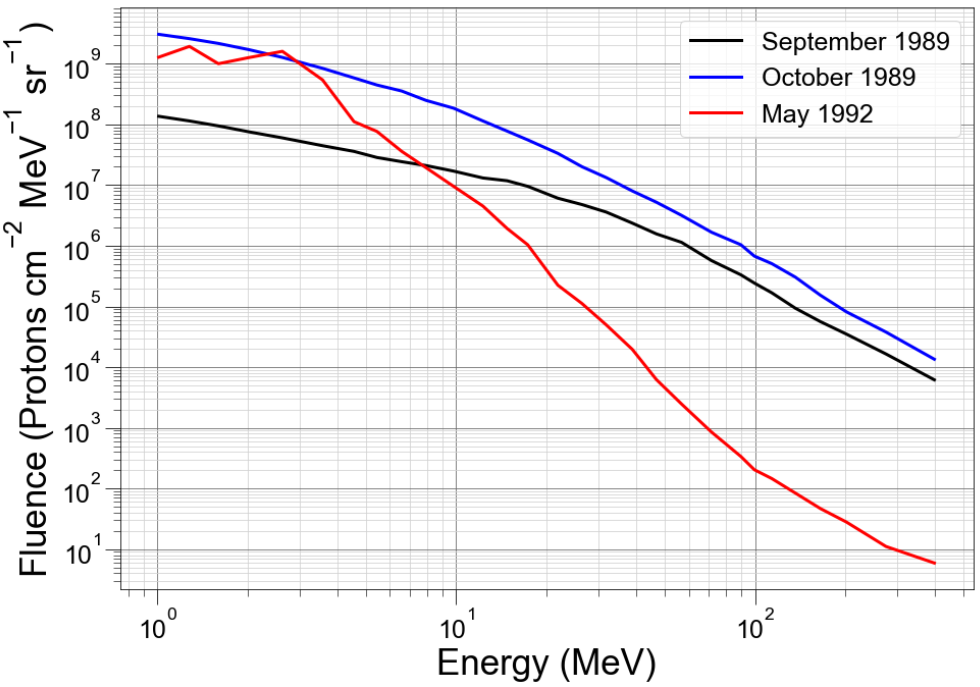


**Figure 1.2**: *Examples of three measured large SPE events.*

The preceding prediction has been confirmed in previous simulations of the Martian radiation environment. A study by Dr. Jingnan Guo and others[10] used the NASA space radiation deterministic transport code HZETRN[11] to transport fluence spectra of large SPEs at Gale Crater and found that the majority (>90%) of surface dose is due to primary protons between 100 MeV and 800 MeV. Source protons transported with kinetic energies greater than 10 GeV were also found to give negligible contribution to surface dose for all simulated particles. It was also found that for the October 1989 event, the downward proton absorbed dose rate was nearly 100 times greater than that of a solar quiet period. At this rate, at the Hellas Planitia surface, it would take a large SPE exposure 40 days for an unshielded astronaut to reach their career limit. This study concluded that it takes as little as 10 cm of Martian soil, also known as regolith, to provide adequate shielding for energetic particles.

Another study by Dr. Lawrence Townsend and others simulated large SPE spectra normalized to the Carrington event[12] fluence above 30 MeV, to understand the effects on the Mars radiation environment in the harshest solar conditions. In this study, dose was calculated for various thicknesses of aluminum shielding to determine the amount of shielding

necessary to minimize dose to acceptable levels for areal densities ranging from $2\,\mathrm{g\,cm^{-2}}$ to $30\,\mathrm{g\,cm^{-2}}$. The acceptable dose for these events is based on a 30 day dose limit, which is set to prevent acute radiation sickness effects over the life of a single SPE. This study concluded that $40\,\mathrm{g\,cm^{-2}}$ of aluminum is needed to shield astronauts on the Martian surface adequately. While this study has significance for short duration missions, particularly for a single SPE, a long-term mission with multiple SPEs could cause astronauts to reach yearly dose limits.

Other simulations using a now-deprecated, NASA-developed radiation transport code for light ions, BRYNTRN,[13] previously showed that for large SPE events, organ dose equivalents can range from 2 rem to 12 rem at the surface.[14] Monte Carlo simulations have also been performed with GEANT4[15] to produce differential flux spectra at the surface of Gale Crater and to estimate dose to a Biochip.[16] This study found that a single SPE can produce up to 3 Gy of absorbed radiation dose, which, for heavy charged particles, can greatly damage electronics. By finding the flux incident on the chip, shielding designs could be optimized to protect the integrity of the electronics. Another concern is whether dust storms will have a large impact on radiation absorbed dose. Simulations performed by Dr. Ryan Norman and others showed that dust storms have a minor impact on radiation dose received, usually within 10% of standard atmospheric conditions.[17] However, for the Carrinton Event, one of the largest events on record (1859),[18] variation was found to be up to 26% for deep atmospheric conditions.

## 1.3 Galactic Cosmic Rays

GCRs refer to all radiation that originates outside of the solar system. While the exact origins of GCRs are unknown, there is general consensus that these particles are accelerated by supernovae.[19] These particles are comprised roughly of 87% protons, 12% alpha particles, and 1% heavy ions,[20] and differ greatly from SPEs in that they are high energy and cannot be mitigated easily using passive shielding techniques. In fact, Dr. Tony Slaba and others found that aluminum shielding exceeding $50\,\mathrm{g\,cm^{-2}}$ can actually cause in increase in dose due to neutron build-up.[21] The intensity of GCRs at Mars depends highly on the modulation

of the solar magnetic field, which is directly correlated to the Sun's 11-year cycle.[22] This will cause an increase in GCR dose during solar minimum, and a decrease of GCR dose during solar maximum. Additional effects of the Martian environment such as seasonal changes and diurnal variations in Martian pressure will also cause differences in dose received at the Martian surface.

A study by Camron Gorguinpour and others in 2010 found that lifetime dose limits can be reached in as little as a year on Mars.[4] In order to minimize absorbed dose, using natural resources, the research performed shielding analysis which simulated a cliff-side habitat as a natural shield. It was found that such a habitat can reduce GCR dose by 40% and SPE dose by 50% with 10 cm of regolith shielding. This paper also found that annual whole body dose doubled during solar maximum as compared to solar minimum due to an increased contribution from SPEs and a decreased contribution for GCRs. This finding shows the radiation environment on Mars is unpredictable and that there can be trade-offs of scheduling a mission during solar minimum or maximum.

Other studies have shown that due to the high penetration power of GCRs, dose rate remains relatively constant for atmospheric depths greater than $10\,\mathrm{g\,cm^{-2}}$.[17] This is due to the lack of atmosphere, which does not provide sufficient material to cause spallation in the high flux regions of the GCR energy domain. This study also showed that dose profiles were unaffected by significant amounts of dust loading. This means that simulations between $10\,\mathrm{g\,cm^{-2}}$ to $22\,\mathrm{g\,cm^{-2}}$ should produce similar results and will not require additional simulation at other column densities. That being said, any variations within the incident particle spectra due to changes in solar activity will require a separate simulation to be performed. A 2016 GCR simulation using PHITS was performed at the first Mars Radiation Workshop in Boulder, Colorado,[23] and demonstrated accurate results when compared to MSLRAD. In 2018, a second Mars Radiation Modeling Workshop was held, in which the GCR contents of this thesis were presented. This model required a new set of modeling parameters, atmospheric parameters, and GCR source spectra for direct comparison with MSLRAD measurements taken in 2018.

## 1.4 Objective

Simulating the Mars radiation environment for these two radiation sources involves overcoming two substantial challenges. First, one must take into account changes in atmospheric density with altitude as well as changes in surface height and composition, to properly model the transport. Second, SPEs and GCRs are comprised of incident spectra of varying particle types and energies, which means that the model has to be flexible enough to apply to any source spectrum or particle type. Through appropriate implementation and some simplification, these challenges can be addressed to achieve accurate flux densites, fluences, or dose estimates. The radiation model discussed in this paper is constructed using the Particle and Heavy Ion Transport code System (PHITS) and largely follows previous work used to develop the PHITS-based Analytical Radiation Model in the Atmosphere (PARMA) to predict GCR dose anywhere and at any time for Earth.[3;24;25] The underlying Monte Carlo data for PARMA permit consideration of varying global parameters, such as geomagnetic shielding and boundary conditions, utilizing a library of data that can quickly be accessed. PARMA can thus be used to determine time-dependent dose rates to subjects as varied as airline crews and semiconductor devices.[24] Applying this modeling strategy to Mars, atmospheric and surface flux densities may be calculated, which can be used to improve radiation shielding for future crewed missions to the Martian surface and understand the threat of radiation effects on electronics, such as the drone on the Mars 2020 Rover.[26]

All of the studies previously cited agree that dose on Mars from SPEs can vary widely depending on the shape of the source spectra. It is also known that there can be large variations between Earth and Mars measured spectra for a single event. Therefore, there is a need to construct a flexible model that allows for efficient dose estimates for any specified SPE energy spectrum. This thesis describes a flexible radiation model constructed from forming kernel responses, that when scaled, provides dose estimates for any recorded events, at any of 11 surface locations. The simulations for each surface location tallies particle fluences in the upper atmosphere to a maximum altitude of 118 km above the Datum. Simulations also tallied particle fluences every 25 cm in Martian regolith to a maximum depth of 5.5 m.

These data will provide information about frequency of SPE doses as well as the shielding feasibility of a subterranean shelter. The data are organized into kernel responses for mono-energetic protons incident to the Martian atmosphere. These kernel responses are then scaled with measured solar data to represent a transported spectrum for the given event. By pre-selecting an event, surface location, and altitude relative to that surface, dose estimates may be quickly provided at any given location on Mars under normal atmospheric conditions.

While the SPE kernel data could be used for an incident GCR proton spectrum, the inclusion of heavy ions up to nickel makes it computationally expensive to make kernel responses for every particle type. For GCRs, particle spectra are finely discretized for particles ranging from protons to nickel and transported in their entirety. This model also includes just one surface location based on atmospheric measurements taken by the Curiosity rover. This allows for a direct comparison of particle results with the only measured radiation flux data on Mars to give validation to the modeling and methods. For both the SPE and GCR simulations, all of the transport was performed using PHITS.[27] This code is well known for being highly validated for its charged and neutral particle transport, its advanced radiation models, and has become a common tool in space radiation analysis.

# Chapter 2

# Radiation Transport Model

## 2.1 Structure of the PHITS Input File

PHITS is a Monte Carlo based program that parses an input deck for specific keywords and values which will tell the software how to perform calculations, construct the model geometry, and extract wanted radiation data. This input deck is a text file that consists of specific "cards" which each serve a function in the execution of the software. The cards used regarding this research are: parameters, source, material, surface, cell, volume, and tally. The parameters section in PHITS uses key words and values to tell the program which calculation models to use. The source card will define the distribution, energy, shape, and location of the irradiating source. The material section defines the composition of cells, and allows the program to calculate cross-section data for the particle transport. The surface card defines all surface boundaries of the problem geometry. The cell card defines the volume bodies enclosed by the surfaces and which materials and densities to use for the calculation. While volumes can be calculated by the program, they can also be defined in the volume card which is used with the tally card to calculate flux densities. Last, the tally card keeps track of how many particles are crossing a surface (T-cross), or the chord length of the particles in a volume (T-track), to calculate the flux rate for a specified region.

## 2.2 Solar Particle Event Model

### 2.2.1 PHITS Parameters

Within the PHITS input, calculation models should be set to optimize the radiation transport for the specific simulation. The cross-section libraries included in PHITS cover a large portion of the energy domain, and outside of this region where particles have exceedingly high or low energies, algorithms are used to simulate particle behavior and atomic reactions. For all simulations performed as part of this research, the standard calculation models were used. Cut-off energies for cross-section libraries are defined within the PHITS parameter card and are given in Table 2.1 for various particle types.

| **Particle** | **Minimum Energy (MeV)** | **Maximum Energy (MeV)** |
|---|---|---|
| Proton | $1.0 \times 10^{-3}$ | N/A |
| Neutron | $1.0 \times 10^{-10}$ | 20 |
| Photon | $1.0 \times 10^{-3}$ | $1.0 \times 10^{3}$ |
| Electron | 0.1 | $1.0 \times 10^{3}$ |
| Positron | 0.1 | $1.0 \times 10^{3}$ |
| Deuteron | $1.0 \times 10^{-3}$ | $3.0 \times 10^{3}$ |
| Triton | $1.0 \times 10^{-3}$ | $3.0 \times 10^{3}$ |
| $^{3}$He | $1.0 \times 10^{-3}$ | $3.0 \times 10^{3}$ |
| Alpha | $1.0 \times 10^{-3}$ | $3.0 \times 10^{3}$ |
| A>4 | $1.0 \times 10^{-3}$ | $3.0 \times 10^{3}$ |

**Table 2.1**: *Particle energy cut-offs for PHITS nuclear cross-section libraries.*

The nuclear cross-section cut-off energy for all hadrons except for neutrons was set to 1 keV, which is the lower limit of PHITS cross-section data. For neutrons, the lower limit was set to 0.1 meV, which is also the lower limit, to capture thermalization and albedo effects of the regolith. For hadrons between 1 MeV to 3 GeV intra-nuclear cascade and evaporation models (INCL4.6 and GEM respectively) are used with cross-section data to simulate spallation products and nucleus excitation.[28] For hadrons above 3 GeV, the Jet AA Microscopic Transport model (JAM) is used. This is a hadronic cascade model that paramaterizes a vast database of hadron-hadron cross-sections that are estimated based on resonance models and string models that fit experimental nuclear data.[29] For nucleus-nucleus

interactions, the JAERI Quantum Molecular Dynamics (JQMD) Model 2.0 was used. This model has the ability to simulate the time evolution of nuclear reactions using correlations between any combination of nucleons.[30] The elastic scattering, inelastic scattering, and total cross-section data for nucleon nucleus collisions was set to use Sato's formula. A figure showing the standard model, libraries, and the energy domains in which the models are used, is shown in Figure 2.1.

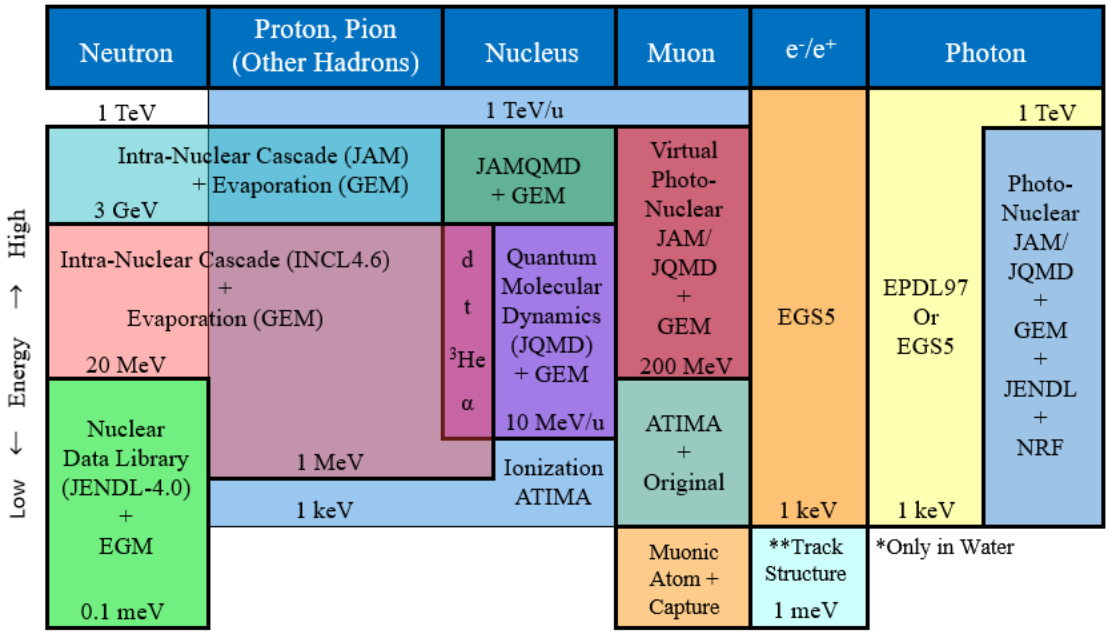


**Figure 2.1**: *PHITS models with switching energies and cross-section libraries recreated from manual.*[31]

All simulations were set to use the most recent version of the event generator mode (Ver. 2.0). This event generator simulates spallation events that result in the release of more than two hadrons. These daughter hadrons continue to be transported using Monte Carlo methods. Cross-section data for photon, electron, and positron transport were used instead of the Electron Gamma Shower (EGS5) algorithm. Due to the large number of secondary particles from spallation events, the maximum database size for PHITS algorithm of stopping power (ATIMA) was increased to 5000 interpolated values. For all runs, energy and angular straggling were turned off to avoid bugs in the code that flag errors. The random number generator seed was set to be based on the starting clock time. For all inputs, 5000 histories

were run per batch, with approximately 100 completed batches per run. It should be noted that all of the physics models have been tested and benchmarked in numerous studies.[32]

### 2.2.2 Atmospheric Model

The altitude dependence of SPEs is strongly influenced by the atmospheric model chosen. Atmospheric density profiles were compared with data from SPICAM,[33] Viking I lander,[34] Mars Global Reference Atmospheric Model (Mars GRAM),[35] and the Mars Climate Database (MCD).[36] The MCD model was ultimately chosen for SPE radiation transport due to coverage at high altitudes and because it is one of the most modern models. The atmospheric composition was taken from the On-Line Tool for Radiation Assessment in Space (OLTARIS).[37] This composition is given as 95.4% $CO_2$, 2.7% $N_2$, 1.6% Ar with trace amounts of $O_2$ and CO. To complete the MCD profile at low altitudes of $-7\,\mathrm{km}$ (Hellas Planitia), and for altitudes extending to 200 km (Martian Exosphere), the end points were logarithmically extrapolated. To smoothen the profile over its domain, the data were logarithmically interpolated between data points.

The geometry of the model consisted of true Mars-sized concentric spheres with the topographical Datum (averaged surface altitude) defined at a radius of 3389.5 km. By making the model true size, the spatial and angular dependence of the radiation transport can be preserved. The MCD atmospheric profile was discretized using a hybrid column density/altitude approach. Altitudes between 118 km and 18 km, had density discretization split every 5 km with the atmospheric density averaged over the given region. For altitudes less than 18 km the model was discretized by average column density in the region multiplied by the region thickness to a resolution of $1\,\mathrm{g\,cm^{-2}}$. This creates a model that captures the shape of the atmospheric profile while also creating finer discretization closer to our region of interest at the surface. A plot of the model density profile compared to the MCD profile is shown in Figure 2.2. Integrating the model into a cumulative distribution function shows that 99.99% of the atmosphere lies below 90 km, and that the relative error of the integrated column density is less than 1.43% for altitudes less than 90 km. These plots are shown in the left

and right hand sides of Figure 2.3 respectively.

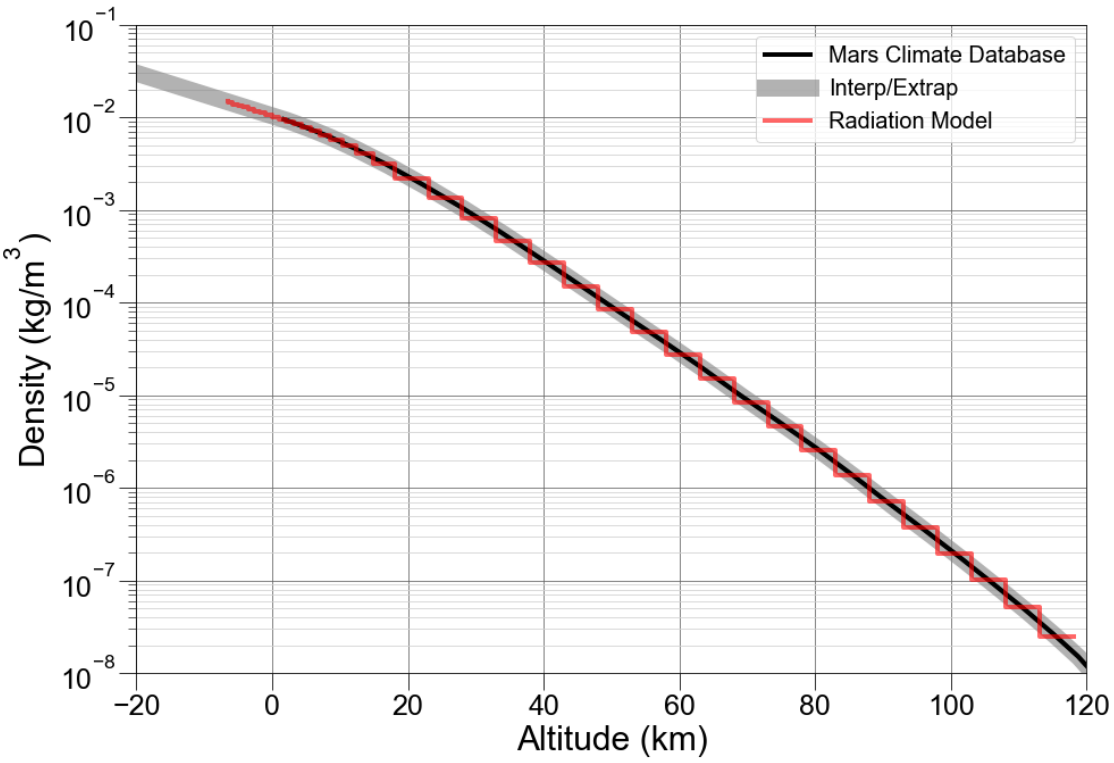


**Figure 2.2**: *Discretization in radiation model compared to interpolated and extrapolated data from Mars Climate Database.*

### 2.2.3 Regolith Model

The inner-most spheres of the radiation model consisted of 6 m of regolith followed by a graveyard region at the center. The regolith was discretized into regions 25 cm deep so that its shielding effects may be studied. The regolith composition was taken from OLTARIS as 51.2% $O_2Si$, 9.3% $Fe_2O_3$, 32.1% $Al_2CaK_2MgNa_2O_7$, and 7.4% $H_2O$ with a density of 1.7 g cm$^{-3}$. It should be noted that $Al_2CaK_2MgNa_2O_7$ was taken to be the "everything else" molecule which came from averages taken from three landing sites: the Viking 1 site, the Phoenix landing site, and the Mawrth Vallis site.[38] Using this composition greatly simplifies the model since the regolith may be treated as a uniform material. In order to capture albedo effects at different geographical locations, 11 "regolith cases" were considered as well as an infinite atmosphere case. The infinite atmosphere was taken to be the same atmospheric

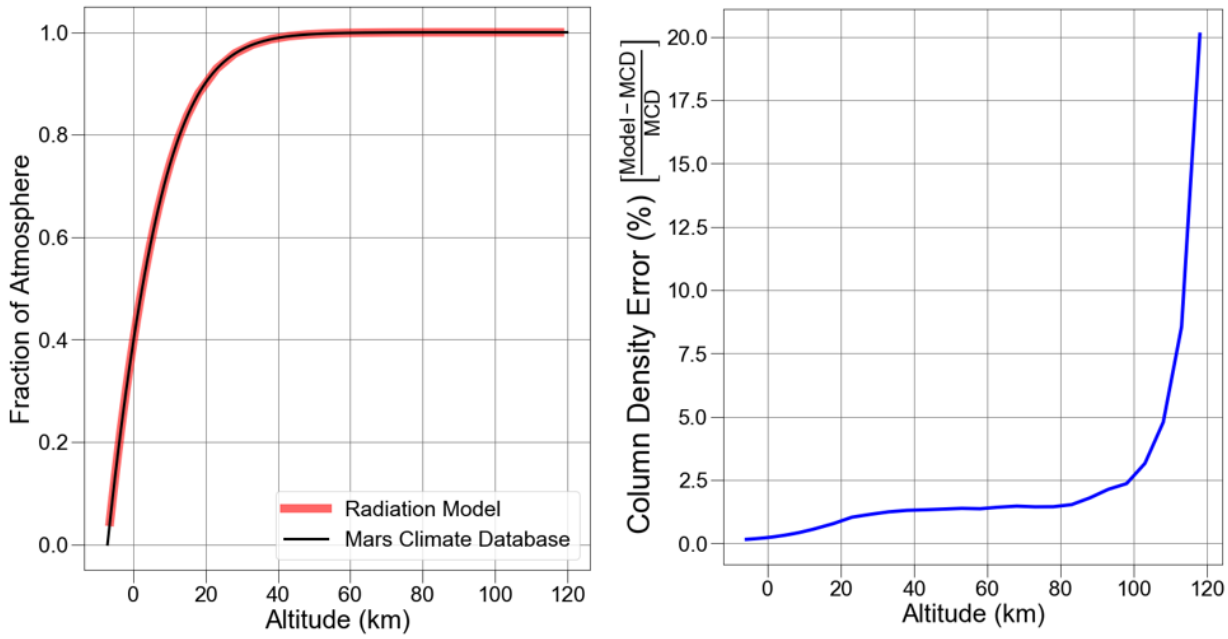


**Figure 2.3**: *Cumulative distribution showing fraction of atmosphere below altitude (left). Column density relative error between integrated MCD data and integrated radiation model with altitude (right).*

profile extending down to −10 km from the Datum. This case will give information about how the regolith albedo affects the spectrum and doses seen at the surface of Mars. The regolith cases consist of geometries of varying altitudes at which the surface of Mars is considered, ranging from the Hellas Planitia at −7 km to Olympus Mons at 23 km. Between these cases the atmospheric discretization method stays the same, while the total number of surfaces and volumes varies. To simplify presentation of the transport results, focus will be taken on three geographical locations: the Hellas Planitia (22.7 g cm$^{-2}$), the topographical Datum (13.7 g cm$^{-2}$), and Olympus Mons (1.6 g cm$^{-2}$). A diagram of the radiation model is shown in Figure 2.4

### 2.2.4 SPE Source Term and Solar Data

By the time solar energetic particles reach Mars, the protons will have gone through enough scattering off of magnetic field lines to allow for isotropic treatment of the source. Therefore, the radiation model constructed uses an isotropic spherical shell source (s=9

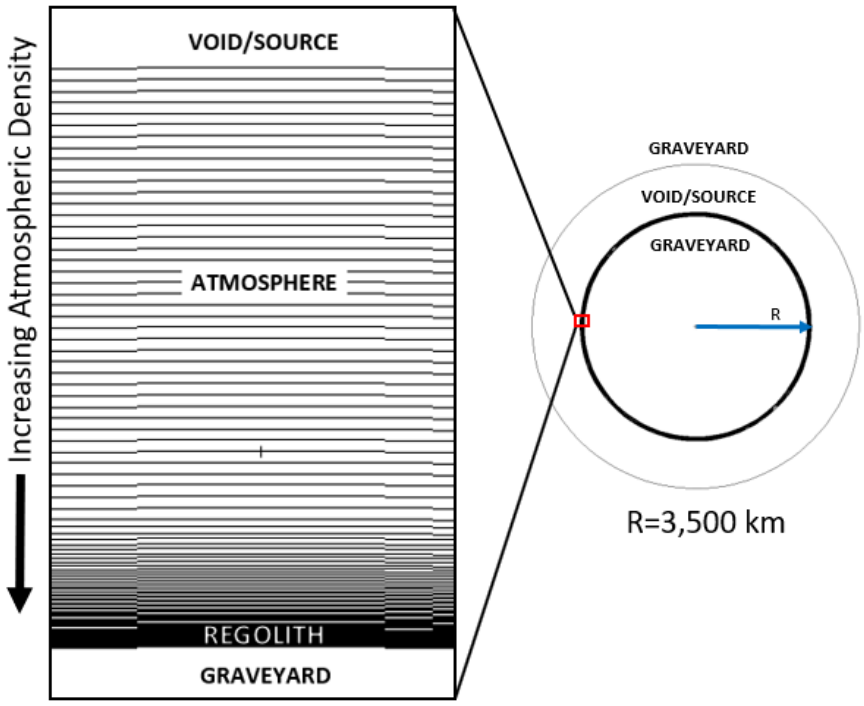


**Figure 2.4**: *Visualization of the Mars model cell/surface geometry.*

in PHITS) of mono-energetic protons. PHITS performs the sampling of a spherical shell by using a uniformly sampled plane tangent to the sphere of interest. This plane shares the same radius as the sphere and rotates about the sphere randomly in both polar and azimuthal angles $\theta$ and $\phi$. By considering all particles produced by the plane to be traveling inward perpendicular from the plane, the model effectively constructs a uniform spherical shell source. An example sketch of the source sampling is shown in Figure 2.5

The source was considered to be mono-energetic protons to produce source-normalized kernels that may be applied to incident SPE protons by multiplying the respective kernel result by an integrated fluence. Mono-energetic protons were made to have 50 discretizations spaced logarithmically between 1 MeV and 100 GeV to give 10 energy bins per decade. Encompassing the entire geometry, is a graveyard region that will force the program to stop tracking particles that escape this boundary. Between the graveyard and outer atmosphere where the source plane exists is a vacuum. A specialized multiplication factor in PHITS called "totfact" is defined as the area of the irradiating source plane. When applied, this factor removes area dependence on the source term giving units in number of particles emit-

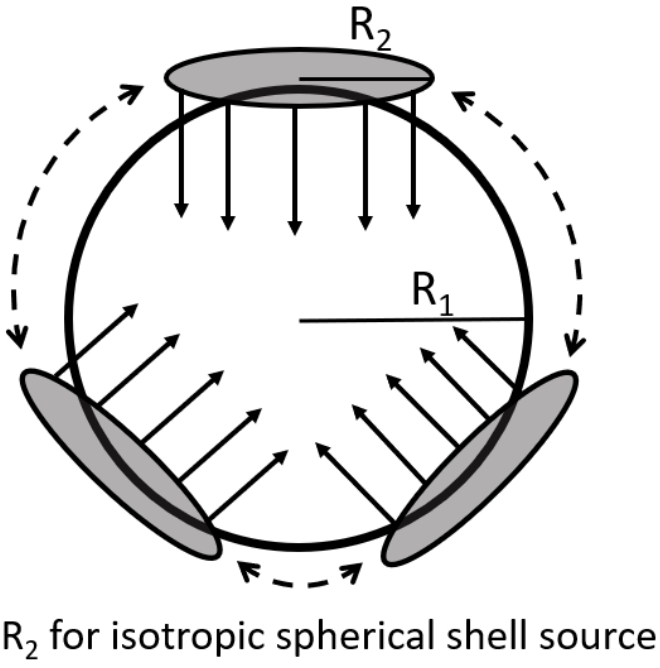


**Figure 2.5**: *Visualization of the Mars model source geometry recreated from PHITS manual.*[31]

ted from the source plane. This factor is important to remove area dependence on the Monte Carlo source term which would otherwise require a tally correction factor in the post processing phase.

### 2.2.5 Current Tally

Surface tallies were used to evaluate an incident angular current at the tally surfaces. These tally surfaces were inserted at the spatial midpoint between density discretizations in the atmosphere, at the surface, and every 25 cm within the regolith. The reason for tallying between discretizations is to accurately capture the back-scattering effects that happen within these regions. If this was not considered, the density increases between layers would lead to over estimation of back-scattering. The tallies were made to have six angular discretizations (every $\theta = 30°$) swept out in $2\pi$ to give solid angle in steradians. In total, 13 particle types were considered: proton, neutron, deuteron, triton, helium-3, alpha, electron, positron, muon+, muon-, pion+, pion-, and pion0. The minimum tally energy was set to

$10^{-3}$ MeV for protons, $10^{-8}$ MeV for neutrons, and 1 MeV for all other particles. The tally energy binning was set similar to the source term with 10 bins per logarithmic decade. Particles with similar mass were grouped into the same tally output files. For particles with more than 1 atomic mass unit, the tally energy binning was scaled to account for the particle kinetic energy, outputting results per unit energy with no nucleon dependence. To allow the program to convert the tally into the proper $cm^{-2}$ units, the cross-sectional area of each surface tally must be provided. By integrating out the solid angle dependence for each of the current tallies, particle fluences may be found to get the total number of particles crossing the surface per unit area.

### 2.2.6 Dose Conversion

To estimate absorbed dose and effective dose a human would receive at a given surface, fluence to dose conversion coefficients are used. These coefficients, calculated by developer of PHITS Tatsuhiko Sato, describe the dose a computational phantom would receive from an isotropic field of mono-energetic particles, for a large range of energies and particle types.[39] By scaling and re-binning tally data, individual organ dose equivalents or the effective doses a male or female would receive may be estimated for a given solar event and location. Unless specified, all examples in this thesis include the effective and absorbed dose for a male/female averaged phantom to describe an averaged radiation dose for both sexes. An example of effective dose conversion coefficients for protons, neutrons, electrons, and alpha particles is given in Figure 2.6. This currently is the most efficient way to provide dose estimates without the transport of a computational phantom. However, due to the forward scattering nature of atmospheric showering the field, will exhibit a superior to inferior (head to toe) radiation field for an astronaut standing on the surface. This means that these coefficients will introduce some inherent error which is not presently quantified. This may be addressed in future studies by transporting the fluence results near the surface for a computational phantom, greatly reducing run time when compared with simulating transport through the entire geometry of Mars and its atmosphere.

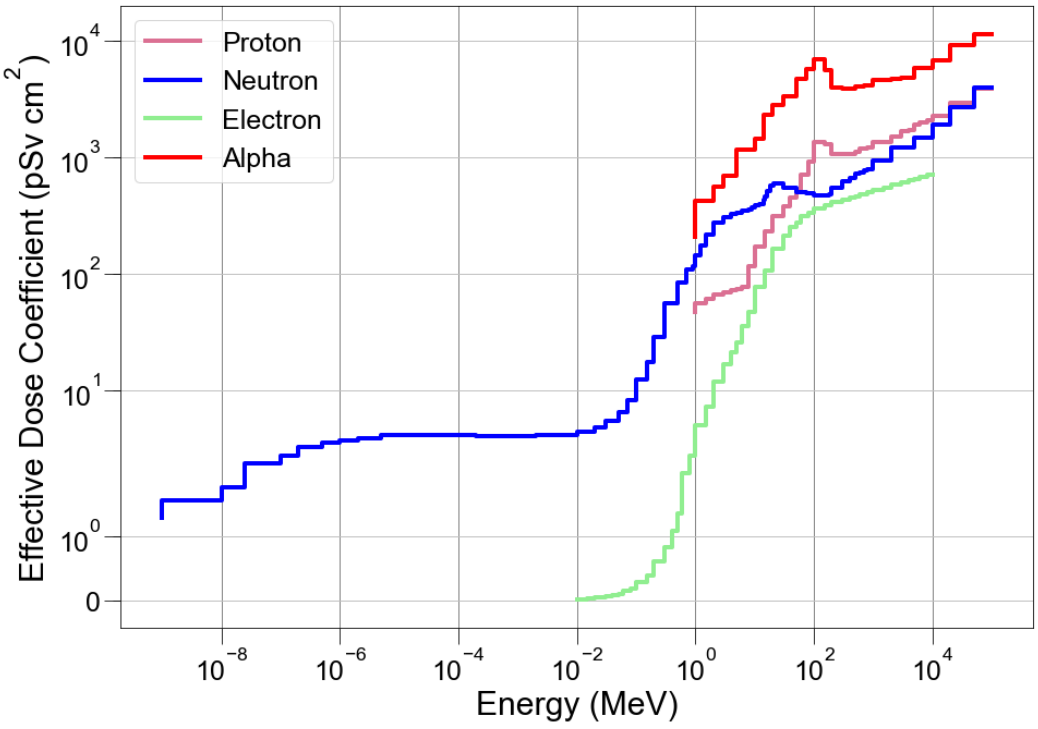


**Figure 2.6**: *Example of effective dose conversion coefficients for common particles.*

## 2.3 Galactic Cosmic Ray Model

### 2.3.1 PHITS Parameters

The PHITS parameter section for the GCR model is the same as discussed in section 2.1.1 with the addition of new features added in PHITS 3.08 beta which simplify the particle transport. Firstly, photons were considered in the GCR transport, so the Electron Gamma Shower Algorithm version 5.0 (EGS5) was turned on for this model. This algorithm was developed in 1985 and samples the particle distance to its next scatter then randomly samples a scattering angle. Iteratively repeating this process, allows for photons and beta particles to be transported in any material ranging from 1 keV to 1 TeV.[40] By tracking photons, the transport may be compared with measured data taken from MSLRAD. A new feature (unnamed) labeled 'ieleh' in the input deck was also activated for this transport. This input weights electron transport for electrons with energies exceeding the cross-section libraries for faster convergence with high energy electrons. Due to the transport of high-Z source nuclei,

the max bank size had to be increased to 100,000 to avoid transport errors. Lastly, 'deltm' was set to $1.012 \times 10^6$, or one over the minimum density of the atmosphere. This parameter increases the maximum flight particles can undergo without tracking their location (default is 20 cm). Applying this greatly reduces the computational run time of the transport over large geometries.

### 2.3.2 Atmosphere and Regolith Model

The GCR model was comprised of concentric spheres of actual Mars size, similar to Figure 2.4 with the inner-most sphere having a radius of 3387 km, which will define the inner graveyard. The Martian atmospheric profile was taken from equations given by NASA Glenn Research Center,[41] and is shown in Figure 2.7. In this case, since particles are highly penetrating, radiation dose varies less with altitude. Because of this, the atmospheric model may be greatly simplified. This model was also used to compare to other transport codes to observe any changes in the physics models for the 2018 Mars Radiation Modeling Workshop. This workshop was started in 2016 as a way to compare radiation transport models with the goal of validating particle transport with MSLRAD data, and is held every 2 years in Boulder, Colorado, as a way to compare, improve, and validate particle transport models to better understand the radiation environment on Mars.[42] The atmospheric and regolith compositions were once again taken from OLTARIS. The regolith was considered to be 10 m thick, sufficient to capture all albedo effects. The atmosphere was split into 35 density discretizations with total column depth of $20\,\mathrm{g\,cm^{-2}}$ which is the average column density measured by the Curiosity Rover at $-4431$ m from March 1, 2018, to July 1, 2018. The density discretization gets finer as the atmospheric density increases to properly capture the 3D nature of this model. Small discretization edits were made at high altitudes to remove any remaining decimals from the $20\,\mathrm{g\,cm^{-2}}$ required.

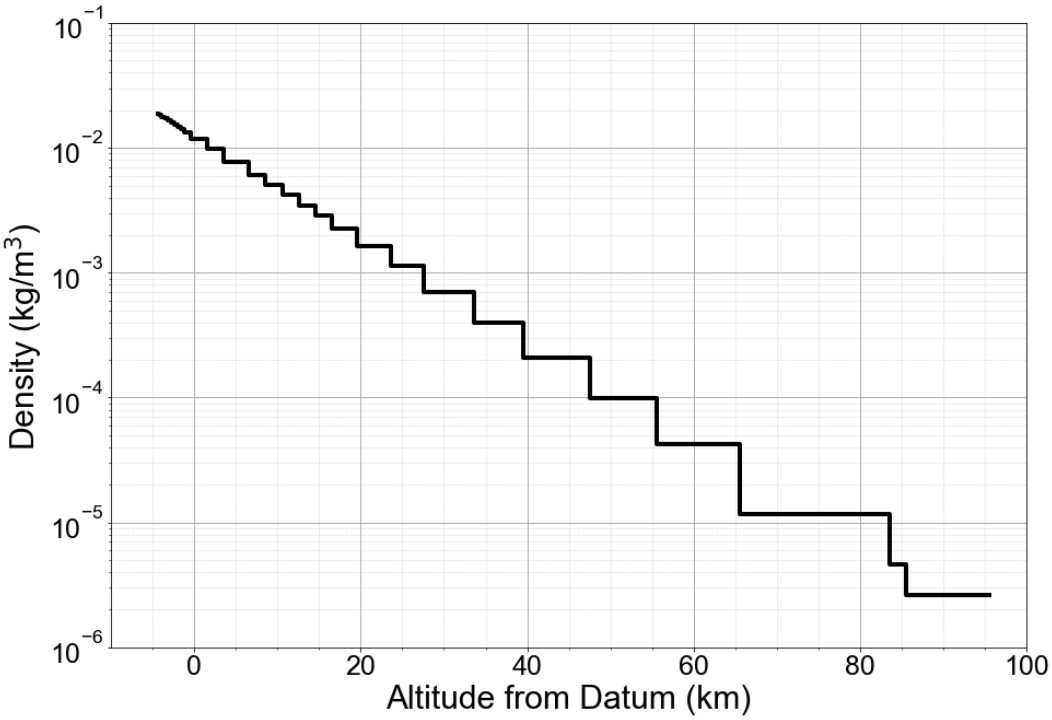


**Figure 2.7**: *Atmospheric density profile with altitude from Datum taken from NASA Glenn Research Center.*[41]

### 2.3.3 GCR Source Term

To simulate GCRs, an isotropic spherical shell source was used. To validate the model with MSLRAD measurement, and to save computational time, individual source spectra were simulated for particles ranging from hydrogen to nickel. These source spectra were provided by Dr. Daniel Matthiae who developed a one-parameter model to describe GCR spectra based off measurements from the Advanced Composition Explorer spacecraft in 2013.[43] All source nuclei were represented by the most abundant Earth isotopes. Each probability distribution function contained 1000 energy discretizations logarithmically spaced between $10\,\mathrm{MeV\,n^{-1}}$ and $200\,\mathrm{GeV\,n^{-1}}$. A figure showing example spectra for GCRs is shown in Figure 2.8. It should be noted that GCRs do not follow the same shape as an SPE. The GCR source spectra for all particle types have increased particle flux around $200\,\mathrm{MeV\,n^{-1}}$ to $500\,\mathrm{MeV\,n^{-1}}$ and decrease at lower and higher energies. As previously stated, 200 MeV protons can directly reach the surface of Mars, which means there should be a maximum dose observed in this region.

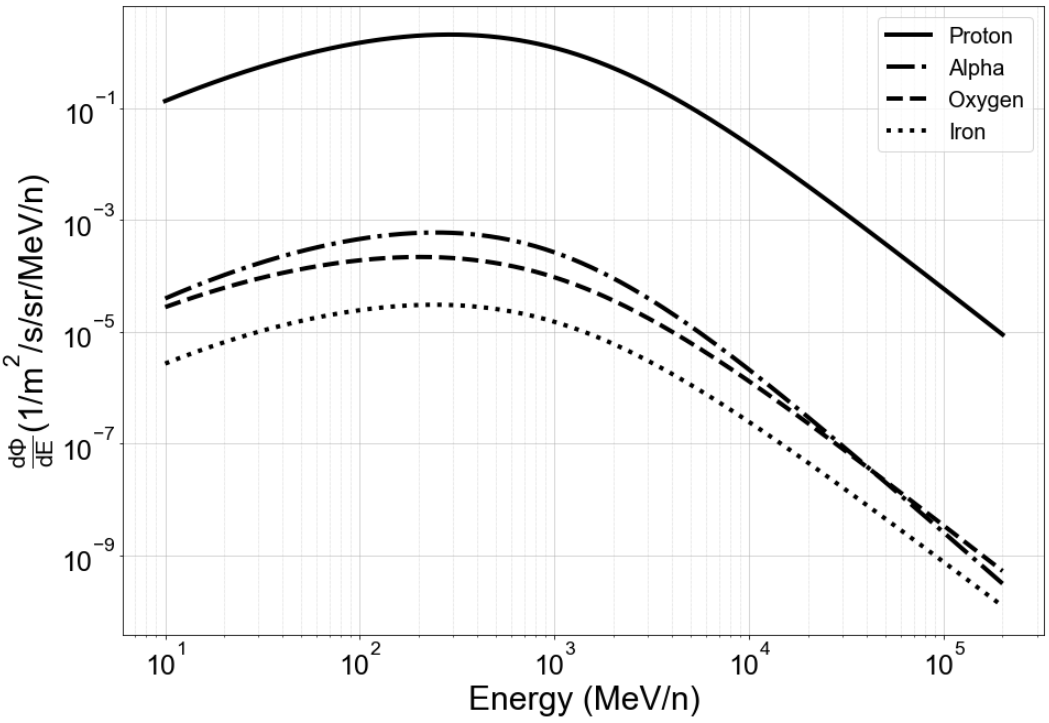


**Figure 2.8**: *Differential flux for particles of interest as function of energy.*

### 2.3.4 T-Cross and T-Track Tally

For this geometry, two different tallies were considered: a T-cross tally and a T-track tally. The T-cross tally was set to tally a surface that is 2 m above the Martian regolith. The T-track tally was set to tally the volume between 1.99 m and 2 m from the regolith. This is the approximate location where the MSLRAD is located on the Curiosity Rover. For both cases, the tally was set to have 200 energy discretizations logarithmically spaced between 100 keV and 100 GeV. All tally units were adjusted to output energies in MeV $n^{-1}$. The particles tallied were: proton, neutron, deuteron, triton, helium-3, alpha, Z=3-5, Z=6-8, Z=9-14, Z=14-24, Z>24, electron, positron, muon+, muon-, pion+, pion-.

The T-cross tally will return important angular information about the particles crossing the tally surface. This angular discretization was set to have angular binning from 0° to 30° and from 30° to 90° from the zenith. The 0° to 30° discretization was made to simulate the acceptance region of the MSLRAD. A diagram of the MSLRAD is shown in Figure 2.9. RAD A, B, and C are thin silicon detectors that consist of an inner annular region for radiation

measurement, and an outer annular region that RAD C uses for anti-coincidence. This ensures that any ions that enter into RAD D are within a 30° acceptance angle in order to keep dead time to a minimum. RAD D, E, and F are all scintillator type detectors with RAD D being made of cesium iodide and RAD E, and F out of plastic. By using two different scintillating materials, MSLRAD is able to distinguish between neutrons and gamma rays by observing differences in detection efficiencies of RAD D and E.[44] Detector F acts as an anti-coincidence detector that will reject ions and scattered photons entering from the sides or from under the instrument.

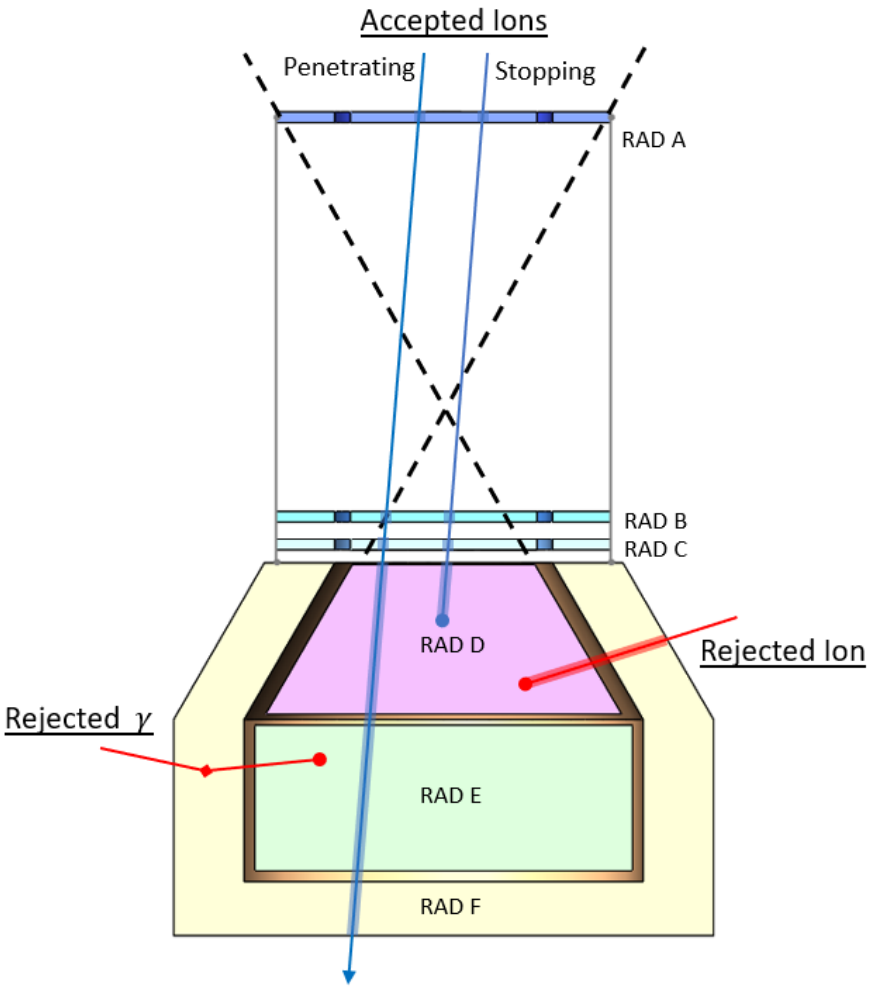


**Figure 2.9**: *Example of accepted and rejected particles for MSLRAD.*

By using the 0° to 30° discretization for the T-cross tally, charged particle tally results may be post processed and directly compared to measurements from the Curiosity Rover.

However, for neutral particles such as neutrons and gamma rays, the data is presented as a flux in $4\pi$sr with no angular dependence. For these cases, a solid angle correction factor is used to correct the angular dependence of the tally.As an estimate for dose, the T-track tallies are used to estimate the averaged $4\pi$sr spectra for each tallied particle type. This is then used with dose conversion coefficients to estimate whole body dose and effective dose equivalent based on quality factors defined in ICRP-123.[45] This document specifically addressed calculation of dosimetric quantities astronauts may be subject to for light ions, heavy ions, and subatomic particles ranging from $10\,\mathrm{MeV\,n^{-1}}$ to $100\,\mathrm{GeV\,n^{-1}}$.

### 2.3.5 Source Scaling

To get the proper units for the T-track tally, the tally results for each transported particle type $j$ at tally $i$ had to be scaled by the energy integrated source flux $S_j$, multiplied by the area of the irradiating plane $A_S$, and then divided by the volume of the tally. The scaled tally results for each source particle type must then be summed for each individual tallied particle type for their respective tallied energy bins (E), or,

$$\bar{\phi}_{i,j}(E) = \sum_j \frac{S_j A_s T_{i,j}^{track}(E)}{(4/3)\pi(R_2^3 - R_1^3)} \tag{2.1}$$

Due to the source term dependence on solid angle (in $4\pi$), and the solid angle dependence in the tally (also in $4\pi$sr), there does not need to be a solid angle correction applied in the T-track results. This however is not true for the T-cross results since the tallied bin of interest has solid angle dependence between $0^\circ$ and $30^\circ$ from the zenith. This means that for the T-cross tally there must be a $4\pi$ correction factor applied to correct for solid angle dependence in the source term. This tally is also fundamentally different from the T-track tally and is divided by the cross-sectional area of the tally surface instead of a tally volume, i.e.,

$$\bar{\phi}_{i,j}(E) = \sum_j \frac{4\pi S_j A_s T_{i,j}^{cross}(E)}{\pi(R_i^2)} \tag{2.2}$$

# Chapter 3

# Solar Particle Event Results

## 3.1 Correction Factors and Post Processing

Cases were simulated in PHITS version 2.88[46] starting with the surface at Olympus Mons with increasing energy. The kernel data were extracted from the PHITS output and organized into matrices with non-contributing rows removed to reduce plotting time and memory. An example of a kernel response for 316 MeV protons at the surface of the Hellas Planitia is shown in Figure 3.1. It was found that primary radiation below 39.8 MeV does not reach the surface of Olympus Mons and secondary neutrons may be considered negligible for proton source energies below 25.1 MeV. It was also found that all proton kernels above 60 km from the Datum were identical to an "infinite atmosphere" case where no Martian regolith was considered. Simulations were optimized considering these observations to efficiently obtain desired quantities. In the case of high interest regions such as the Hellas Planitia, Datum, and Olympus Mons, all proton source energies were simulated. For the remaining eight regolith cases, protons above 25.1 MeV were simulated.

For the SPE source spectra, measured solar fluence data taken by the Geostationary Operational Environmental Satellites (GOES) and Goddard Medium Energy (GME) from the IMP-8 satellite[47] were used. These satellites captured the energy dependent fluence profile to energies just under 300 MeV for 577 measured solar events taking place between

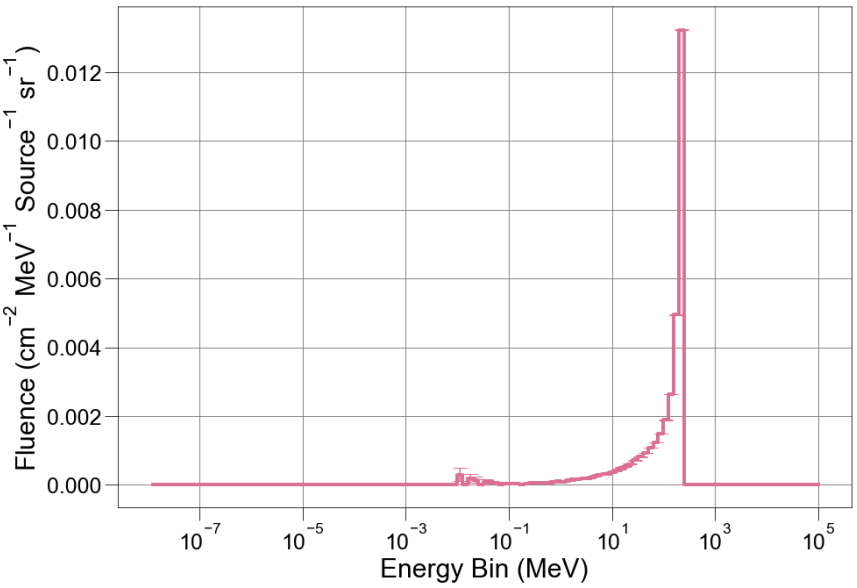


**Figure 3.1**: *Kernel response to 316 MeV protons transported through 22.7 g cm$^{-2}$ of atmosphere to the surface of the Hellas Planita.*

November 1973, to December 2012. To simulate the spectra beyond 300 MeV, a differential Weibull fit is applied to the data. The three factor differential Weibull is defined as

$$\frac{d\Phi}{dE} = \Phi_0 k\alpha e^{\alpha-1} e^{-kE^{\alpha}}, \tag{3.1}$$

where constants $\alpha, \Phi_0$, and $k$ are the shape, scale, and location factors found by a logarithmic based least squares regression. An example fit of the October 19, 1989, SPE is shown in Figure 3.2. Examples of Weibull fitting to other, less significant SPEs is shown in Figure 3.3, and the Weibull fitting code is given in Appendix D.

The October 19, 1989, event will serve as the benchmark since it is the largest event on record with high confidence in the measured proton spectrum.[48] The Weibull curve was integrated and re-binned to share the same binning structure as the mono-energetic proton source (10 energy discretizations per logarithmic decade). To remove the area dependence on the source term, a source normalization factor equal to the area of the irradiating source plane $\pi r_s^2$ was applied. The kernel responses for the mono-energetic proton source of energy $i$ is multiplied by the total number of particles in the same energy bin $\Delta E_i$ for the Weibull

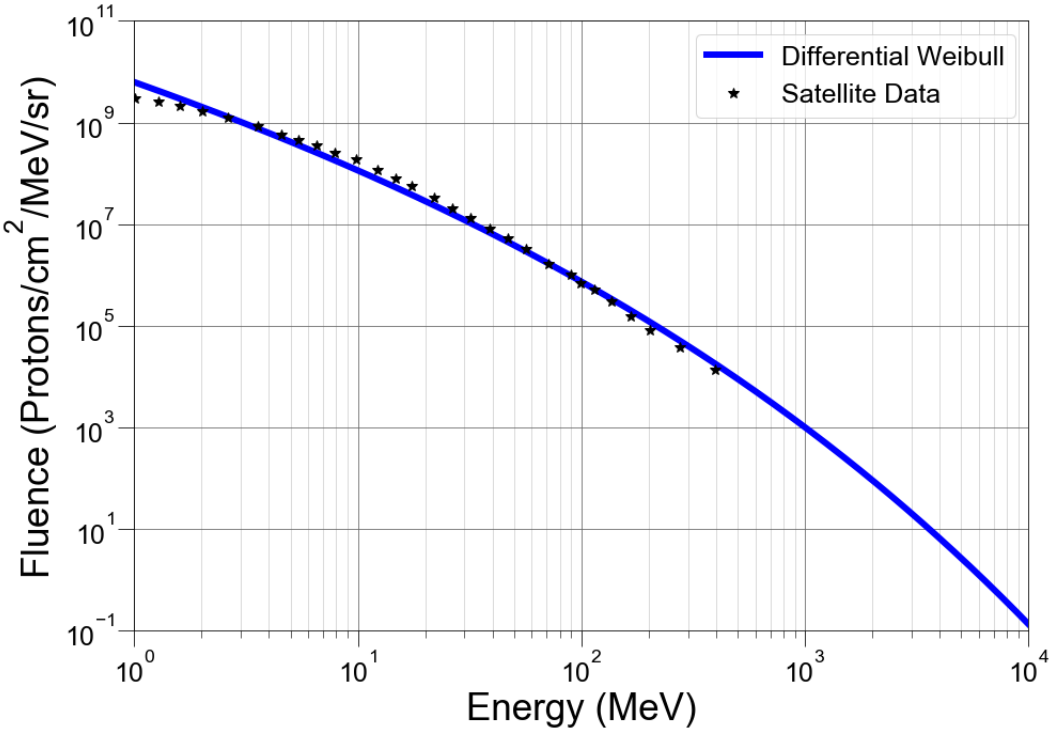


**Figure 3.2**: *Differential Weibull fit for October 19, 1989, solar event.*

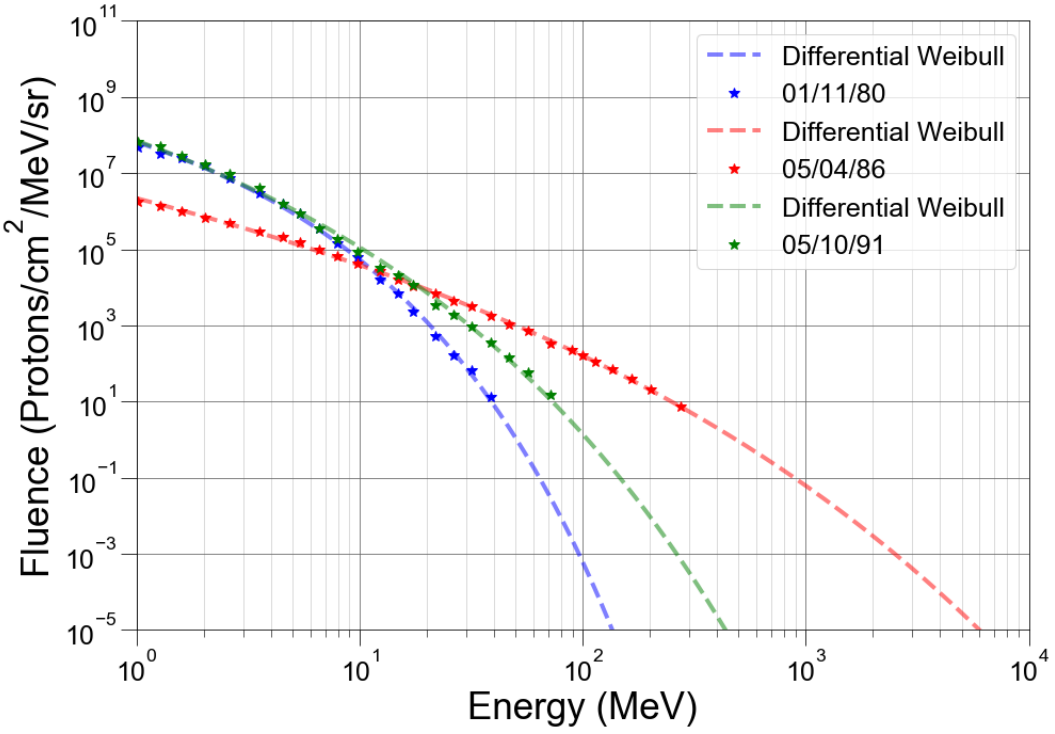


**Figure 3.3**: *Differential Weibull fit applied to other solar events.*

fit. Correcting for solid angle describes the total amount of particles in the source energy bin $E_i$ incident to the outermost atmospheric shell, so that the source strength for energy bin $i$ is

$$\Phi_{s,i} = \frac{d\Phi_i}{dE_i} \pi r_s^2 \Delta\Omega \Delta E_i \tag{3.2}$$

Where $\Phi_{s,i}$ is the total source fluence for discretized energy bin $i$, $\frac{d\Phi_i}{dE_i}$ is the differential Weibull fit applied over $i$, $\pi r^2$ is the source plane area (source normalization factor), and $\Delta\Omega$ is solid angle correction for the GME/GOES data[47] ($4\pi$).

Applying this scaling to all kernel responses over all source proton energies describes the angular particle spectrum induced for each energy bin in the Weibull fit. Correcting for T-cross solid angle dependence, and combining the results in their respective tallied energy bins describes the total differential fluence spectra on tally $T$, or

$$\Phi_T(E) = \sum_{i=0}^{E_{max}} \Phi_{s,i} \int_\Omega k_{T,i}(E) d\Omega. \tag{3.3}$$

Where $\Phi_T$ is the fluence spectra at tally $T$, $E_{max}$ is the maximum energy, and $k_{T,i}$ is the kernel response created at tally $T$ for source energy $i$. This produces an energy dependent, differential fluence response spectrum for one particle type. Repeating this process for all particle kernels, at a particular column depth, and for a given SPE, gives the total induced differential fluence spectrum for all primary and secondary particle types.

## 3.2 Particle Fluences

With correction factors applied, particle fluences may be plotted for each particle type. A plot of the fluence spectra for all tallied particles at the Hellas Planitia for the October 19, 1989, event is shown in Figure 3.4. From this figure, it is shown that low energy neutrons dominate the fluence spectra. It was also observed that all ions heavier than 1 amu have fluences that are orders of magnitude less than the proton and neutron spectra over their energy domain. The electrons and positrons were also shown to have high fluence in the

1 MeV to 10 MeV energy range, however, the effective dose coefficients shown in Figure 2.6 show that the electrons in this region will contribute negligible effective dose when compared to proton and neutron radiation.

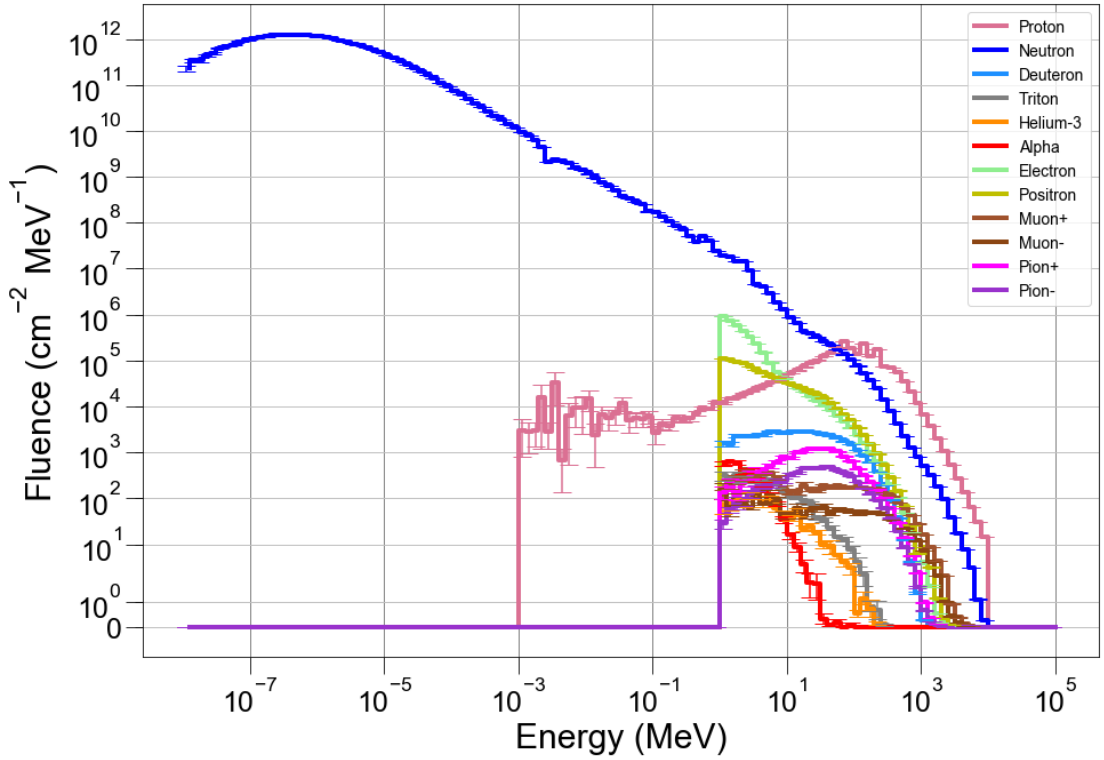


**Figure 3.4**: *Total fluences for all tallied particles at 22.7 g cm$^{-2}$ for October 19, 1989, event.*

Plotting the proton and neutron fluences for an infinite atmosphere, the Hellas Planitia, Datum, and Olympus Mons shows how altitude changes and Martian regolith affect the fluence spectra observed. This comparison is shown in Figure 3.5. From the four cases, it is observed that the Martian regolith makes a considerable difference in the neutron spectrum at thermal energies. This plot also shows that the proton fluence greatly increases for changes in altitude while the neutron spectrum has little change due to the finite range of charged particles. A sharp drop in neutron fluence at 3.9 keV was observed and was found to be linked to a sharp increase in the radiative capture cross-sections of $^{27}$Al and $^{39}$K. It should also be noted that there is little change in all other particle types with altitude for the regolith cases. To observe this please refer to the full particle fluence spectra for each case shown in Appendix B.

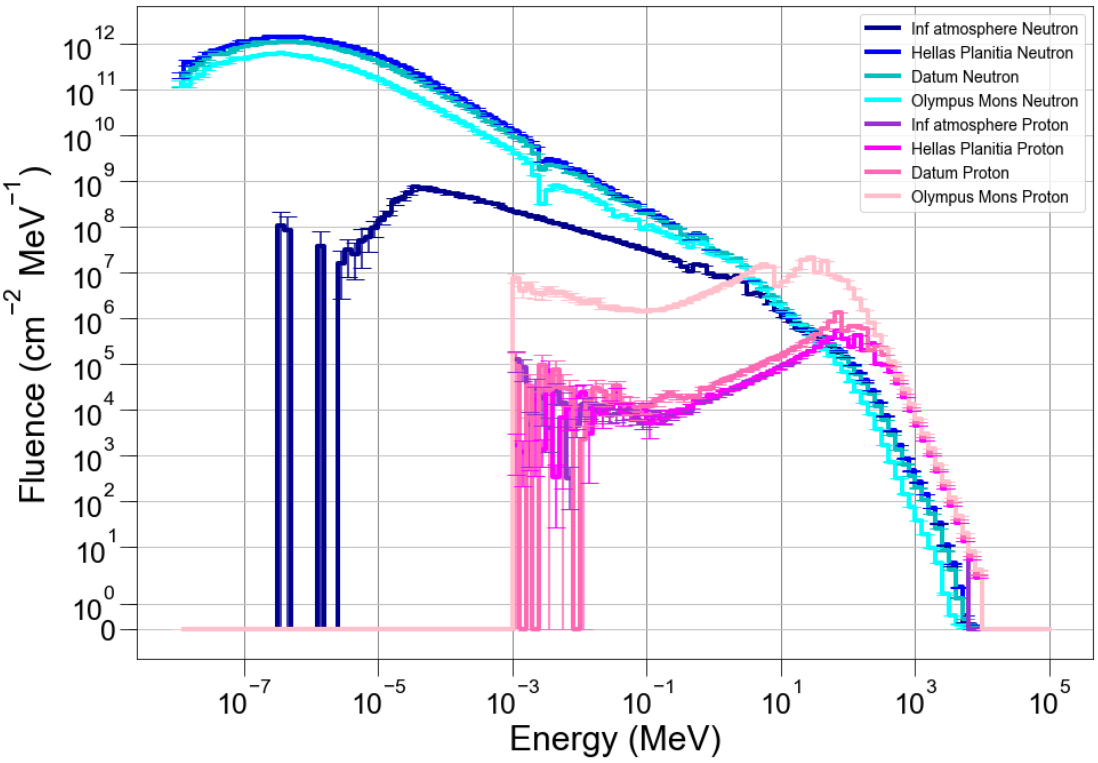


**Figure 3.5**: *Total proton and neutron fluence comparisons for infite atmosphere, Hallas Planitia, Datum, and Olympus Mons for October 19, 1989, event.*

## 3.3 Dose Conversion and Dose Estimates

### 3.3.1 Absorbed Dose

With the fluence spectra for all particles, dose conversion coefficients may be used to estimate absorbed dose, individual organ dose, and effective dose for both male and female phantoms. These coefficients can provide dose estimates for source particles ranging from subatomic particles to $^{58}$Ni. For dose equivalents and effective dose, two quality factors may be considered in these coefficients: the standard ICRP 60 model,[49] or quality factors defined by NASA in 2011.[50] Since this thesis specifically deals with radiation dose on Mars, the quality factors defined by NASA were used. The tallied fluence data had finer energy binning than the coefficient data, so a re-binning code was written to adjust the coefficient data to fit the fluence structure by using a fluence weighted interpolation when necessary.

Applying this to all tallied particles at the Hellas Planitia the energy-dependent absorbed

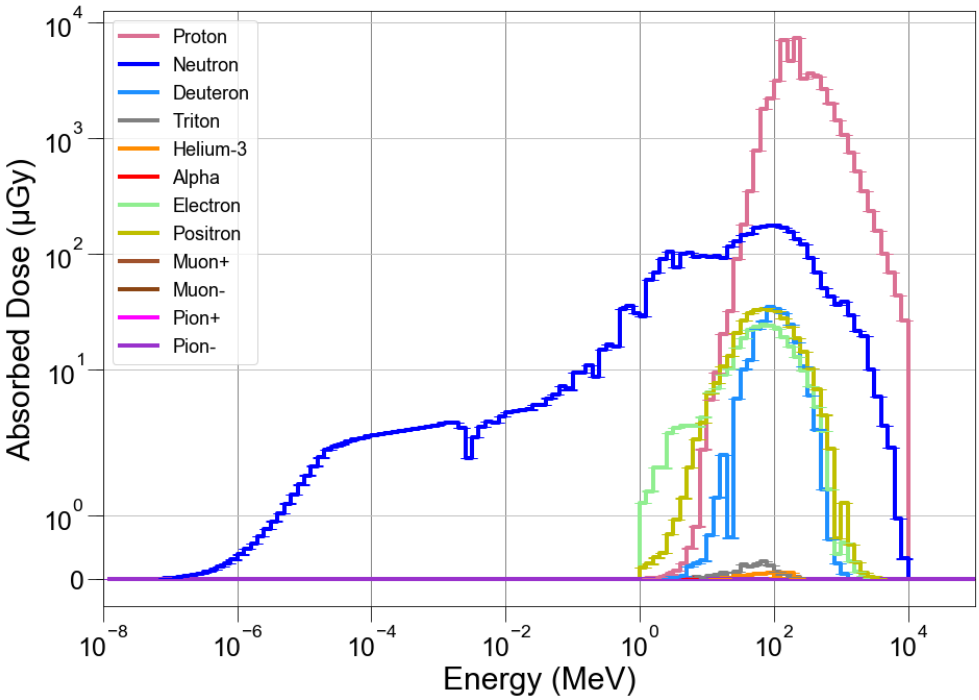


**Figure 3.6**: *Absorbed dose for all tallied particles at 22.7 g cm$^{-2}$ for October 19, 1989, event.*

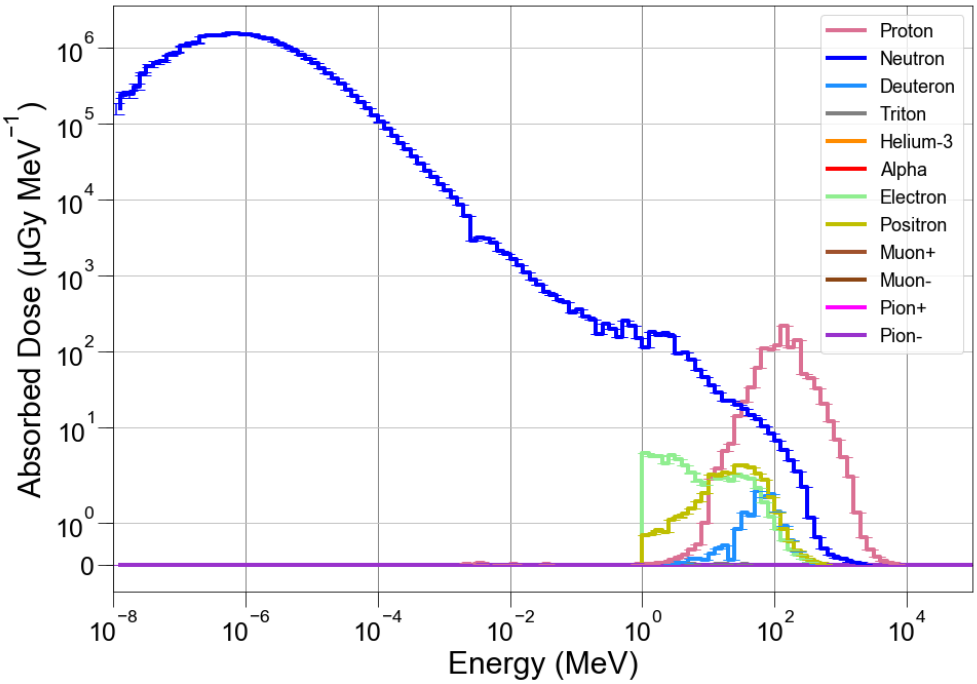


**Figure 3.7**: *Absorbed dose per MeV for all tallied particles at 22.7 g cm$^{-2}$ for October 19, 1989, event.*

dose for all particle types was found. This is shown in Figure 3.6. Despite the neutrons dominating the fluence spectra, protons dominate the absorbed dose spectra at the surface. This is because the absorbed dose response for protons is much larger than neutrons due to ionization. Dose with energy is also commonly expressed in differential $\mu\text{Gy}\,\text{MeV}^{-1}$ units. This graph may be seen in Figure 3.7. Summing the absorbed dose contribution for all energies allows the absorbed dose to be expressed for varying surface locations. A table showing absorbed dose contribution for all particle types for four models is given in Table 3.1. As validation for these absorbed dose estimates, the surface dose for a column density of $19.7\,\text{g}\,\text{cm}^{-2}$ was compared to surface dose estimates previously produced by Dr. Jingnan Guo at $20\,\text{g}\,\text{cm}^{-2}$ for the October 19, 1989, event.[10] The results calculated using the PHITS kernel method were found to be within 2% of Dr. Jingnan Guo's estimates with a total absorbed dose of 86.4 mGy.

| Particle Type | Absorbed Dose (μGy) | | | |
|---|---|---|---|---|
| | Infinite Atmosphere (22.7 g $\text{cm}^{-2}$) | Hellas Planitia (22.7 g $\text{cm}^{-2}$) | Datum (13.7 g $\text{cm}^{-2}$) | Olympus Mons (1.62 g $\text{cm}^{-2}$) |
| Proton | 68,531 | 68,607 | 118,768 | 574,056 |
| Neutron | 3,656 | 4,881 | 4,604 | 3,276 |
| Deuteron | 236 | 244 | 240 | 230 |
| Triton | 1.46 | 1.74 | 1.81 | 3.02 |
| Helium-3 | 0.626 | 0.682 | 0.858 | 1.54 |
| Alpha | 0.109 | 0.114 | 0.162 | 0.615 |
| Electron | 139 | 168 | 123 | 89.6 |
| Positron | 202 | 222 | 168 | 97.7 |
| Muon+ | 20.6 | 19.2 | 14.6 | 5.58 |
| Muon- | 5.09 | 5.04 | 3.74 | 1.36 |
| Pion+ | 0.340 | 38.8 | 43.9 | 84.6 |
| Pion- | 0.090 | 13.4 | 15.4 | 23.8 |
| Total | 72,794 | 74,202 | 123,982 | 577,870 |

**Table 3.1**: *Absorbed dose for October 19, 1989, SPE for various particle types for four separate surface and atmospheric conditions.*

### 3.3.2 Effective Dose

By applying interpolated radiation quality factors defined by NASA to absorbed dose contribution for each energy bin, the effective dose may be estimated. The effective dose for all particle types at the Hellas Planitia is given in Figure 3.8. A graph with the differential effective dose for all particles is shown in Figure 3.9. It may be seen in these plots that there is a sharp drop in effective dose at 3.9 keV and at 0.316 MeV. The first peak is due to spikes in the radiative capture cross-sections of $^{27}$Al and $^{39}$K which makes a large portion of the Martian regolith causing diminished back scattering effects in this energy domain. The second peak is due to a sharp increase in the radiative capture cross-section of $^{16}$O at about 0.4 MeV. Summing the effective dose over all energies, or by integrating the differential effective dose over all energies gives the total effective dose. Once again, forming a table of effective dose the risk to astronauts may be expressed for the surface locations of interest as seen in Table 3.2.

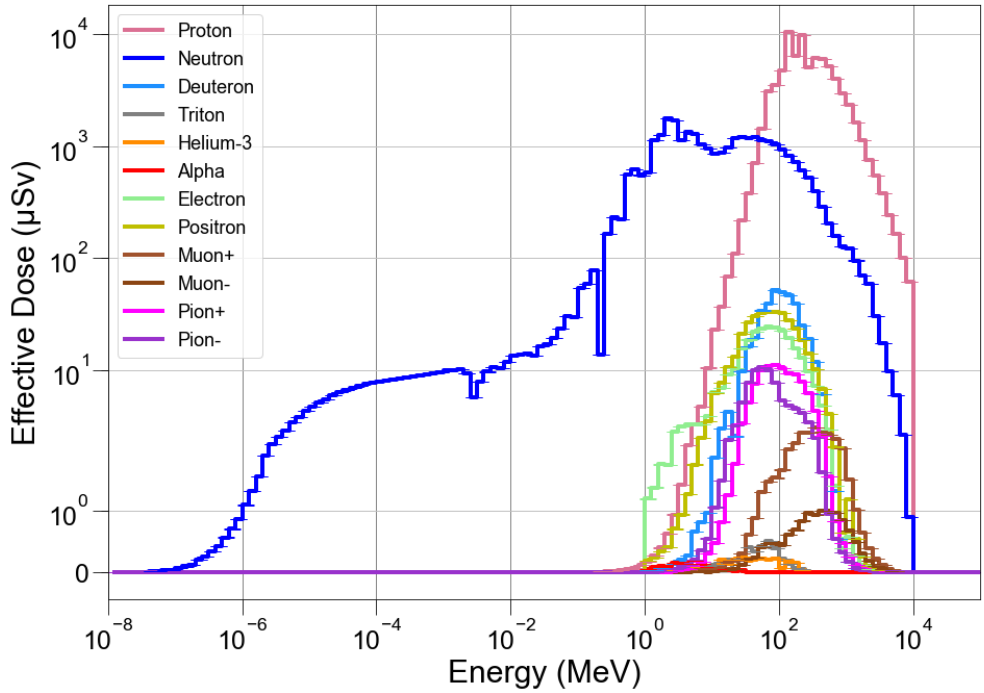


**Figure 3.8**: *Effective dose for all tallied particles at 22.7 g cm$^{-2}$ for October 19, 1989, event.*

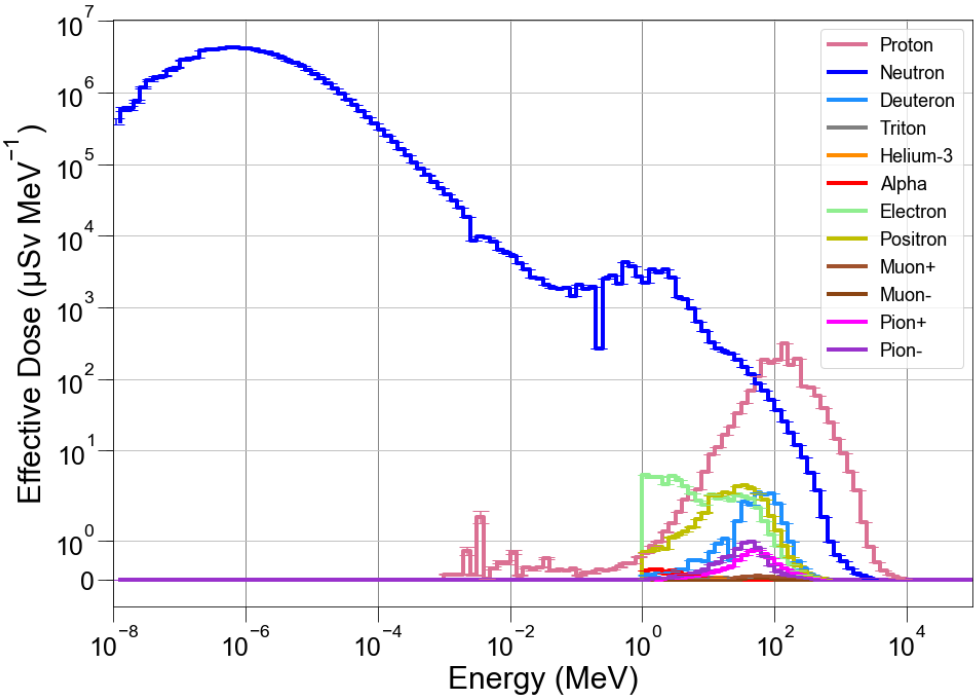


**Figure 3.9**: *Effective dose per MeV for all tallied particles at 22.7 g cm$^{-2}$ for October 19, 1989, event.*

| Particle Type | Effective Dose (μSv) | | | |
|---|---|---|---|---|
| | Infinite Atmosphere (22.7 g cm$^{-2}$) | Hellas Planitia (22.7 g cm$^{-2}$) | Datum (13.7 g cm$^{-2}$) | Olympus Mons (1.62 g cm$^{-2}$) |
| Proton | 109,021 | 109,159 | 187,127 | 967,328 |
| Neutron | 29,840 | 43,726 | 42,890 | 34,311 |
| Deuteron | 375 | 387 | 384 | 402 |
| Triton | 3.05 | 3.58 | 3.84 | 7.11 |
| Helium-3 | 2.43 | 2.74 | 3.60 | 9.27 |
| Alpha | 1.72 | 1.76 | 2.50 | 11.4 |
| Electron | 139 | 168 | 122 | 89.6 |
| Positron | 201 | 222 | 168 | 97.7 |
| Muon+ | 20.6 | 19.2 | 14.6 | 5.62 |
| Muon- | 5.09 | 5.05 | 3.74 | 1.37 |
| Pion+ | 0.579 | 58,4 | 66.6 | 128 |
| Pion- | 0.204 | 40.6 | 46.5 | 72.3 |
| Total | 139,611 | 153,793 | 230,834 | 1,002,462 |

**Table 3.2**: *Effective dose for October 19, 1989, SPE for various particle types for four separate surface and atmospheric conditions.*

Current standards for astronauts set occupational dose limits to a 3% risk of radiation induced death. Simulation showed that the doses received at the surface of Mars in both the Hellas Planitia and the Datum are in the hundreds of mSv range. In this range, there is an observable increase in excess cancer risk. This dose would be delivered in just over 25 days, which means that for a long-term mission that takes over 30 days, there could be significant cancer risks if proper shielding were not used. In the Olympus Mons case, the total effective dose was approximately 1 Sv. This dose in a short time will lead to mild radiation sickness which can include nausea, fatigue, headaches, or in rare cases death.

### 3.3.3 Organ Absorbed Dose and Dose Equivalent

Using the dose coefficient database, absorbed dose estimates for all organs were calculated. These values for the October 19, 1989, event at the Hellas Planitia for all organs listed in the coefficient database is given in Figure 3.10. In this case, the absorbed dose not scaled for relative biological effectiveness is between 60 mGy and 90 mGy for all organs. With relative biological effectiveness, the organ absorbed doses observed were around 95 mGy to 135 mGy-Eq. At this dose, the non-cancer radiation absorbed dose limits defined by NASA were not close to being reached for any organ type. Taking into account the quality factors defined by NASA, the dose equivalent may be found for all organs. These are shown in Figure 3.11. The bone marrow dose equivalent is much less than the other organ dose equivalents. This is because NASA decided that the risk of developing leukemia is much less than that of solid cancers based on previous radio-biological data,[51] including large studies of leukemia in mice,[52] as well as studies on the lethality of charged particles on B-cell precursors.[53] This study on B-cell precursors suggests that these cells, which are the most common cause of lymphoma/leukemia, have very low probability of surviving radiation induced damage.[53]

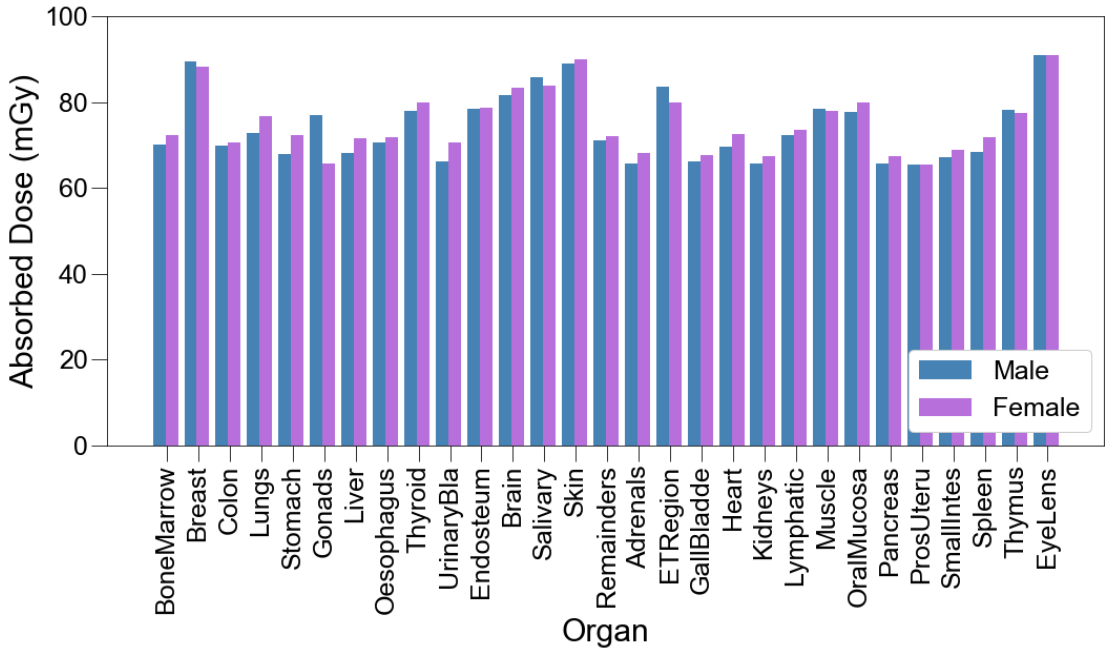


**Figure 3.10**: *Absorbed dose for all organ types included in fluence to dose coefficient library for a male and female computational phantom at 22.7 g cm$^{-2}$ for October 19, 1989, event.*

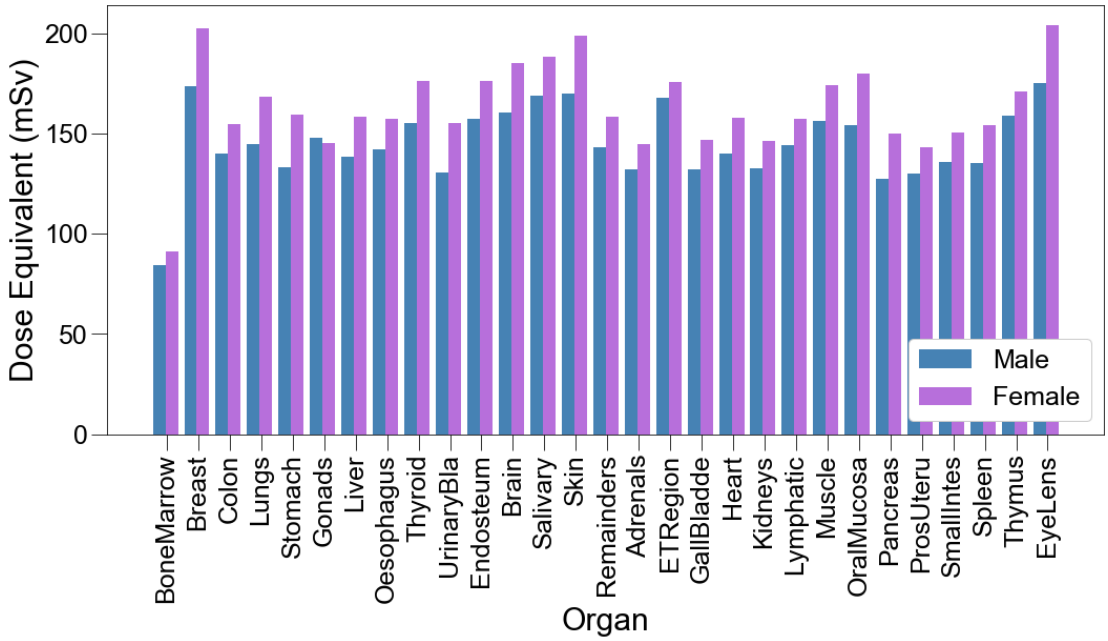


**Figure 3.11**: *Dose equivalent for all organ types included in fluence to dose coefficient library for a male and female computational phantom at 22.7 g cm$^{-2}$ for October 19, 1989, event.*

### 3.3.4 Dose with Source Energy

It was shown previously that the maximum amount of effective dose at the Hellas Planitia surface happens at about 175 MeV where protons have a CSDA range of approximately 25 g cm$^{-2}$. As evidence that these are primary protons and not the effect of higher energy protons slowing down or interacting, total particle dose was plotted with proton source energy. This result plotted in Figure 3.12 shows that there is a distinct increase at 200 MeV where primary protons reach the surface. Secondary neutron dose, caused by cascading

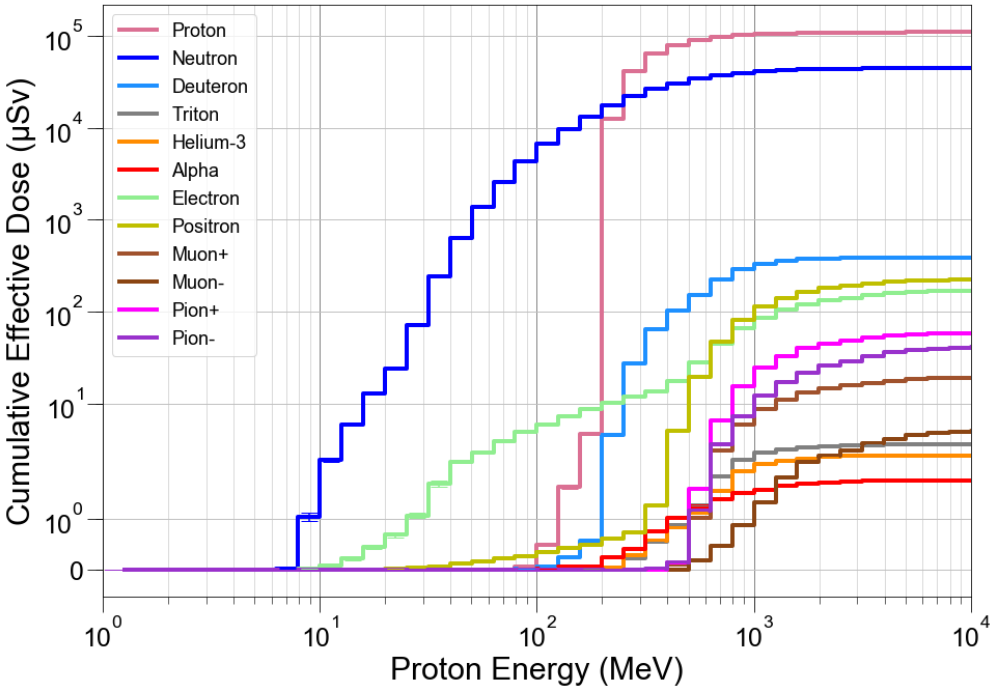


**Figure 3.12**: *Radiation dose with proton source energy for all tallied particle types at the Hellas Planitia (22.7 g cm$^{-2}$) for October 19, 1989, event.*

protons, starts at a proton source energy of 7 MeV, the average binding energy of a neutron in $^{16}$O. Another interesting observation is that for all events, the dose contribution for particles greater than 10 GeV is negligible due to the decreasing, almost asymptotic nature of the Weibull fit. At these energies, particles are so rare and have such large energy that there is a relatively low probability that one of these particles will interact in the atmosphere, or with a computational phantom. Therefore, at the lowest surfaces of Mars, mono-energetic protons do not need to be transported below 25 MeV and greater than 3 GeV.

### 3.3.5 Dose for All Solar Events

Since intensities of SPEs can vary by orders of magnitude, other events must be assessed to draw conclusions about SPE doses and risks. By iterating through all SPEs, for all surface cases of interest, and plotting the frequency of radiation dose at the surface, a cumulative distribution function of the dose and frequency of SPEs was formed. This CDF of effective dose is shown in Figure 3.13. A similar plot for whole-body absorbed dose is shown in Figure 3.14. At the Hellas Planitia, in the nearly 40 years of solar data, 90% of events have an effective dose less than about 400 µSv and 80% less than about 20 µSv. This means that large events hazardous to human health are very rare at the Hellas Planitia which would make it, and surrounding low altitude regions ideal for future missions. The Datum is also relatively safe, being very close to the same profile as the Hellas Planitia. In the Olympus Mons case, we can see that considerably higher doses can be observed. It may also be seen that for an infinite atmosphere case, the effective dose for an infinite atmosphere 22.7 $\mathrm{g\,cm^{-2}}$ is approximately the same as the dose at the Datum and Hellas Planitia for relatively large events. This diverges for events that have effective doses less than about 0.1 µSv since these events will see little primary radiation, and will have a larger contribution due to thermalized neutrons in the Martian regolith.

### 3.3.6 Dose Above the Surface

To further observe albedo effects, and to determine dose at altitudes above the surface of Mars, tally surfaces were iterated against altitude to find radiation absorbed and effective dosees above the Martian surface. A plot showing the proton and neutron absorbed dose for the three regolith cases of interest is shown in Figure 3.15. A plot showing the effective dose of all secondary particles and their development throughout the atmosphere for the Hellas Planitia case is shown in Figure 3.16. It may be seen in the plot that absorbed dose estimates with altitudes for both protons and neutrons are similar for both the Hellas Planitia and the Datum. However, in the case of Olympus Mons, the lack of atmosphere means that low energy particles can travel far above the surface with little energy loss. Because of this,

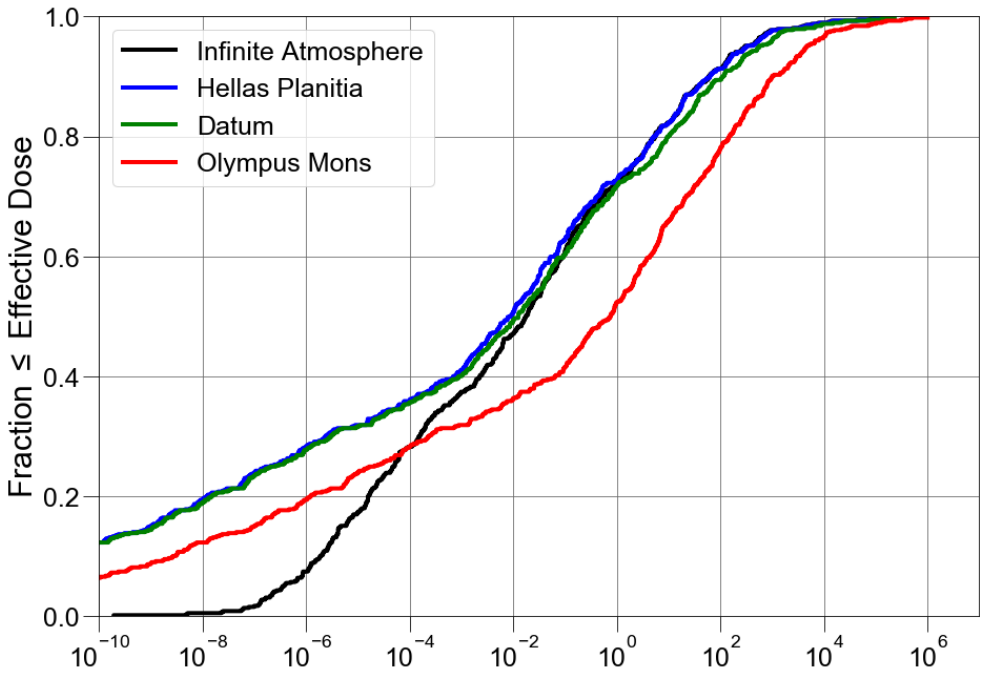


**Figure 3.13**: *Cumulative distribution function of effective dose due to SPEs for four surface cases.*

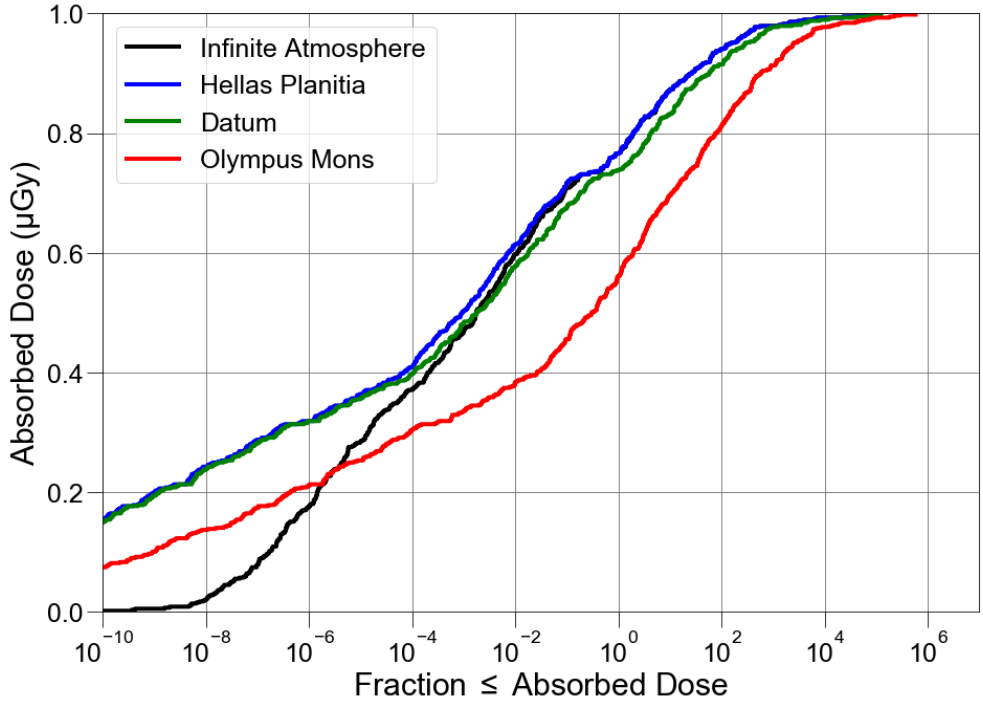


**Figure 3.14**: *Cumulative distribution function of absorbed dose due to SPEs for four surface cases.*

the albedo effects of the Martian regolith are much more prominent in the Olympus Mons case. For protons, the radiation dose converges with the Datum and Hellas Planitia above an altitude of 60 km. For neutrons, a clear offset is observed that does not dissipate with increasing altitude. For the case showing all secondary particles, its observed that subatomic particles and neutrons have increasing effective dose as they cascade to the surface. For all ions, there is an increase in effective dose that reaches a critical point in the atmosphere then begins to become shielded.

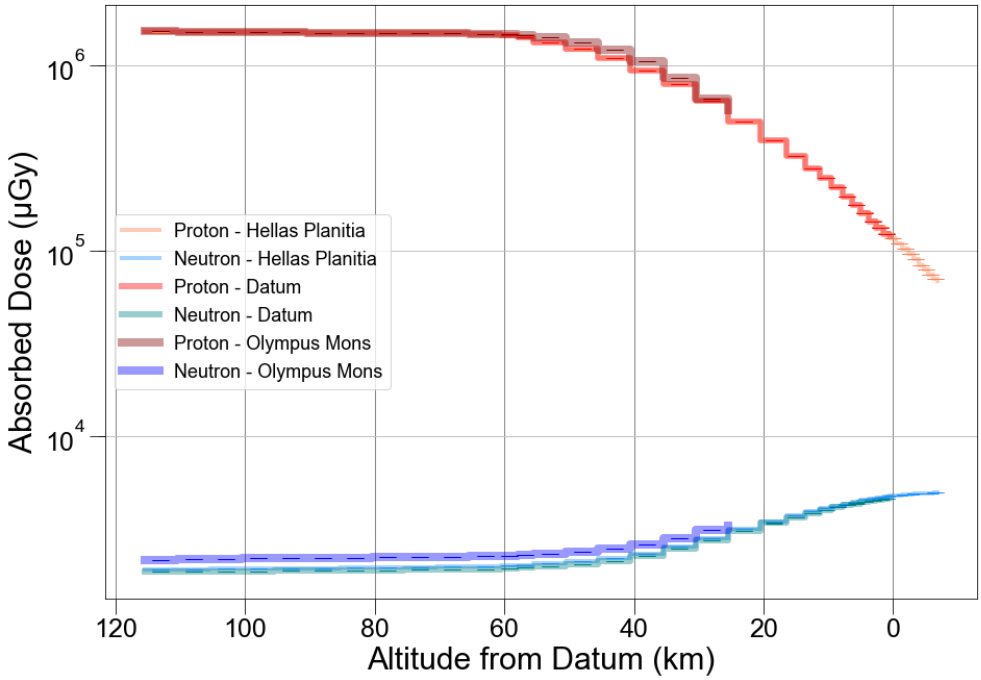


**Figure 3.15**: *Absorbed dose with altitude for Hellas Planitia, Datum, and Olympus Mons cases.*

### 3.3.7 Dose in Regolith

For the case of a Martian habitat, regolith is often considered for shielding since it eliminates the need to bring additional material when traveling to Mars. To test the shielding effects of regolith, the three regolith cases were considered with regolith depths down to 5.5 m. Absorbed dose with regolith depth is given in Figure 3.17, and the effective dose with regolith depth is given in Figure 3.18. In all cases, the proton absorbed dose is reduced by

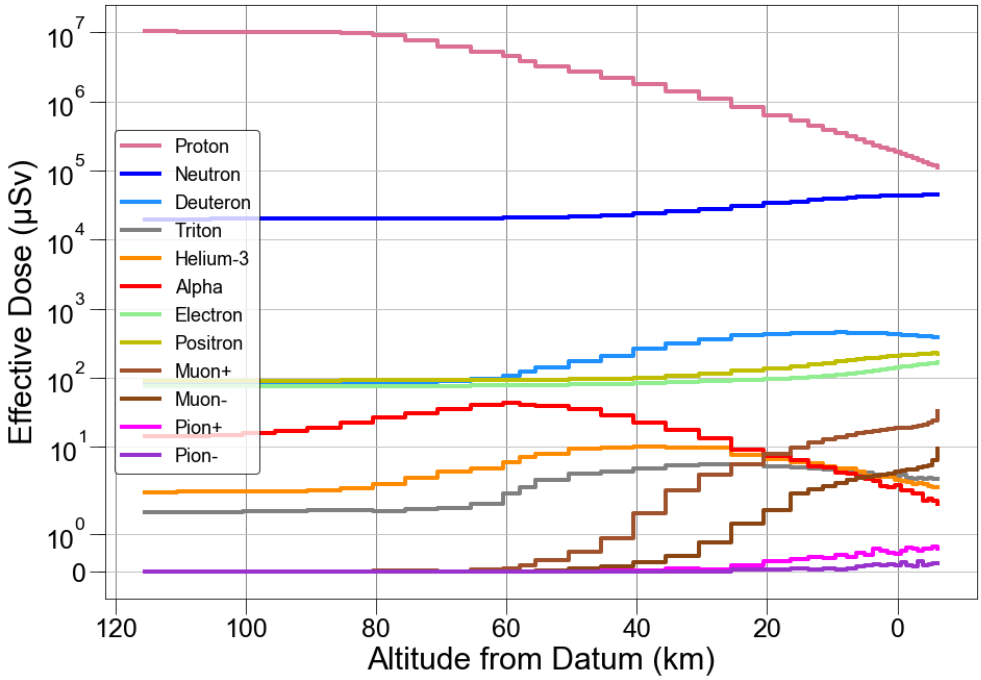


**Figure 3.16**: *Effective dose for all particle types vs. altitude at the Hellas Planitia.*

more than 75% in the first 25 cm of material, after which the dose begins to show exponential attenuation. In the first 25 cm of the Olympus Mons case, the neutron dose increases because the protons have not sufficiently slowed to energies below the spallation threshold. After the first 25 cm, the neutron doses for the three cases begin to converge and show a similar shape. For the proton dose, it takes about 1 m for the three cases to exhibit similar behavior. At depths greater than 4.5 m, proton dose starts to diverge again due to differences in the incident spectra to the regolith. For the case at the Hellas Planita, no more than 25 cm of regolith material would be necessary to shield one of these events. However, depending on the longevity of the habitat, it may be worth considering more regolith material for both radiation shielding and structural support.

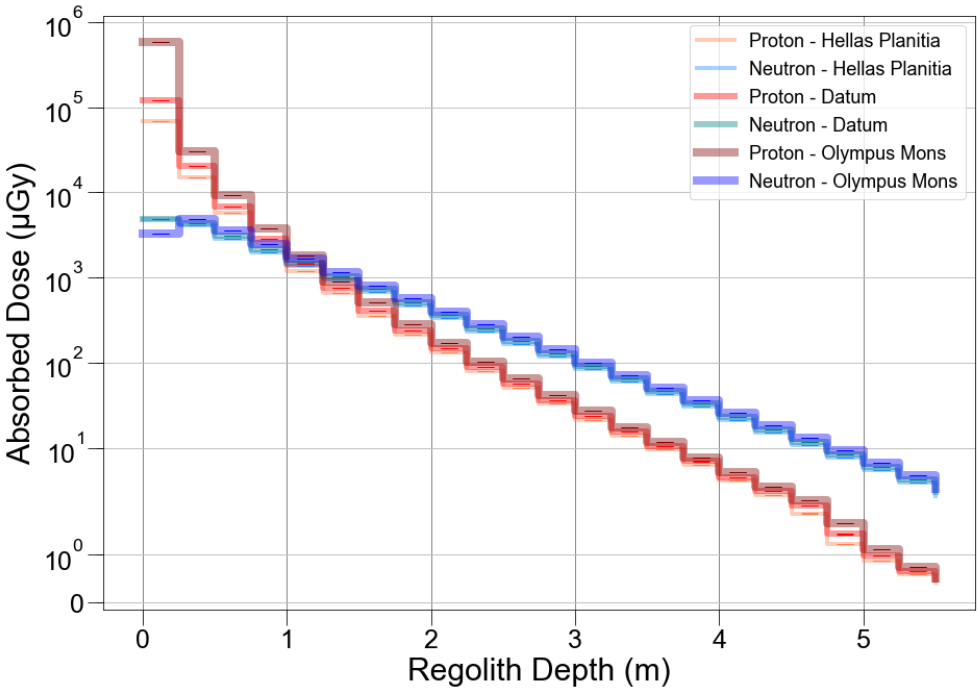


**Figure 3.17**: *Absorbed dose vs. Regolith depth for Hellas Planitia, Datum, and Olympus Mons.*

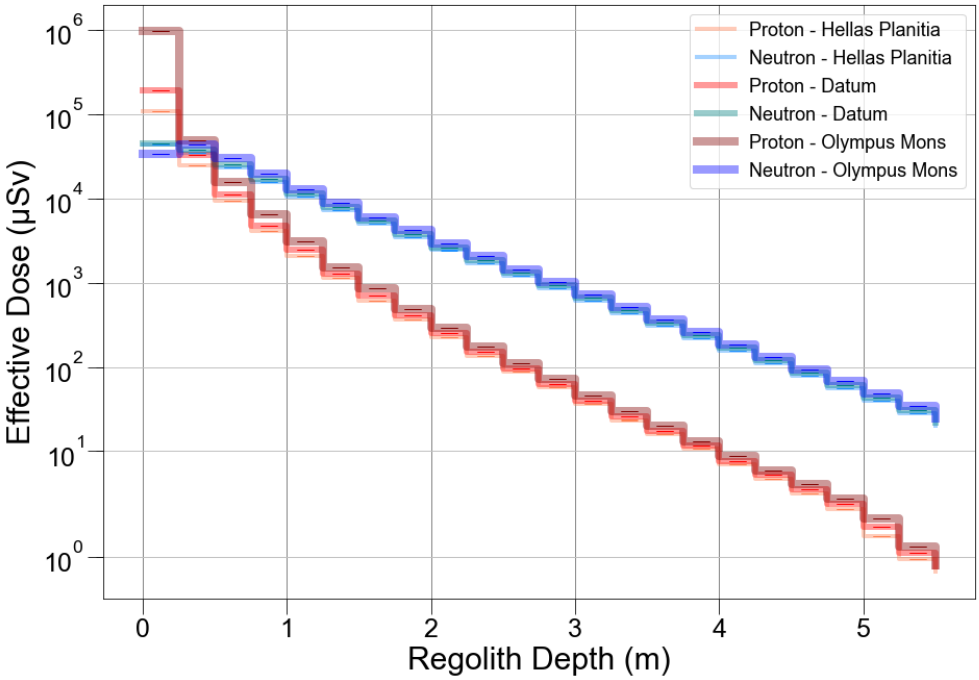


**Figure 3.18**: *Effective dose vs. Regolith depth for Hellas Planitia, Datum, and Olympus Mons.*

# Chapter 4

# Galactic Cosmic Ray Results

## 4.1 Particle Flux

### 4.1.1 Light Ions, Photons, and Neutrons

With the tallies corrected for source strength, the average particle flux may be plotted for all tallied particle types. The flux is presented as the T-track result, scaled for source strength, and divided by $4\pi$ to represent the flux for all incident angles. For simplicity, the flux results are separated into three categories: light ions with neutrons and photons, heavy ions with atomic numbers greater than two, and subatomic particles. The flux results for light ions is shown in Figure 4.1. This figure shows that the high energy ions follow the same general shape as the transported source spectra. At these energies the particles have relatively high range and are not likely to interact with atmospheric material. In the low energy domain, it is seen that down-scattering from higher energies plays a significant role and contributes to large errors. It is observed that flux of photons and neutrons has an inverse relationship with energy. It can also be seen in the photon spectra that there is a 511 keV peak due to pair production. At 1 GeV there is a discontinuity in the photon flux spectra caused by the code changing from EGS5 data to cross-section models. There also appears to be a small error at 3 GeV for triton and helium-3 data likely due to a bug in the PHITS code when changing from its JQMD model to the JAMQMD + GEM model.

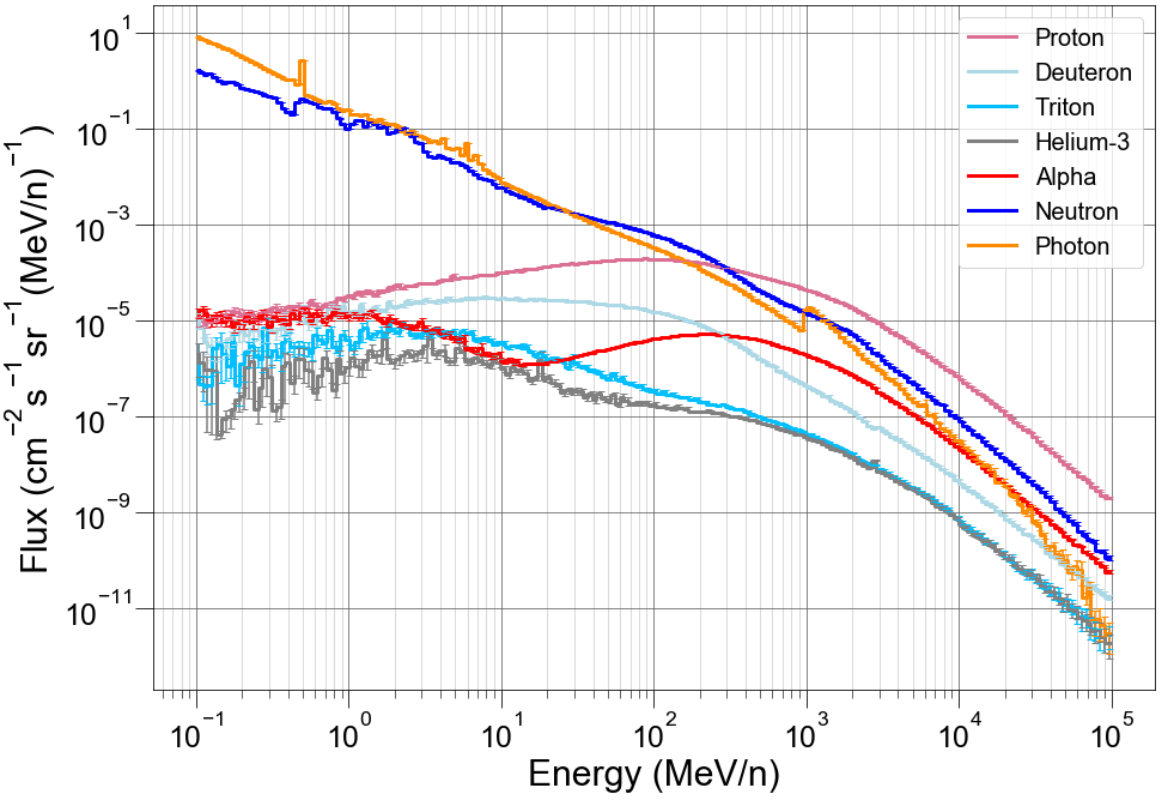


**Figure 4.1**: *T-track flux results for light ions, neutrons, and photons.*

### 4.1.2 Heavy Ions

The flux for heavy ions shown in Figure 4.2. The tally results show that the magnitude of the fluxes generally goes down with atomic number with the exception of Z=6-8. This is because these particles closely follow the shape of their transported source spectra above 30 MeV n$^{-1}$. Since these particles have high mass and kinetic energy, they are extremely difficult to shield and are not likely to interact in a thin atmosphere. While shielding these particles is difficult, their flux is several orders of magnitude less than that of the light ions, and their contribution far less than source protons or alpha particles. In the low energy domain, down-scattering and particle fragmentation causes an increase in flux for particles with atomic numbers Z=3-8.

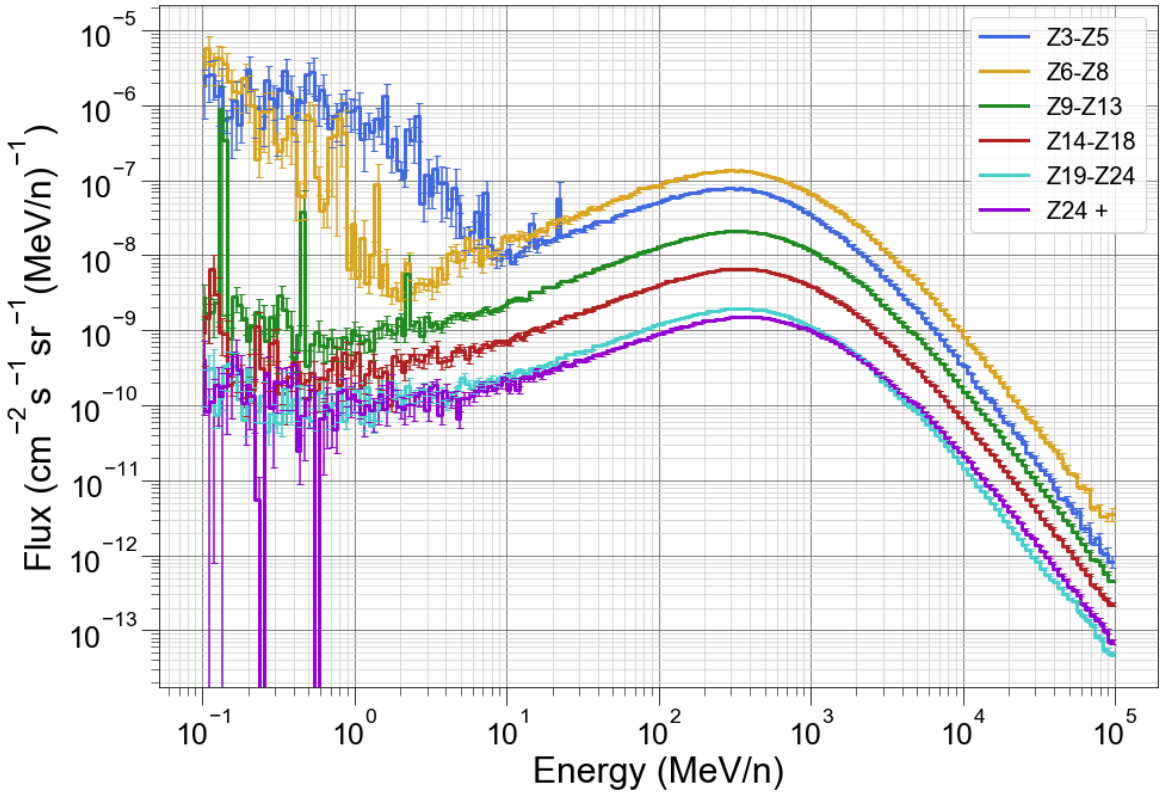


**Figure 4.2**: *T-track flux results for heavy ions (Z>2).*

### 4.1.3 Subatomic Particles

Tallied flux for subatomic particles is shown in Figure 4.3. Errors for the subatomic particles were relatively large for the high energy domain. It can be seen that positive and negative muons followed the same profile across the entire tallied energy domain. Positive and negative pions also showed this behavior but positive pions were not tallied below 1 MeV likely due to a bug in the PHITS code. Electrons and positrons were not tallied above the set EGS5 range of 1 GeV. It can also be seen that the electron and positron profiles diverge below 30 MeV. This is due to positrons annihilating causing a shorter overall track length in the tally, which by definition of the track length tally leads to a lower flux.

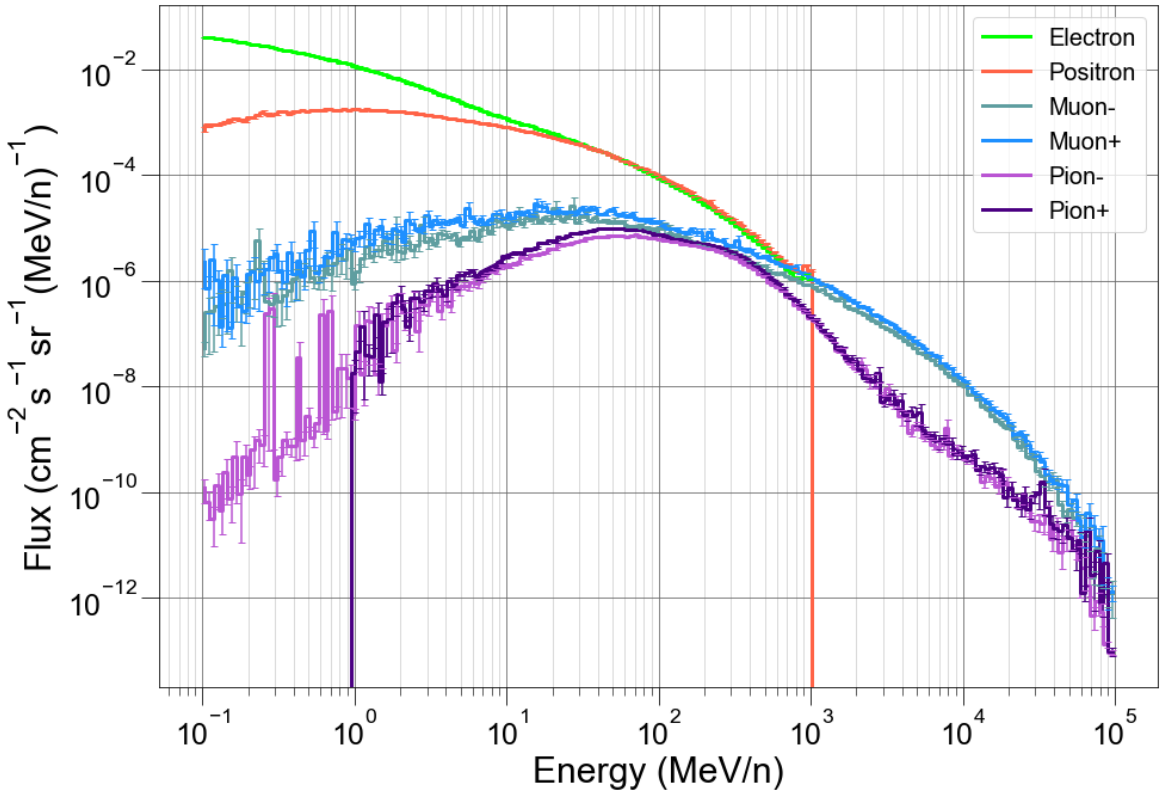


**Figure 4.3**: *T-track flux results for subatomic particles.*

## 4.2 Comparison with MSLRAD

### 4.2.1 Particle Flux

The T-cross tally results were directly compared with data taken by MSLRAD over the coarse of March 1, 2018, to July 1, 2018. To avoid comparing all particle types, only the most significant absorbed dose contributors will be compared. Comparisons for other particle types are given in Appendix B. The proton data show that protons with energies larger than approximately 500 MeV directly follow the profile of the proton source term. There is a slight variation in magnitude for high energy protons due to the particles losing energy to ionization and due to a loss of particles to the 30° to 90° zenith. Below 500 MeV the proton profile diverges from the proton source term due to slowing down, spallation, and scattering effects. From Figure 4.4 it is observed that the PHITS simulations were relatively accurate for estimating the measured proton profile.

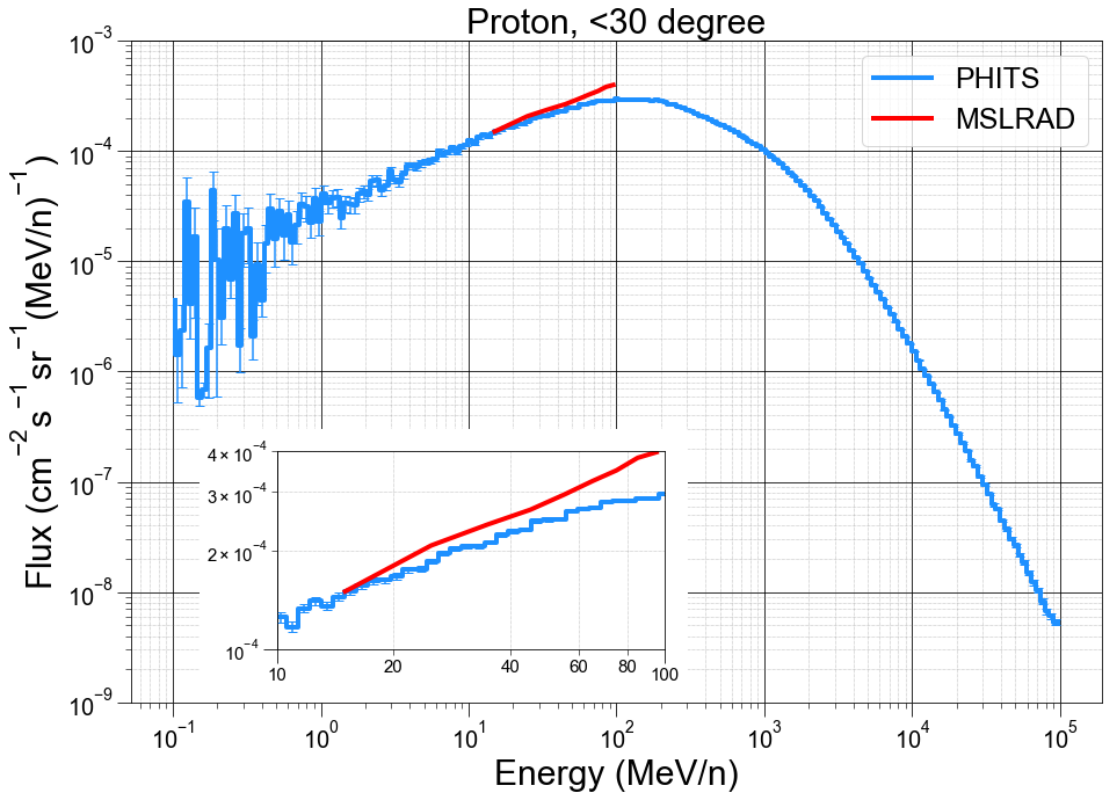


**Figure 4.4**: *Comparison of simulated proton flux with MSLRAD.*

For alpha particles, the tallied flux follows the same profile as the transported alpha source term with a noticeable decrease in magnitude. This is because alpha particles are heavily ionizing and are more readily stopped by the thin atmosphere of Mars. For low energies, the flux results show high error in the tally results since the range of these particles is too low to give reasonable Monte Carlo statistics at the tally surface. The alpha flux profile is shown in Figure 4.5. It may be noted again that PHITS was accurate in estimating the measured alpha particle flux. For the neutron profiles the T-cross tally for the 30° zenith was corrected for solid angle and then averaged over $4\pi$sr since MSLRAD cannot measure angular dependence of neutrons. These results were well-converged and had exhibited high particle flux below 100 MeV. It may be seen in Figure 4.6 that the PHITS simulations were close to the measured flux profile for all energies. Below about 200 MeV the simulations began to over estimate the radiation measurement. This is possibly due to the fact that the simulations did not take into account any inherent shielding in the detector design.

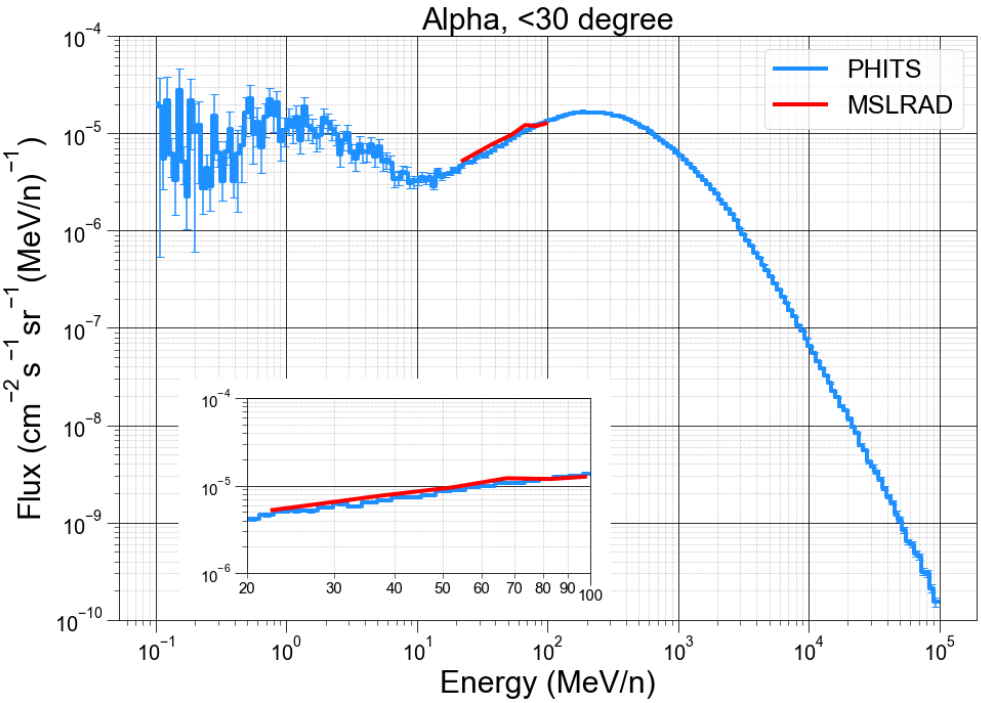


**Figure 4.5**: *Comparison of simulated alpha particle flux with MSLRAD.*

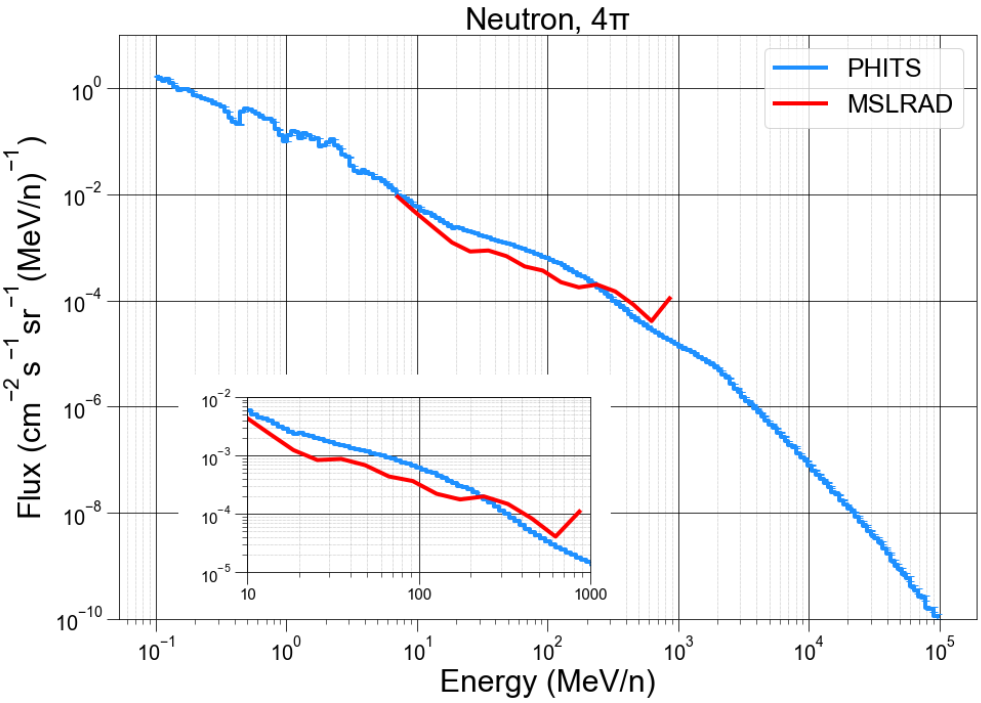


**Figure 4.6**: *Comparison of simulated neutron flux with MSLRAD.*

Lastly, for all particle types a comparison of the integrated particle fluxes was performed. For all simulated particles with the exceptions of Z=2-5, PHITS was within one standard deviation from the MSLRAD measurements. This demonstrates overall accuracy of the PHITS code in terms of integrated quantities. It may also be observed that the MSLRAD measurements from 2016 are very similar to the 2018 measurements showing little variation in solar activity over the two year time span. The bar plot comparing integrated solar fluxes with MSLRAD data is shown in Figure 4.7.

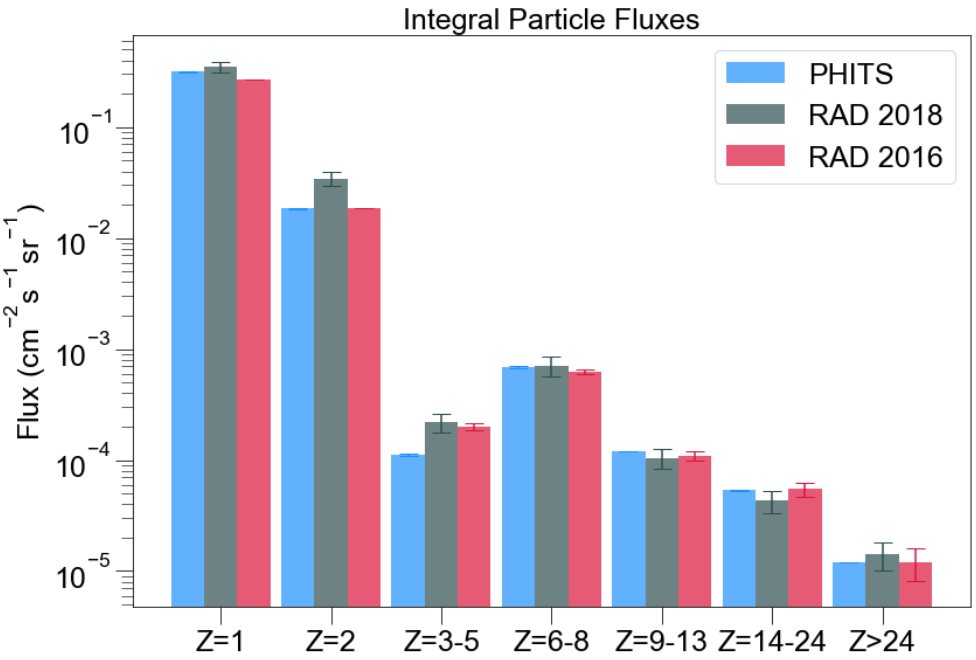


**Figure 4.7**: *Comparison of simulated integrated particle flux with 2018 and 2016 measurements taken from MSLRAD.*

### 4.2.2 Estimated Dose Rates

Dose rate estimates on Mars were performed using dose conversion coefficients provided in ICRP-123[45] and using detector information for MSLRAD. For all dose conversions the T-track data is used. Estimated dose to scintillating devices are estimated using the angular flux, average track length through the detector, and the mean free path of the particle in the scintillating material. Estimates for absorbed dose rates to RAD B, RAD E, whole body dose rates, and effective dose equivalent rates are given in Table 4.1.

| | Total Dose | Uncertainty |
|---|---|---|
| RAD B Dose / (μGy/d) | 186.9 | 0.083 |
| RAD E Dose / (μGy/d) | 243.5 | 0.096 |
| RAD E Dose Eq. / (μSv/d) | 611.8 | 0.157 |
| Whole body, ICRP123 Dose / (μGy/d) | 215.8 | 0.074 |
| Effective Dose Equivalent, ICRP123 Dose Eq. / (μSv/d) | 491.0 | 0.119 |

**Table 4.1**: *Various types of simulated GCR dose rates based on MSLRAD detector data and ICRP-123 flux to dose conversion coeffcients.*

The fractional effective dose equivalent contribution was plotted for each source particle and is shown in Figure 4.8. This figure shows that source protons contributed 65% of the total dose while source helium ions contributed 19%. It can also be seen that atomic numbers Z=3-5 had very little contribution to the total effective dose equivalent rate. In fact, 95% of GCR dose is linked to only 7 source ions: H, He, C, O, Mg, Si, and Fe. In future iterations, a significant amount of time and resources may be saved by only simulating significant contributors.

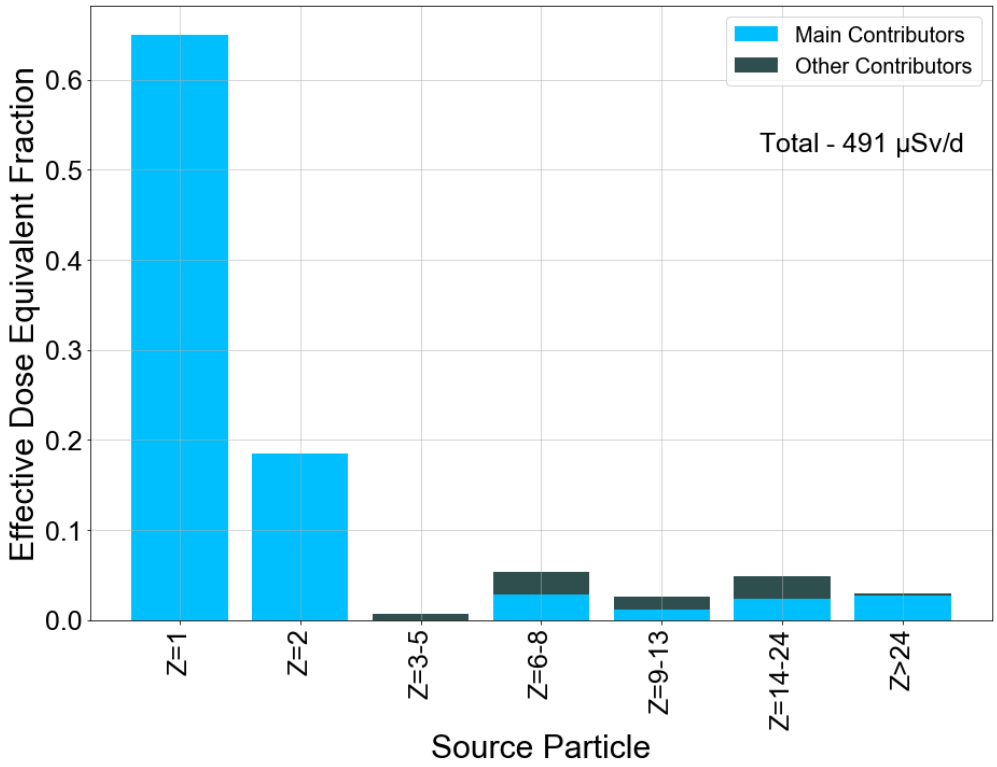


**Figure 4.8**: *Fractional contribution of effective dose for all simulated source particle types.*

A absorbed dose in RAD B and RAD E, and a tissue effective dose equivalent in RAD E were compared with simulation results. It is shown in Figure 4.9 that the absorbed dose estimates were within 10% from the 2018 measured dose in RAD B. The absorbed dose estimates in RAD E were underestimated by 17% for the 2018 measurement but was within 5% for the 2016 measurement. The effective dose equivalent estimates were shown to be 14% less that the 2018 measurement but were within 0.3% for the 2016 measurement. The difference in measured dose has to do with the fact that in 2016 the average column density measured by Curiosity was $23\,\mathrm{g\,cm^{-2}}$ as compared to the 2018 measurement of $20\,\mathrm{g\,cm^{-2}}$.[42] The models suffer from systematic error since they are based off a 4 month atmospheric measurement which is short in comparison to the Suns 11-year cycle. Solar activity can also fluctuate largely in relatively short periods of time which leads to changes in the incident GCR spectra, and the flux observed by MSLRAD. An example of this fluctuation is shown in the observed sunspot count given in Figure 4.10. While the simulated model was not as accurate for the 2018 measurement, the model was still observed to be within 20% relative error. Considering the amount of unknowns, assumptions, and simplifications made, this result is more than an acceptable estimate.

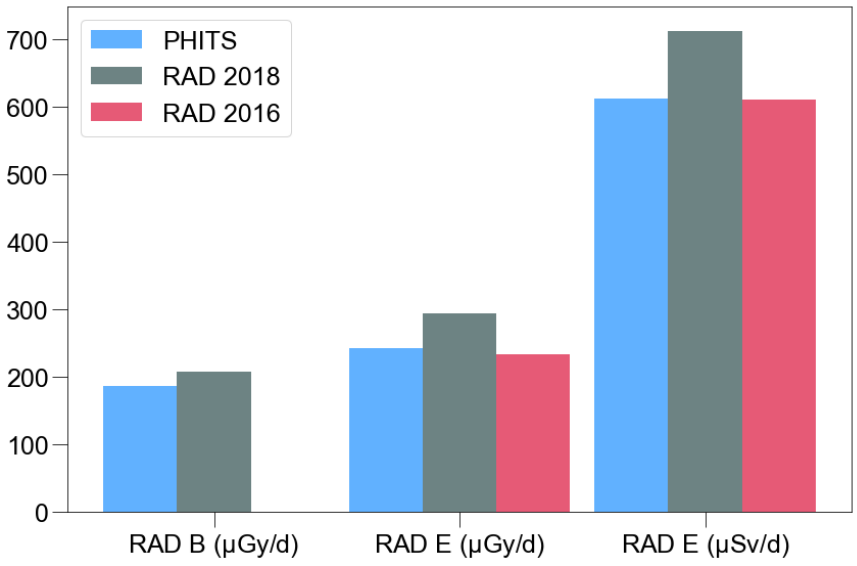


**Figure 4.9**: *Comparison of simulated detector dose with 2018 and 2016 measurements taken from MSLRAD.*

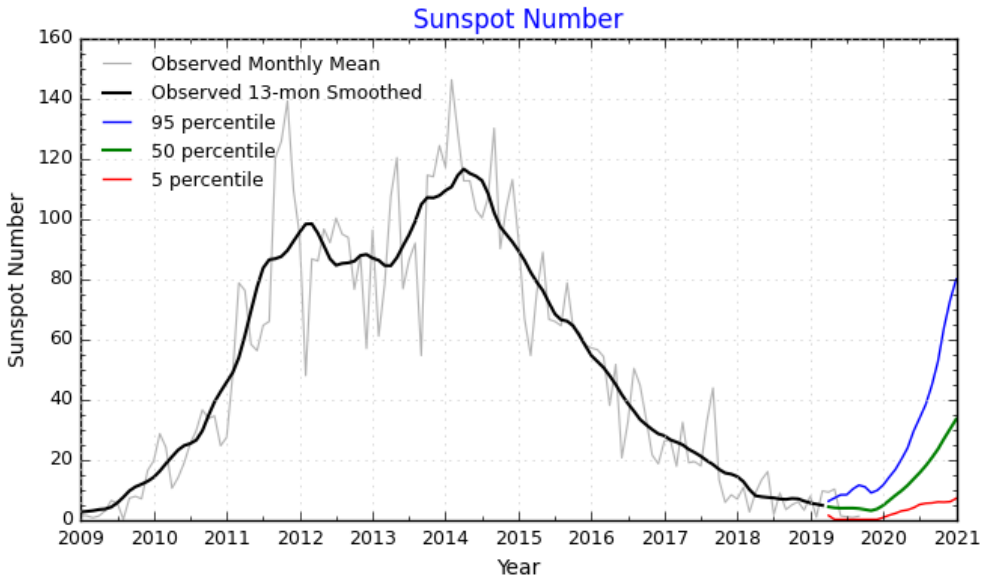


**Figure 4.10**: *Sunspot count since 2009 and predicted sunspot count.*[54]

To understand the energy dependence of dose rates for tallied particles, the dose contribution for all tallied particles was split into four groups: Particles less than 10 MeV $n^{-1}$, 10 −100 MeV $n^{-1}$, 100 −1000 MeV $n^{-1}$, and particle greater than 1000 MeV $n^{-1}$. This plot is given in Figure 4.11 . Atomic numbers Z=3-5 were not shown since they gave almost zero contribution to the dose rate. This was also observed to be true for all heavy ions with kinetic energies less than 100 MeV $n^{-1}$. It was found that the most significant tallied contributors are relatively light particles such as protons, alphas, neutrons, photons, electrons, and positrons. Protons between 100 MeV and 1000 MeV provide the majority of the surface dose since they have sufficient energy to reach the Martian surface and comprise most of GCR flux which peaks at approximately 200 MeV. From this figure it can be concluded that by intelligently setting tally cut-off energies for heavy ions, the convergence on integral quantities could be achieved more quickly. This could be helpful in the case of an altitude dependent model where data sets can be excessively large slowing down plotting code.

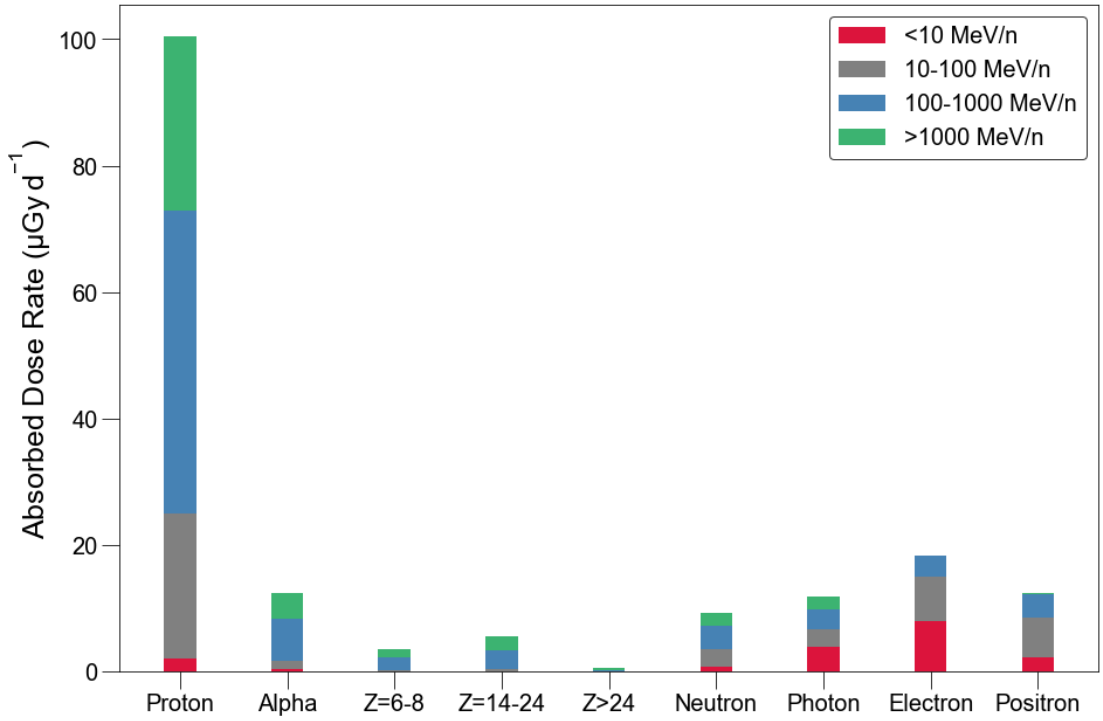


**Figure 4.11**: *Energy dependent dose rate contributions for various particle types.*

# Chapter 5

# Conclusion

Using the Monte Carlo code PHITS, simulations of SPEs and GCRs were performed. The first set of simulations estimated radiation dose due to SPEs, which are known for being highly unpredictable in both both their spectral features and magnitude. In order to provide these dose estimates, a flexible model using kernel response functions was constructed. This model consisted of concentric spheres of true Mars size that modeled 120 km of atmosphere and 6 m of regolith. The atmospheric density profile was taken from the Mars Climate Database[36] and used for the model. Atmospheric and regolith compositions were taken from OLTARIS.[37] Mono-energetic source protons were then simulated as an isotropic spherical shell source surrounding the Mars geometry. Using a T-cross tally kernel response functions were formed for various altitude column densities and for various surface locations on Mars. Three parameter Weibull fits were applied to measured satellite data[47] and the current tallies were scaled and post processed to explain particle fluences for 577 recorded SPEs. Using dose conversion coefficients, absorbed dose, effective dose, and organ dose equivalents were predicted for multiple surface locations.

Particle fluences for the October 19, 1989, event (the largest on record) showed that protons dominate the high energy domain while neutrons dominate thermal regions. It was found that as surface altitude increased the proton fluence also increased while neutron fluence decreased. Converting particle fluence to absorbed dose, it was shown that dose at

the Hellas Planitia can be as high as 74 mGy while at Olympus Mons, absorbed dose can reach 577 mGy. These findings were compared with estimates from Dr. Jingnan Guo and were found to be within 2% of the absorbed dose estimate for similar conditions. Taking into account quality factors defined by NASA, the effective dose at the Hellas Planitia was estimated to be 153 mSv, while dose at Olympus Mons was estimated at 1 Sv. For this SPE, dose equivalents were also calculated for organs of interest in concern for astronauts reaching NASA defined limits on the eye-lens, skin, and blood forming organs. It was found that it is unlikely that a single event will cause an astronaut to exceed organ RBE weighted dose limits at low altitudes, but SPE exposure at high surface altitudes may put an astronaut at risk of acute radiation sickness. Plotting the dose with source proton energy revealed information regarding particle ranges need to be simulated at the Martian surface. This also demonstrated that primary protons reach the surface of Mars at the Hellas Planitia at around 175 MeV, as expected. Next, absorbed and effective dose were plotted for all solar data giving information on SPE statistical doses. It was found that most SPEs do not deliver a significant amount of dose at the Mars surface. Last, absorbed and effective dose was plotted as a function of regolith depth to observe the shielding capabilities of Martian regolith. It was found that 25 cm of regolith provides enough shielding to reduce the proton absorbed dose by nearly 80%, and the neutron absorbed dose by nearly 20% at the Hellas Planitia.

The second set of simulations addressed GCRs. These particles tend to have higher energies and are fairly consistent for a given solar cycle. This model also consisted of concentric sphere of true Mars size but had an atmospheric density profile based on equations by the NASA Glenn Research Center in order to directly compare with other codes. The composition for the atmosphere and regolith were taken from OLTARIS. The atmospheric model consisted of $20\,\mathrm{g\,cm^{-2}}$ of atmospheric material and 10 m of Martian regolith. The source term simulated GCR particle spectra from protons up to a $^{58}$Ni. Two different tallies were used in this simulation to estimate the $4\pi$ particle flux and a particle flux within 30° from the zenith. The $4\pi$ particle fluxes were used with dose conversion coefficients defined in ICRP-123 to estimate absorbed and effective dose equivalents to an astronaut. The tally

that addressed particle flux 30° from the zenith was used to compare to MSLRAD.

It was found that the particle fluxes for light and heavy ions followed the same basic shape as the simulated source spectra for energies above 100 MeV. For ions with atomic number less than 8, it was observed that the particle fluxes diverged from their source spectra due to spallation, ionization, and down-scattering. The flux comparison with MSLRAD showed good agreement for protons, alpha particles, and neutrons but showed some disagreement with heavier ions. The integrated particle fluxes were compared for all ions tallied, and it was found that the PHITS simulations were within one standard deviation for protons, and for particles heavier than boron. Dose rates were estimated from the simulations to be 215 $\mu Gy\,d^{-1}$ whole body dose per day or an effective dose rate of 491 $\mu Sv\,d^{-1}$. This dose is much lower than dose estimates for large SPEs. It was shown that 65% of the GCR effective dose comes from source protons, while 19% comes from source alpha particles. Plotting the absorbed dose for tallied particle types show that protons, alphas particles, neutrons, photons, electrons and positrons are the significant contributors to dose at the surface. This also gave information about tally energy cut-offs which can lead to better data management for future simulations. Overall, both sets of simulations showed reasonable results and gave a great amount of information on the Martian radiation environment.

### 5.0.1 Future Work

In the future, more accurate dose estimates may be achieved by simulating the radiation environment on a computational phantom, or by developing dose conversion coefficients which consider a superior to inferior irradiating direction. From the fluences found, the radiation flux at the surface of Mars could be calculated and used to optimize a radiation shielding design for future Mars habitats. With this data, future simulations of shielding designs will have the benefit of a reduced geometry allowing for efficient shield optimization. Absorbed dose to electronic systems could also be found by developing or simulating an absorbed dose response in silicon. This would allow for future scientist to consider risks to electrical components as well as biological risks to ensure the safety of astronauts.

# Bibliography


[1] Gary Daines. NASA's Journey to Mars. 2015. URL https://www.nasa.gov/content/nasas-journey-to-mars.

[2] Donald M Hassler, Cary Zeitlin, Robert F Wimmer-Schweingruber, Bent Ehresmann, Scot Rafkin, Jennifer L Eigenbrode, David E Brinza, Gerald Weigle, Stephan Böttcher, Eckart Böhm, Soenke Burmeister, Jingnan Guo, Jan Köhler, Cesar Martin, Guenther Reitz, Francis A Cucinotta, Myung-Hee Kim, David Grinspoon, Mark A Bullock, Arik Posner, Javier Gómez-Elvira, Ashwin Vasavada, John P Grotzinger, and MSL Science MSL Science Team. Mars' surface radiation environment measured with the Mars Science Laboratory's Curiosity rover. *Science (New York, N.Y.)*, 343(6169):1244797, 1 2014. ISSN 1095-9203. doi: 10.1126/science.1244797. URL http://www.ncbi.nlm.nih.gov/pubmed/24324275.

[3] Tatsuhiko Sato. Analytical Model for Estimating the Zenith Angle Dependence of Terrestrial Cosmic Ray Fluxes. *PLos ONE*, 2016. doi: 10.1371/journal.pone.0160390. URL http://europepmc.org/backend/ptpmcrender.fcgi?accid=PMC4973932&blobtype=pdf.

[4] Camron Saul Gorguinpour, Thomas Budinger, Thomas Lang, and Robert Lin. The Impact of Solar Particle Events on Radiation Risk for Human Explorers of Mars. 2010. URL https://search.proquest.com/docview/749356739?pq-origsite=primo.

[5] Charles Lloyd and Scott Townsend. Space Radiation. URL https://www.nasa.gov/sites/default/files/atoms/files/space_radiation_ebook.pdf.

[6] Francis Cucinotta. Radiation Risk Acceptability and Limitations. 2010. URL https://three.jsc.nasa.gov/articles/AstronautRadLimitsFC.pdf.

[7] Francis A Cucinotta, Myung-Hee Y Kim, and Lori J Chappell. Space Radiation Cancer Risk Projections and Uncertainties-2012. Technical report, 2013. URL http://www.sti.nasa.gov.

[8] Jennifer Boyer, Lockheed Martin Houston, and TX Keith Holubec. NASA-STD-3001, Space Flight Human-System Standard, and the Human Integration Design Handbook. URL https://search-proquest-com.er.lib.k-state.edu/docview/1151089814/fulltextPDF/475F6AAB563C4C91PQ/1?accountid=11789.

[9] Luis Espinoza. Radiation Measurements on Mars. 2013. URL https://www.nasa.gov/jpl/msl/mars-rover-curiosity-pia17600.html#.WUq_0WjythE.

[10] Jingnan Guo, Cary Zeitlin, Robert F Wimmer-Schweingruber, Thoren Mcdole, Patrick Kühl, Jan C Appel, Daniel Matthiä, Johannes Krauss, and Jan Köhler. A generalized approach to model the spectra and radiation dose rate of solar particle events on the surface of Mars. 2017. URL https://arxiv.org/pdf/1705.06763.pdf.

[11] HZETRN, 2015. URL https://software.nasa.gov/software/LAR-18803-1.

[12] L.W. Townsend, M. PourArsalan, M.I. Hall, J.A. Anderson, S. Bhatt, N. DeLauder, and A.M. Adamczyk. Estimates of Carrington-class solar particle event radiation exposures on Mars. *Acta Astronautica*, 69(7-8):397–405, 9 2011. ISSN 0094-5765. doi: 10.1016/J.ACTAASTRO.2011.05.020. URL https://www.sciencedirect.com/science/article/pii/S0094576511001585?via%3Dihub.

[13] John W Wilson, Lawrence W Townsend, Sang Y Chun, Warren W Buck, Ferdous Khan, Frank Cucinotta, and June 1988. BRYNTRN: A Baryon Transport Computer Code Computatio7z Procedures m d Data Base BRYNTRN: A Baryon Transport Computer Code Compututiolz Procedures ulzd Dutu Base. 1988. URL https://ntrs.nasa.gov/archive/nasa/casi.ntrs.nasa.gov/19880014330.pdf.

[14] Lisa Simonsen, John Nealy, Lawrence Townsend, and John Wilson. *Radiation exposure*

*for manned Mars surface missions /*. Washington, D.C. :, 1990. URL http://hdl.handle.net/2027/uiug.30112106709527.

[15] Geant4, 2017. URL https://geant4.web.cern.ch/support/download.

[16] A. Postollec, S. Incerti, M. Dobrijevic, L. Desorgher, G. Santin, and P. Moretto. Monte Carlo simulation of the radiation environment encountered by a biochip during a space mission to Mars. *Astrobiology 9, no. 3*, 2009. URL http://go.galegroup.com.er.lib.k-state.edu/ps/i.do?id=GALE%7CA201944899&v=2.1&u=ksu&it=r&p=AONE&sw=w#.

[17] Ryan B. Norman, Guillaume Gronoff, and Christopher J. Mertens. Influence of dust loading on atmospheric ionizing radiation on Mars. *Journal of Geophysical Research: Space Physics*, 119(1):452–461, 1 2014. ISSN 21699380. doi: 10.1002/2013JA019351. URL http://doi.wiley.com/10.1002/2013JA019351.

[18] L.W. Townsend, E.N. Zapp, D.L. Stephens, and J.L. Hoff. Carrington flare of 1859 as a prototypical worst-case solar energetic particle event. *IEEE Transactions on Nuclear Science*, 50(6):2307–2309, dec 2003. ISSN 0018-9499. doi: 10.1109/TNS.2003.821602. URL http://ieeexplore.ieee.org/document/1263877/.

[19] Pasquale Blasi. Galactic Cosmic Rays. *EDP Sciences*, 2015. URL https://www.epj-conferences.org/articles/epjconf/pdf/2015/24/epjconf-SuGAR2015_00002.pdf.

[20] J. Simpson. Elemental and Isotopic Composition of the Galactic Cosmic Rays. *Ann. Rev. Nucl. Particle Sci.*, (33):323–382, 1983.

[21] Tony Slaba, Christopher Mertens, and Steve Blattnig. Radiation Shielding Optimization on Mars. *NASA/TP-2013-217983*, 2013. URL https://permanent.access.gpo.gov/gpo45816/20130012456-2013011531.pdf.

[22] Bent Ehresmann, Cary Zeitlin, Donald Hassler, and Et. al. Charged particle spectra obtained with the Mars Science Laboratory Radiation Assessment Detector (MSL/RAD)

on the surface of Mars. *Journal of Geophysical Research: Planets*, 2014. URL https://agupubs.onlinelibrary.wiley.com/doi/pdfdirect/10.1002/2013JE004547.

[23] John Flores-Mclaughlin. Radiation Transport Simulation of the Martian GCR Surface Flux and Dose Estimation Using Spherical Geometry in PHITS Compared to MSL-RAD Measurements. *Life Sciences in Space Research*, 14:36–42, 2017.

[24] Tatsuhiko Sato. Analytical Model for Estimating Terrestrial Cosmic Ray Fluxes Nearly Anytime and Anywhere in the World: Extension of PARMA/ EXPACS. *PLos ONE*, 2015. doi: 10.1371/journal.pone.0144679. URL http://europepmc.org/backend/ptpmcrender.fcgi?accid=PMC4682948&blobtype=pdf.

[25] Tatsuhiko Sato, Hiroshi Yasuda, Koji Niita, Akira Endo, and Lembit Sihver. Development of PARMA: PHITS-Based Analytical Radiation Model in the Atmosphere. *Radiation Research*, 170(2):244–259, 2008. ISSN 00337587, 19385404. URL http://www.jstor.org/stable/25167763.

[26] Karen Northon. Mars Helicopter to Fly on NASAs Next Red Planet Rover Mission. 2018. URL https://www.nasa.gov/press-release/mars-helicopter-to-fly-on-nasa-s-next-red-planet-rover-mission.

[27] T Sato, K Niita, N Matsuda, S Hashimoto, Y Iwamoto, S Noda, T Ogawa, H Iwase, H Nakashima, T Fukahori, K Okumura, T Kai, S Chiba, T Furuta, and L Sihver. Particle and Heavy Ion Transport Code System PHITS, Version 2.88, 2016.

[28] Tatsuhiko Sato, Ritsuko Watanabe, and Koji Niita. Development of a calculation method for estimating specific energy distribution in complex radiation fields. *Radiation Protection Dosimetry*, 122(1-4):41–45, dec 2006. ISSN 1742-3406. doi: 10.1093/rpd/ncl407. URL http://academic.oup.com/rpd/article/122/1-4/41/1600831/Development-of-a-calculation-method-for-estimating.

[29] Y. Nara, N. Otuka, A. Ohnishi, K. Niita, and S. Chiba. Relativistic nuclear collisions at 1 0 A GeV energies from p + Be to Au+Au with the hadronic cascade model. *Physical*

*Review C*, 61(2):024901, dec 1999. ISSN 0556-2813. doi: 10.1103/PhysRevC.61.024901. URL http://iopscience.iop.org/article/10.1088/0031-9155/54/7/009/pdf.

[30] Koji Niita, Satoshi Chiba, Toshiki Maruyama, Tomoyuki Maruyama, Hiroshi Takada, Tokio Fukahori, Yasuaki Nakahara, and Akira Iwamoto. Analysis of the ( N , xN ) reactions by quantum molecular dynamics plus statistical decay model. *Physical Review C*, 52(5):2620–2635, nov 1995. ISSN 0556-2813. doi: 10.1103/PhysRevC.52.2620. URL https://link.aps.org/doi/10.1103/PhysRevC.52.2620.

[31] Koji Niita et. al. PHITS ver. 2.88 User's Manual. 2016. URL https://phits.jaea.go.jp/manual/manualE-phits288.pdf.

[32] Yosuke Iwamoto, Tatsuhiko Sato, Shintaro Hashimoto, Tatsuhiko Ogawa, Takuya Furuta, Shin-ichiro Abe, Takeshi Kai, Norihiro Matsuda, Ryuji Hosoyamada, and Koji Niita. Benchmark study of the recent version of the PHITS code. *Journal of Nuclear Science and Technology*, 54(5):617–635, may 2017. ISSN 0022-3131. doi: 10.1080/00223131.2017.1297742. URL https://www.tandfonline.com/doi/full/10.1080/00223131.2017.1297742.

[33] Franois Forget, Francisco Gonzalez-Galindo, Sbastien Lebonnois, Jean-Loup Bertaux, Franck Montmessin, Eric Quémerais, Aurlie Reberac, Emmanuel Dimarellis, and Miguel A Lopez Valverde. The density and temperatures of the upper martian atmosphere measured by stellar occultations with Mars Express SPICAM. *Journal of Geophysical Research*, 2008. URL http://www-mars.lmd.jussieu.fr/mars/publi/forget_jgr2008.pdf.

[34] Paul Withers, R. D. Lorenz, and G. A. Neumann. Comparison of viking lander descent data and MOLA topography reveals kilometer-scale offset in Mars atmosphere profiles. *Icarus*, 159(1):259–261, 2002. ISSN 00191035. doi: 10.1006/icar.2002.6914.

[35] Validation of Mars Global Reference Atmospheric Model (Mars-GRAM 2001) and planned new features. *Advances in Space Research*, 38(11):2633–2638, 1 2006. ISSN

0273-1177. doi: 10.1016/J.ASR.2006.07.007. URL http://www.sciencedirect.com/science/article/pii/S0273117706004510?via%3Dihub.

[36] A. Keating, A. Mohammadzadeh, P. Nieminen, D. Maia, S. Coutinho, H. Evans, M. Pimenta, J. P. Huot, and E. Daly. A model for Mars radiation environment characterization. *IEEE Transactions on Nuclear Science*, 52(6):2287–2293, 2005. ISSN 00189499. doi: 10.1109/TNS.2005.860748.

[37] OLTARIS Home Page, 2013. URL https://oltaris.nasa.gov/.

[38] S. McKenna-Lawlor, P. Goncalves, A. Keating, B. Morgado, D. Heynderickx, P. Nieminen, G. Santin, P. Truscott, F. Lei, B. Foing, and J. Balaz. Characterization of the particle radiation environment at three potential landing sites on Mars using ESA's MEREM models. *Icarus*, 218(1):723–734, 2012.

[39] Tatsuhiko Sato. Fluence-to-dose conversion coefficients for neutrons and protons calculated using the PHITS code and ICRP/ICRU adult reference computational phantoms. *Phys. Med. Biol*, 54, 2009. URL http://iopscience.iop.org/article/10.1088/0031-9155/54/7/009/pdf.

[40] Hideo Hirayama, Yoshihito Namito, Alex F. Bielajew, Scott J. Wilderman, Michigan U., and Walter R. Nelson. The EGS5 Code System. Technical report, Stanford Linear Accelerator Center (SLAC), Menlo Park, CA, dec 2005. URL http://www.osti.gov/servlets/purl/877459-sHotCs/.

[41] The Martian Atmosphere. URL http://www.braeunig.us/space/atmmars.htm.

[42] Daniel Matthiä, Donald M. Hassler, Wouter de Wet, Bent Ehresmann, Ana Firan, John Flores-McLaughlin, Jingnan Guo, Lawrence H. Heilbronn, Kerry Lee, Hunter Ratliff, Ryan R. Rios, Tony C. Slaba, Michael Smith, Nicholas N. Stoffle, Lawrence W. Townsend, Thomas Berger, Robert F. Wimmer-Schweingruber, and Cary Zeitlin. The radiation environment on the surface of Mars - Summary of model calculations and comparison to RAD data. *Life Sciences in Space Research*, 14:18–28, aug 2017. ISSN

2214-5524. doi: 10.1016/J.LSSR.2017.06.003. URL https://www.sciencedirect.com/science/article/pii/S2214552417300111.

[43] Daniel Matthiae, Thomas Berger, Alankrita I., and Gunther Reitz. A ready-to-use galactic cosmic ray model. *Advances in Space Research*, 2012. URL https://www.sciencedirect.com/science/article/pii/S0273117712005947.

[44] Bent Ehresmann, Cary Zeitlin, Donald M. Hassler, Robert F. Wimmer-Schweingruber, Eckart Böhm, Stephan Böttcher, David E. Brinza, Sönke Burmeister, Jingnan Guo, Jan Köhler, Cesar Martin, Arik Posner, Scot Rafkin, and Günther Reitz. Charged particle spectra obtained with the Mars Science Laboratory Radiation Assessment Detector (MSL/RAD) on the surface of Mars. *Journal of Geophysical Research: Planets*, 119 (3):468–479, mar 2014. ISSN 21699097. doi: 10.1002/2013JE004547. URL http://doi.wiley.com/10.1002/2013JE004547.

[45] ICRP publication. 1975. ISSN 0074-2740. URL http://www.icrp.org/publication.asp?id=ICRPPublication123.

[46] Tatsuhiko Sato, Koji Niita, Norihiro Matsuda, Shintaro Hashimoto, Yosuke Iwamoto, Shusaku Noda, Tatsuhiko Ogawa, Hiroshi Iwase, Hiroshi Nakashima, Tokio Fukahori, Keisuke Okumura, Tetsuya Kai, Satoshi Chiba, Takuya Furuta, and Lembit Sihver. Particle and Heavy Ion Transport code System, PHITS, version 2.52. *Journal of Nuclear Science and Technology*, 50(9):913–923, sep 2013. ISSN 0022-3131. doi: 10.1080/00223131.2013.814553. URL http://www.tandfonline.com/doi/abs/10.1080/00223131.2013.814553.

[47] Z Robinson, J Adams, M Xapsos, and C Stauffer. Database of Episode-Integrated Solar Energetic Proton Fluences. 2018.

[48] L.W. Townsend, J.H. Adams, S.R. Blattnig, M.S. Clowdsley, D.J. Fry, I. Jun, C.D. McLeod, J.I. Minow, D.F. Moore, J.W. Norbury, R.B. Norman, D.V. Reames, N.A. Schwadron, E.J. Semones, R.C. Singleterry, T.C. Slaba, C.M. Werneth, and M.A.

Xapsos. Solar particle event storm shelter requirements for missions beyond low Earth orbit. *Life Sciences in Space Research*, 17:32–39, may 2018. ISSN 2214-5524. doi: 10.1016/J.LSSR.2018.02.002. URL https://www.sciencedirect.com/science/article/pii/S2214552417301013.

[49] ICRP. URL http://www.icrp.org/publication.asp?id=ICRPPublication60.

[50] Comparison of the mean quality factors for astronauts calculated using the Q-functions proposed by ICRP, ICRU, and NASA. *Advances in Space Research*, 52(1):79–85, 7 2013. ISSN 0273-1177. doi: 10.1016/J.ASR.2013.03.013. URL http://www.sciencedirect.com/science/article/pii/S027311771300149X?via%3Dihub.

[51] Francis A. Cucinotta. Review of NASA Approach to Space Radiation Risk Assessments for Mars Exploration. *Health Physics*, 108(2):131–142, feb 2015. ISSN 0017-9078. doi: 10.1097/HP.0000000000000255. URL http://content.wkhealth.com/linkback/openurl?sid=WKPTLP:landingpage&an=00004032-201502000-00008.

[52] R H Mole, D G Papworth, and M J Corp. The dose-response for x-ray induction of myeloid leukaemia in male CBA/H mice. *British Journal of Cancer*, 47(2):285–291, feb 1983. ISSN 0007-0920. doi: 10.1038/bjc.1983.37. URL http://www.ncbi.nlm.nih.gov/pubmed/6337614.

[53] S.D. Griffiths, S.J. Marsden, E.G. Wright, M.F. Greaves, and D.T. Goodhead. Lethality and Mutagenesis of B Lymphocyte Progenitor Cells Following Exposure to $\alpha$-particles and X-rays. *International Journal of Radiation Biology*, 66(2):197–205, jan 1994. ISSN 0955-3002. doi: 10.1080/09553009414551101. URL http://www.ncbi.nlm.nih.gov/pubmed/8089629.

[54] Solar Cycle Progression and Forecast — NASA. URL https://www.nasa.gov/msfcsolar.

# Appendix A

# Example Input File

```
[Title]
This is a simulation to find the particle flux at various altitudes in the martian atmosphere
for protons a discrete energy is assigned for each simualtion in order to obtain a response
function.

[Parameters]
icntl=0                   # Normal PHITS calculation mode
rseed = -1                # Random seed generated from starting time
maxcas   =     5000       # Number of Histories per batch
maxbch   =     1550       # Number of batches
istdev = -1
# minimum and maximum cross-section data cut-off energies
emin(1)  = 1.000000000E-03 # (D=1.0) cut-off energy of proton (MeV)
emin(2)  = 1.000000000E-10 # (D=1.0) cut-off energy of neutron (MeV)
dmax(2)  =  20.0000000     # (D=emin(2)) data max. energy of neutron (MeV)
emin(12) = 1.000000000E-01 # (D=1.d9) cut-off energy of electron (MeV)
emin(13) = 1.000000000E-01 # (D=1.d9) cut-off energy of positron (MeV)
emin(14) = 1.000000000E-03 # (D=1.d9) cut-off energy of photon (MeV)
dmax(12) =  1000.00000     # (D=emin(12)) data max. energy of electron (MeV)
dmax(13) =  1000.00000     # (D=emin(13)) data max. energy of positron (MeV)
dmax(14) =  1000.00000     # (D=emin(14)) data max. energy of photon (MeV)
emin(15) = 1.000000000E-03 # (D=1.d9) cut-off energy of deuteron (MeV)
emin(16) = 1.000000000E-03 # (D=1.d9) cut-off energy of triton (MeV)
emin(17) = 1.000000000E-03 # (D=1.d9) cut-off energy of 3He (MeV)
emin(18) = 1.000000000E-03 # (D=1.d9) cut-off energy of Alpha (MeV)
emin(19) = 1.000000000E-03 # (D=1.d9) cut-off energy of Nucleus (MeV)
e-mode   =           2     # Event generator mode (version 2.0)
itall    =           1     # Output tally after each batch
negs     =           0     # (D=0) = 1 EGS5 (Electron gamma shower 5.0) photon and electron [off]
irqmd    =           1     # Use of JQMD-2.0 in nuclear reactions (Model for high energy particles up to 200 GeV)
icxsni   =           2     # Nucleon-Nucleus collisions (Satos formula)
nspred   =           0     # Angular straggling (Lynch's formula) [off]
nedisp   =           0     # Energy straggling (Landau-Vavilov) [off]
nlost    =       10000     # Number of particles that may be lost (generously set)
MDBATIMA =        5000     # Maximum database size for stopping power calculation
# Different directories based on system/beocat
file(6)  = phits_test.out                          # Name for error file if failure
file(7)  = /homes/mike5454/phits/data/xsdir.jnd    # Directory for cross-section data
file(20) = /homes/mike5454/phits/XS/egs            # Directory for EGS5 algorithm

[Source]
s-type = 9                                # Source defined as spherical shell source
proj = proton                             # Particle type proton
# sphere center location
x0 = 0
y0 = 0
z0 = 0
# r1 = r2 for truely isotropic source
r1 = 350750675.0                          # Size of Mars with atmosphere
r2 = 350750675.0                          # Size of Mars with atmosphere
totfact = pi * 350750675.0 * 350750675.0  # Source normalization
dir = iso                                 # Inward isotropic source defined
   e0 = 1.0                               # Mono-energetic source (Changing with input)

[Material]
```

```
# Materials are defined in ZAID format using mass fractions
# MARS Atmosphere using earth isotope abundances
#   (density calculated from Mars Climate Database - altitude discritization)
m1    6012    -0.263965188671
          7014    -0.0173629494665
          7015    -6.41316585402E-05
          8016    -0.703880847672
         18040    -0.0147268825313
#
# MARS Regolith using earth isotope abundances
#  (density = 1.7 g/cm^3 from OLTARIS)
m2         1001    -0.000927870434089
         1002    -1.06717372418E-07
         8016    -0.360694192643
        11023    -0.0918189076912
        12024    -0.0383381272244
        12025    -0.00485354186915
        12026    -0.00534374959793
        13027    -0.107762408322
        14028    -0.0825066152678
        14029    -0.00418948538944
        14030    -0.00276165022756
        19039    -0.0894577508848
        19040    -0.145624435891
        19041    -1.82697899691E-05
        20040    -0.0105093453376
        20042    -0.0775848082916
        20043    -0.000517813628543
        20044    -0.000108044574735
        20046    -0.0016694887622
        20048    -3.20132073288E-06
        26054    -0.000149661744262
        26056    -0.0037769381899
        26057    -0.059289852297
        26058    -0.0013692612531

[Importance]
part = all          # Define importance for all particles
# proton neutron deuteron triton 3he alpha electron positron muon+ muon- pion+ pion- pion0
  reg      imp
   1        0        # Importance equal to zero in inner graveyard region

[Surface]
# Surface Card (Define bounding surfaces)
# ****************** MARS ATMOSPHERE **********************
#  Spheres at Origin    Radius (cm)
#
9894        so            338234175.0
9895        so            338234225.0
9896        so            338234250.0
9897        so            338234275.0
9898        so            338234300.0
9899        so            338234325.0
9900        so            338234350.0
9901        so            338234375.0
9902        so            338234400.0
9903        so            338234425.0
9904        so            338234450.0
9905        so            338234475.0
9906        so            338234500.0
9907        so            338234525.0
9908        so            338234550.0
9909        so            338234575.0
9910        so            338234600.0
9911        so            338234625.0
9912        so            338234650.0
9913        so            338234675.0
9914        so            338234700.0
9915        so            338234725.0
9916        so            338234750.0
9917        so            338234775.0
9918        so            338234800.0
9919        so            338268425.0
9920        so            338302050.0
9921        so            338336950.0
9922        so            338371850.0
9923        so            338408075.0
9924        so            338444300.0
9925        so            338481962.5
9926        so            338519625.0
9927        so            338558862.5
9928        so            338598100.0
9929        so            338639025.0
9930        so            338679950.0
9931        so            338722725.0
9932        so            338765500.0
9933        so            338810300.0
9934        so            338855100.0
9935        so            338902125.0
9936        so            338949150.0
```

```
9937        so            338998637.5
9938        so            339048125.0
9939        so            339100362.5
9940        so            339152600.0
9941        so            339208250.0
9942        so            339263900.0
9943        so            339323600.0
9944        so            339383300.0
9945        so            339447900.0
9946        so            339512500.0
9947        so            339583087.5
9948        so            339653675.0
9949        so            339731712.5
9950        so            339809750.0
9951        so            339898025.0
9952        so            339986300.0
9953        so            340088637.5
9954        so            340190975.0
9955        so            340314225.0
9956        so            340437475.0
9957        so            340593962.5
9958        so            340750450.0
9959        so            341000562.5
9960        so            341250675.0
9961        so            341500675.0
9962        so            341750675.0
9963        so            342000675.0
9964        so            342250675.0
9965        so            342500675.0
9966        so            342750675.0
9967        so            343000675.0
9968        so            343250675.0
9969        so            343500675.0
9970        so            343750675.0
9971        so            344000675.0
9972        so            344250675.0
9973        so            344500675.0
9974        so            344750675.0
9975        so            345000675.0
9976        so            345250675.0
9977        so            345500675.0
9978        so            345750675.0
9979        so            346000675.0
9980        so            346250675.0
9981        so            346500675.0
9982        so            346750675.0
9983        so            347000675.0
9984        so            347250675.0
9985        so            347500675.0
9986        so            347750675.0
9987        so            348000675.0
9988        so            348250675.0
9989        so            348500675.0
9990        so            348750675.0
9991        so            349000675.0
9992        so            349250675.0
9993        so            349500675.0
9994        so            349750675.0
9995        so            350000675.0
9996        so            350250675.0
9997        so            350500675.0
9998        so            350750675.0
9999        so            496036412.0

[Cell]
# Cell Card (Define cells constrained by surfaces)
# ***************** CELL CARD ***************************
# Cell / Material / Density / Boundaries
#
1   -1       -9894
2    2  -1.7  9894  -9895                    # Regolith
3    2  -1.7  9895  -9896                    # Regolith
4    2  -1.7  9896  -9897                    # Regolith
5    2  -1.7  9897  -9898                    # Regolith
6    2  -1.7  9898  -9899                    # Regolith
7    2  -1.7  9899  -9900                    # Regolith
8    2  -1.7  9900  -9901                    # Regolith
9    2  -1.7  9901  -9902                    # Regolith
10   2  -1.7  9902  -9903                    # Regolith
11   2  -1.7  9903  -9904                    # Regolith
12   2  -1.7  9904  -9905                    # Regolith
13   2  -1.7  9905  -9906                    # Regolith
14   2  -1.7  9906  -9907                    # Regolith
15   2  -1.7  9907  -9908                    # Regolith
16   2  -1.7  9908  -9909                    # Regolith
17   2  -1.7  9909  -9910                    # Regolith
18   2  -1.7  9910  -9911                    # Regolith
19   2  -1.7  9911  -9912                    # Regolith
20   2  -1.7  9912  -9913                    # Regolith
21   2  -1.7  9913  -9914                    # Regolith
```

```
22   2  -1.7  9914  -9915                    # Regolith
23   2  -1.7  9915  -9916                    # Regolith
24   2  -1.7  9916  -9917                    # Regolith
25   2  -1.7  9917  -9918                    # Regolith
26   1  -1.485760624e-05  9918  -9919       # Datum -- Surface 9918
27   1  -1.485760624e-05  9919  -9920       # Atmosphere
28   1  -1.432939155e-05  9920  -9921       # Atmosphere
29   1  -1.432939155e-05  9921  -9922       # Atmosphere
30   1  -1.380098741e-05  9922  -9923       # Atmosphere
31   1  -1.380098741e-05  9923  -9924       # Atmosphere
32   1  -1.327259754e-05  9924  -9925       # Atmosphere
33   1  -1.327259754e-05  9925  -9926       # Atmosphere
34   1  -1.274422492e-05  9926  -9927       # Atmosphere
35   1  -1.274422492e-05  9927  -9928       # Atmosphere
36   1  -1.221589554e-05  9928  -9929       # Atmosphere
37   1  -1.221589554e-05  9929  -9930       # Atmosphere
38   1  -1.168753024e-05  9930  -9931       # Atmosphere
39   1  -1.168753024e-05  9931  -9932       # Atmosphere
40   1  -1.115915159e-05  9932  -9933       # Atmosphere
41   1  -1.115915159e-05  9933  -9934       # Atmosphere
42   1  -1.063076618e-05  9934  -9935       # Atmosphere
43   1  -1.063076618e-05  9935  -9936       # Atmosphere
44   1  -1.010228637e-05  9936  -9937       # Atmosphere
45   1  -1.010228637e-05  9937  -9938       # Atmosphere
46   1  -9.573743625e-06  9938  -9939       # Atmosphere
47   1  -9.573743625e-06  9939  -9940       # Atmosphere
48   1  -8.984144652e-06  9940  -9941       # Atmosphere
49   1  -8.984144652e-06  9941  -9942       # Atmosphere
50   1  -8.373625844e-06  9942  -9943       # Atmosphere
51   1  -8.373625844e-06  9943  -9944       # Atmosphere
52   1  -7.737976073e-06  9944  -9945       # Atmosphere
53   1  -7.737976073e-06  9945  -9946       # Atmosphere
54   1  -7.081024914e-06  9946  -9947       # Atmosphere
55   1  -7.081024914e-06  9947  -9948       # Atmosphere
56   1  -6.405336681e-06  9948  -9949       # Atmosphere
57   1  -6.405336681e-06  9949  -9950       # Atmosphere
58   1  -5.659916016e-06  9950  -9951       # Atmosphere
59   1  -5.659916016e-06  9951  -9952       # Atmosphere
60   1  -4.881430151e-06  9952  -9953       # Atmosphere
61   1  -4.881430151e-06  9953  -9954       # Atmosphere
62   1  -4.049499133e-06  9954  -9955       # Atmosphere
63   1  -4.049499133e-06  9955  -9956       # Atmosphere
64   1  -3.191881135e-06  9956  -9957       # Atmosphere
65   1  -3.191881135e-06  9957  -9958       # Atmosphere
66   1  -2.189359028e-06  9958  -9959       # Atmosphere
67   1  -2.189359028e-06  9959  -9960       # Atmosphere
68   1  -1.346059075e-06  9960  -9961       # Atmosphere
69   1  -1.346059075e-06  9961  -9962       # Atmosphere
70   1  -8.036402089e-07  9962  -9963       # Atmosphere
71   1  -8.036402089e-07  9963  -9964       # Atmosphere
72   1  -4.673739908e-07  9964  -9965       # Atmosphere
73   1  -4.673739908e-07  9965  -9966       # Atmosphere
74   1  -2.668835877e-07  9966  -9967       # Atmosphere
75   1  -2.668835877e-07  9967  -9968       # Atmosphere
76   1  -1.509559602e-07  9968  -9969       # Atmosphere
77   1  -1.509559602e-07  9969  -9970       # Atmosphere
78   1  -8.512657190e-08  9970  -9971       # Atmosphere
79   1  -8.512657190e-08  9971  -9972       # Atmosphere
80   1  -4.844450090e-08  9972  -9973       # Atmosphere
81   1  -4.844450090e-08  9973  -9974       # Atmosphere
82   1  -2.734625093e-08  9974  -9975       # Atmosphere
83   1  -2.734625093e-08  9975  -9976       # Atmosphere
84   1  -1.515135283e-08  9976  -9977       # Atmosphere
85   1  -1.515135283e-08  9977  -9978       # Atmosphere
86   1  -8.349037314e-09  9978  -9979       # Atmosphere
87   1  -8.349037314e-09  9979  -9980       # Atmosphere
88   1  -4.673439000e-09  9980  -9981       # Atmosphere
89   1  -4.673439000e-09  9981  -9982       # Atmosphere
90   1  -2.575922201e-09  9982  -9983       # Atmosphere
91   1  -2.575922201e-09  9983  -9984       # Atmosphere
92   1  -1.370571801e-09  9984  -9985       # Atmosphere
93   1  -1.370571801e-09  9985  -9986       # Atmosphere
94   1  -7.134277065e-10  9986  -9987       # Atmosphere
95   1  -7.134277065e-10  9987  -9988       # Atmosphere
96   1  -3.783154188e-10  9988  -9989       # Atmosphere
97   1  -3.783154188e-10  9989  -9990       # Atmosphere
98   1  -1.97853357e0-10  9990  -9991       # Atmosphere
99   1  -1.978533570e-10  9991  -9992       # Atmosphere
100  1  -1.015760195e-10  9992  -9993       # Atmosphere
101  1  -1.015760195e-10  9993  -9994       # Atmosphere
102  1  -5.123688029e-11  9994  -9995       # Atmosphere
103  1  -5.123688029e-11  9995  -9996       # Atmosphere
104  1  -2.482706772e-11  9996  -9997       # Atmosphere
105  1  -2.482706772e-11  9997  -9998       # Atmosphere
106  0     9998  -9999                      # Vacuum
107 -1       9999                          # Graveyard

[Volume]
# Volume of the cells calculated using (4/3)*pi*(R2-R1)
# Values defined in the surface card
```

```
reg vol
3     [(4/3)*pi*(338234250.0**3-338234225.0**3)]
4     [(4/3)*pi*(338234275.0**3-338234250.0**3)]
5     [(4/3)*pi*(338234300.0**3-338234275.0**3)]
6     [(4/3)*pi*(338234325.0**3-338234300.0**3)]
7     [(4/3)*pi*(338234350.0**3-338234325.0**3)]
8     [(4/3)*pi*(338234375.0**3-338234350.0**3)]
9     [(4/3)*pi*(338234400.0**3-338234375.0**3)]
10    [(4/3)*pi*(338234425.0**3-338234400.0**3)]
11    [(4/3)*pi*(338234450.0**3-338234425.0**3)]
12    [(4/3)*pi*(338234475.0**3-338234450.0**3)]
13    [(4/3)*pi*(338234500.0**3-338234475.0**3)]
14    [(4/3)*pi*(338234525.0**3-338234500.0**3)]
15    [(4/3)*pi*(338234550.0**3-338234525.0**3)]
16    [(4/3)*pi*(338234575.0**3-338234550.0**3)]
17    [(4/3)*pi*(338234600.0**3-338234575.0**3)]
18    [(4/3)*pi*(338234625.0**3-338234600.0**3)]
19    [(4/3)*pi*(338234650.0**3-338234625.0**3)]
20    [(4/3)*pi*(338234675.0**3-338234650.0**3)]
21    [(4/3)*pi*(338234700.0**3-338234675.0**3)]
22    [(4/3)*pi*(338234725.0**3-338234700.0**3)]
23    [(4/3)*pi*(338234750.0**3-338234725.0**3)]
24    [(4/3)*pi*(338234775.0**3-338234750.0**3)]
25    [(4/3)*pi*(338234800.0**3-338234775.0**3)]
26    [(4/3)*pi*(338268425.0**3-338234800.0**3)]
27    [(4/3)*pi*(338302050.0**3-338268425.0**3)]
28    [(4/3)*pi*(338336950.0**3-338302050.0**3)]
29    [(4/3)*pi*(338371850.0**3-338336950.0**3)]
30    [(4/3)*pi*(338408075.0**3-338371850.0**3)]
31    [(4/3)*pi*(338444300.0**3-338408075.0**3)]
32    [(4/3)*pi*(338481962.5**3-338444300.0**3)]
33    [(4/3)*pi*(338519625.0**3-338481962.5**3)]
34    [(4/3)*pi*(338558862.5**3-338519625.0**3)]
35    [(4/3)*pi*(338598100.0**3-338558862.5**3)]
36    [(4/3)*pi*(338639025.0**3-338598100.0**3)]
37    [(4/3)*pi*(338679950.0**3-338639025.0**3)]
38    [(4/3)*pi*(338722725.0**3-338679950.0**3)]
39    [(4/3)*pi*(338765500.0**3-338722725.0**3)]
40    [(4/3)*pi*(338810300.0**3-338765500.0**3)]
41    [(4/3)*pi*(338855100.0**3-338810300.0**3)]
42    [(4/3)*pi*(338902125.0**3-338855100.0**3)]
43    [(4/3)*pi*(338949150.0**3-338902125.0**3)]
44    [(4/3)*pi*(338998637.5**3-338949150.0**3)]
45    [(4/3)*pi*(339048125.0**3-338998637.5**3)]
46    [(4/3)*pi*(339100362.5**3-339048125.0**3)]
47    [(4/3)*pi*(339152600.0**3-339100362.5**3)]
48    [(4/3)*pi*(339208250.0**3-339152600.0**3)]
49    [(4/3)*pi*(339263900.0**3-339208250.0**3)]
50    [(4/3)*pi*(339323600.0**3-339263900.0**3)]
51    [(4/3)*pi*(339383300.0**3-339323600.0**3)]
52    [(4/3)*pi*(339447900.0**3-339383300.0**3)]
53    [(4/3)*pi*(339512500.0**3-339447900.0**3)]
54    [(4/3)*pi*(339583087.5**3-339512500.0**3)]
55    [(4/3)*pi*(339653675.0**3-339583087.5**3)]
56    [(4/3)*pi*(339731712.5**3-339653675.0**3)]
57    [(4/3)*pi*(339809750.0**3-339731712.5**3)]
58    [(4/3)*pi*(339898025.0**3-339809750.0**3)]
59    [(4/3)*pi*(339986300.0**3-339898025.0**3)]
60    [(4/3)*pi*(340088637.5**3-339986300.0**3)]
61    [(4/3)*pi*(340190975.0**3-340088637.5**3)]
62    [(4/3)*pi*(340314225.0**3-340190975.0**3)]
63    [(4/3)*pi*(340437475.0**3-340314225.0**3)]
64    [(4/3)*pi*(340593962.5**3-340437475.0**3)]
65    [(4/3)*pi*(340750450.0**3-340593962.5**3)]
66    [(4/3)*pi*(341000562.5**3-340750450.0**3)]
67    [(4/3)*pi*(341250675.0**3-341000562.5**3)]
68    [(4/3)*pi*(341500675.0**3-341250675.0**3)]
69    [(4/3)*pi*(341750675.0**3-341500675.0**3)]
70    [(4/3)*pi*(342000675.0**3-341750675.0**3)]
71    [(4/3)*pi*(342250675.0**3-342000675.0**3)]
72    [(4/3)*pi*(342500675.0**3-342250675.0**3)]
73    [(4/3)*pi*(342750675.0**3-342500675.0**3)]
74    [(4/3)*pi*(343000675.0**3-342750675.0**3)]
75    [(4/3)*pi*(343250675.0**3-343000675.0**3)]
76    [(4/3)*pi*(343500675.0**3-343250675.0**3)]
77    [(4/3)*pi*(343750675.0**3-343500675.0**3)]
78    [(4/3)*pi*(344000675.0**3-343750675.0**3)]
```

```
79    [(4/3)*pi*(344250675.0**3-344000675.0**3)]
80    [(4/3)*pi*(344500675.0**3-344250675.0**3)]
81    [(4/3)*pi*(344750675.0**3-344500675.0**3)]
82    [(4/3)*pi*(345000675.0**3-344750675.0**3)]
83    [(4/3)*pi*(345250675.0**3-345000675.0**3)]
84    [(4/3)*pi*(345500675.0**3-345250675.0**3)]
85    [(4/3)*pi*(345750675.0**3-345500675.0**3)]
86    [(4/3)*pi*(346000675.0**3-345750675.0**3)]
87    [(4/3)*pi*(346250675.0**3-346000675.0**3)]
88    [(4/3)*pi*(346500675.0**3-346250675.0**3)]
89    [(4/3)*pi*(346750675.0**3-346500675.0**3)]
90    [(4/3)*pi*(347000675.0**3-346750675.0**3)]
91    [(4/3)*pi*(347250675.0**3-347000675.0**3)]
92    [(4/3)*pi*(347500675.0**3-347250675.0**3)]
93    [(4/3)*pi*(347750675.0**3-347500675.0**3)]
94    [(4/3)*pi*(348000675.0**3-347750675.0**3)]
95    [(4/3)*pi*(348250675.0**3-348000675.0**3)]
96    [(4/3)*pi*(348500675.0**3-348250675.0**3)]
97    [(4/3)*pi*(348750675.0**3-348500675.0**3)]
98    [(4/3)*pi*(349000675.0**3-348750675.0**3)]
99    [(4/3)*pi*(349250675.0**3-349000675.0**3)]
100   [(4/3)*pi*(349500675.0**3-349250675.0**3)]
101   [(4/3)*pi*(349750675.0**3-349500675.0**3)]
102   [(4/3)*pi*(350000675.0**3-349750675.0**3)]
103   [(4/3)*pi*(350250675.0**3-350000675.0**3)]
104   [(4/3)*pi*(350500675.0**3-350250675.0**3)]
105   [(4/3)*pi*(350750675.0**3-350500675.0**3)]

[T-cross]
# For Proton and Neutrons applicable energies are 0.01eV to 1E5eV
# Other particles 1 to 1E5 MeV
# Corrections applied for mass of the particle in the case of deuterons Helium nuclei and tritons
mesh = reg   # Type - regions
reg = 126    # 126 tallies for each particle type
# r-in and r-out (surface-in to surface-out) alternating to capture forward and backward current
 r-in   r-out   area
  3       4      (pi*338234250.0**2)
  4       3      (pi*338234250.0**2)
  4       5      (pi*338234275.0**2)
  5       4      (pi*338234275.0**2)
  5       6      (pi*338234300.0**2)
  6       5      (pi*338234300.0**2)
  6       7      (pi*338234325.0**2)
  7       6      (pi*338234325.0**2)
  7       8      (pi*338234350.0**2)
  8       7      (pi*338234350.0**2)
  8       9      (pi*338234375.0**2)
  9       8      (pi*338234375.0**2)
  9       10     (pi*338234400.0**2)
  10      9      (pi*338234400.0**2)
  10      11     (pi*338234425.0**2)
  11      10     (pi*338234425.0**2)
  11      12     (pi*338234450.0**2)
  12      11     (pi*338234450.0**2)
  12      13     (pi*338234475.0**2)
  13      12     (pi*338234475.0**2)
  13      14     (pi*338234500.0**2)
  14      13     (pi*338234500.0**2)
  14      15     (pi*338234525.0**2)
  15      14     (pi*338234525.0**2)
  15      16     (pi*338234550.0**2)
  16      15     (pi*338234550.0**2)
  16      17     (pi*338234575.0**2)
  17      16     (pi*338234575.0**2)
  17      18     (pi*338234600.0**2)
  18      17     (pi*338234600.0**2)
  18      19     (pi*338234625.0**2)
  19      18     (pi*338234625.0**2)
  19      20     (pi*338234650.0**2)
  20      19     (pi*338234650.0**2)
  20      21     (pi*338234675.0**2)
  21      20     (pi*338234675.0**2)
  21      22     (pi*338234700.0**2)
  22      21     (pi*338234700.0**2)
  22      23     (pi*338234725.0**2)
  23      22     (pi*338234725.0**2)
  23      24     (pi*338234750.0**2)
  24      23     (pi*338234750.0**2)
```

```
24      25      (pi*338234775.0**2)
25      24      (pi*338234775.0**2)
25      26      (pi*338234800.0**2)
26      25      (pi*338234800.0**2)
26      27      (pi*338268425.0**2)
27      26      (pi*338268425.0**2)
28      29      (pi*338336950.0**2)
29      28      (pi*338336950.0**2)
30      31      (pi*338408075.0**2)
31      30      (pi*338408075.0**2)
32      33      (pi*338481962.5**2)
33      32      (pi*338481962.5**2)
34      35      (pi*338558862.5**2)
35      34      (pi*338558862.5**2)
36      37      (pi*338639025.0**2)
37      36      (pi*338639025.0**2)
38      39      (pi*338722725.0**2)
39      38      (pi*338722725.0**2)
40      41      (pi*338810300.0**2)
41      40      (pi*338810300.0**2)
42      43      (pi*338902125.0**2)
43      42      (pi*338902125.0**2)
44      45      (pi*338998637.5**2)
45      44      (pi*338998637.5**2)
46      47      (pi*339100362.5**2)
47      46      (pi*339100362.5**2)
48      49      (pi*339208250.0**2)
49      48      (pi*339208250.0**2)
50      51      (pi*339323600.0**2)
51      50      (pi*339323600.0**2)
52      53      (pi*339447900.0**2)
53      52      (pi*339447900.0**2)
54      55      (pi*339583087.5**2)
55      54      (pi*339583087.5**2)
56      57      (pi*339731712.5**2)
57      56      (pi*339731712.5**2)
58      59      (pi*339898025.0**2)
59      58      (pi*339898025.0**2)
60      61      (pi*340088637.5**2)
61      60      (pi*340088637.5**2)
62      63      (pi*340314225.0**2)
63      62      (pi*340314225.0**2)
64      65      (pi*340593962.5**2)
65      64      (pi*340593962.5**2)
66      67      (pi*341000562.5**2)
67      66      (pi*341000562.5**2)
68      69      (pi*341500675.0**2)
69      68      (pi*341500675.0**2)
70      71      (pi*342000675.0**2)
71      70      (pi*342000675.0**2)
72      73      (pi*342500675.0**2)
73      72      (pi*342500675.0**2)
74      75      (pi*343000675.0**2)
75      74      (pi*343000675.0**2)
76      77      (pi*343500675.0**2)
77      76      (pi*343500675.0**2)
78      79      (pi*344000675.0**2)
79      78      (pi*344000675.0**2)
80      81      (pi*344500675.0**2)
81      80      (pi*344500675.0**2)
82      83      (pi*345000675.0**2)
83      82      (pi*345000675.0**2)
84      85      (pi*345500675.0**2)
85      84      (pi*345500675.0**2)
86      87      (pi*346000675.0**2)
87      86      (pi*346000675.0**2)
88      89      (pi*346500675.0**2)
89      88      (pi*346500675.0**2)
90      91      (pi*347000675.0**2)
91      90      (pi*347000675.0**2)
92      93      (pi*347500675.0**2)
93      92      (pi*347500675.0**2)
94      95      (pi*348000675.0**2)
95      94      (pi*348000675.0**2)
96      97      (pi*348500675.0**2)
97      96      (pi*348500675.0**2)
98      99      (pi*349000675.0**2)
```

```
  99      98     (pi*349000675.0**2)
  100     101    (pi*349500675.0**2)
  101     100    (pi*349500675.0**2)
  102     103    (pi*350000675.0**2)
  103     102    (pi*350000675.0**2)
  104     105    (pi*350500675.0**2)
  105     104    (pi*350500675.0**2)
# Energy min, max, and number of groups divided by log scale (10 per decade)
e-type = 3
ne = 130
emin = 1E-8
emax = 1E5
part = neutron proton    # Particle type grouped by mass
unit = 5                 # Units in 1/cm^2/MeV/sr/source
a-type = -2              # Angle mesh in theta divided equally on linear scale (0-30, 30-60, 60-90)
na = 3
amin = 0
amax = 90
axis = reg
output = a-curr          # Output (non-integrated) angle mesh current by surface crossing
ginfo=1                  # Perform geometry check to detect any issues
file = flux_results_proton_neutron.dat   # Name the tally output file

[T-cross]
# Repeated for all other particle groupings
mesh = reg
reg = 126
 r-in   r-out   area
  3       4     (pi*338234250.0**2)
  4       3     (pi*338234250.0**2)
  4       5     (pi*338234275.0**2)
  5       4     (pi*338234275.0**2)
  5       6     (pi*338234300.0**2)
  6       5     (pi*338234300.0**2)
  6       7     (pi*338234325.0**2)
  7       6     (pi*338234325.0**2)
  7       8     (pi*338234350.0**2)
  8       7     (pi*338234350.0**2)
  8       9     (pi*338234375.0**2)
  9       8     (pi*338234375.0**2)
  9      10     (pi*338234400.0**2)
  10      9     (pi*338234400.0**2)
  10     11     (pi*338234425.0**2)
  11     10     (pi*338234425.0**2)
  11     12     (pi*338234450.0**2)
  12     11     (pi*338234450.0**2)
  12     13     (pi*338234475.0**2)
  13     12     (pi*338234475.0**2)
  13     14     (pi*338234500.0**2)
  14     13     (pi*338234500.0**2)
  14     15     (pi*338234525.0**2)
  15     14     (pi*338234525.0**2)
  15     16     (pi*338234550.0**2)
  16     15     (pi*338234550.0**2)
  16     17     (pi*338234575.0**2)
  17     16     (pi*338234575.0**2)
  17     18     (pi*338234600.0**2)
  18     17     (pi*338234600.0**2)
  18     19     (pi*338234625.0**2)
  19     18     (pi*338234625.0**2)
  19     20     (pi*338234650.0**2)
  20     19     (pi*338234650.0**2)
  20     21     (pi*338234675.0**2)
  21     20     (pi*338234675.0**2)
  21     22     (pi*338234700.0**2)
  22     21     (pi*338234700.0**2)
  22     23     (pi*338234725.0**2)
  23     22     (pi*338234725.0**2)
  23     24     (pi*338234750.0**2)
  24     23     (pi*338234750.0**2)
  24     25     (pi*338234775.0**2)
  25     24     (pi*338234775.0**2)
  25     26     (pi*338234800.0**2)
  26     25     (pi*338234800.0**2)
  26     27     (pi*338268425.0**2)
  27     26     (pi*338268425.0**2)
  28     29     (pi*338336950.0**2)
  29     28     (pi*338336950.0**2)
  30     31     (pi*338408075.0**2)
  31     30     (pi*338408075.0**2)
```

```
  32      33     (pi*338481962.5**2)
  33      32     (pi*338481962.5**2)
  34      35     (pi*338558862.5**2)
  35      34     (pi*338558862.5**2)
  36      37     (pi*338639025.0**2)
  37      36     (pi*338639025.0**2)
  38      39     (pi*338722725.0**2)
  39      38     (pi*338722725.0**2)
  40      41     (pi*338810300.0**2)
  41      40     (pi*338810300.0**2)
  42      43     (pi*338902125.0**2)
  43      42     (pi*338902125.0**2)
  44      45     (pi*338998637.5**2)
  45      44     (pi*338998637.5**2)
  46      47     (pi*339100362.5**2)
  47      46     (pi*339100362.5**2)
  48      49     (pi*339208250.0**2)
  49      48     (pi*339208250.0**2)
  50      51     (pi*339323600.0**2)
  51      50     (pi*339323600.0**2)
  52      53     (pi*339447900.0**2)
  53      52     (pi*339447900.0**2)
  54      55     (pi*339583087.5**2)
  55      54     (pi*339583087.5**2)
  56      57     (pi*339731712.5**2)
  57      56     (pi*339731712.5**2)
  58      59     (pi*339898025.0**2)
  59      58     (pi*339898025.0**2)
  60      61     (pi*340088637.5**2)
  61      60     (pi*340088637.5**2)
  62      63     (pi*340314225.0**2)
  63      62     (pi*340314225.0**2)
  64      65     (pi*340593962.5**2)
  65      64     (pi*340593962.5**2)
  66      67     (pi*341000562.5**2)
  67      66     (pi*341000562.5**2)
  68      69     (pi*341500675.0**2)
  69      68     (pi*341500675.0**2)
  70      71     (pi*342000675.0**2)
  71      70     (pi*342000675.0**2)
  72      73     (pi*342500675.0**2)
  73      72     (pi*342500675.0**2)
  74      75     (pi*343000675.0**2)
  75      74     (pi*343000675.0**2)
  76      77     (pi*343500675.0**2)
  77      76     (pi*343500675.0**2)
  78      79     (pi*344000675.0**2)
  79      78     (pi*344000675.0**2)
  80      81     (pi*344500675.0**2)
  81      80     (pi*344500675.0**2)
  82      83     (pi*345000675.0**2)
  83      82     (pi*345000675.0**2)
  84      85     (pi*345500675.0**2)
  85      84     (pi*345500675.0**2)
  86      87     (pi*346000675.0**2)
  87      86     (pi*346000675.0**2)
  88      89     (pi*346500675.0**2)
  89      88     (pi*346500675.0**2)
  90      91     (pi*347000675.0**2)
  91      90     (pi*347000675.0**2)
  92      93     (pi*347500675.0**2)
  93      92     (pi*347500675.0**2)
  94      95     (pi*348000675.0**2)
  95      94     (pi*348000675.0**2)
  96      97     (pi*348500675.0**2)
  97      96     (pi*348500675.0**2)
  98      99     (pi*349000675.0**2)
  99      98     (pi*349000675.0**2)
  100     101    (pi*349500675.0**2)
  101     100    (pi*349500675.0**2)
  102     103    (pi*350000675.0**2)
  103     102    (pi*350000675.0**2)
  104     105    (pi*350500675.0**2)
  105     104    (pi*350500675.0**2)
e-type = 3
ne = 50
emin = 2
emax = 2E5
```

```
part = deuteron
unit = 5
a-type = -2
na = 3
amin = 0
amax = 90
axis = reg
output = a-curr
file = flux_results_deuteron.dat

[T-cross]
mesh = reg
reg = 126
 r-in   r-out   area
  3        4     (pi*338234250.0**2)
  4        3     (pi*338234250.0**2)
  4        5     (pi*338234275.0**2)
  5        4     (pi*338234275.0**2)
  5        6     (pi*338234300.0**2)
  6        5     (pi*338234300.0**2)
  6        7     (pi*338234325.0**2)
  7        6     (pi*338234325.0**2)
  7        8     (pi*338234350.0**2)
  8        7     (pi*338234350.0**2)
  8        9     (pi*338234375.0**2)
  9        8     (pi*338234375.0**2)
  9       10     (pi*338234400.0**2)
  10       9     (pi*338234400.0**2)
  10      11     (pi*338234425.0**2)
  11      10     (pi*338234425.0**2)
  11      12     (pi*338234450.0**2)
  12      11     (pi*338234450.0**2)
  12      13     (pi*338234475.0**2)
  13      12     (pi*338234475.0**2)
  13      14     (pi*338234500.0**2)
  14      13     (pi*338234500.0**2)
  14      15     (pi*338234525.0**2)
  15      14     (pi*338234525.0**2)
  15      16     (pi*338234550.0**2)
  16      15     (pi*338234550.0**2)
  16      17     (pi*338234575.0**2)
  17      16     (pi*338234575.0**2)
  17      18     (pi*338234600.0**2)
  18      17     (pi*338234600.0**2)
  18      19     (pi*338234625.0**2)
  19      18     (pi*338234625.0**2)
  19      20     (pi*338234650.0**2)
  20      19     (pi*338234650.0**2)
  20      21     (pi*338234675.0**2)
  21      20     (pi*338234675.0**2)
  21      22     (pi*338234700.0**2)
  22      21     (pi*338234700.0**2)
  22      23     (pi*338234725.0**2)
  23      22     (pi*338234725.0**2)
  23      24     (pi*338234750.0**2)
  24      23     (pi*338234750.0**2)
  24      25     (pi*338234775.0**2)
  25      24     (pi*338234775.0**2)
  25      26     (pi*338234800.0**2)
  26      25     (pi*338234800.0**2)
  26      27     (pi*338268425.0**2)
  27      26     (pi*338268425.0**2)
  28      29     (pi*338336950.0**2)
  29      28     (pi*338336950.0**2)
  30      31     (pi*338408075.0**2)
  31      30     (pi*338408075.0**2)
  32      33     (pi*338481962.5**2)
  33      32     (pi*338481962.5**2)
  34      35     (pi*338558862.5**2)
  35      34     (pi*338558862.5**2)
  36      37     (pi*338639025.0**2)
  37      36     (pi*338639025.0**2)
  38      39     (pi*338722725.0**2)
  39      38     (pi*338722725.0**2)
  40      41     (pi*338810300.0**2)
  41      40     (pi*338810300.0**2)
  42      43     (pi*338902125.0**2)
  43      42     (pi*338902125.0**2)
  44      45     (pi*338998637.5**2)
```

```
  45      44     (pi*338998637.5**2)
  46      47     (pi*339100362.5**2)
  47      46     (pi*339100362.5**2)
  48      49     (pi*339208250.0**2)
  49      48     (pi*339208250.0**2)
  50      51     (pi*339323600.0**2)
  51      50     (pi*339323600.0**2)
  52      53     (pi*339447900.0**2)
  53      52     (pi*339447900.0**2)
  54      55     (pi*339583087.5**2)
  55      54     (pi*339583087.5**2)
  56      57     (pi*339731712.5**2)
  57      56     (pi*339731712.5**2)
  58      59     (pi*339898025.0**2)
  59      58     (pi*339898025.0**2)
  60      61     (pi*340088637.5**2)
  61      60     (pi*340088637.5**2)
  62      63     (pi*340314225.0**2)
  63      62     (pi*340314225.0**2)
  64      65     (pi*340593962.5**2)
  65      64     (pi*340593962.5**2)
  66      67     (pi*341000562.5**2)
  67      66     (pi*341000562.5**2)
  68      69     (pi*341500675.0**2)
  69      68     (pi*341500675.0**2)
  70      71     (pi*342000675.0**2)
  71      70     (pi*342000675.0**2)
  72      73     (pi*342500675.0**2)
  73      72     (pi*342500675.0**2)
  74      75     (pi*343000675.0**2)
  75      74     (pi*343000675.0**2)
  76      77     (pi*343500675.0**2)
  77      76     (pi*343500675.0**2)
  78      79     (pi*344000675.0**2)
  79      78     (pi*344000675.0**2)
  80      81     (pi*344500675.0**2)
  81      80     (pi*344500675.0**2)
  82      83     (pi*345000675.0**2)
  83      82     (pi*345000675.0**2)
  84      85     (pi*345500675.0**2)
  85      84     (pi*345500675.0**2)
  86      87     (pi*346000675.0**2)
  87      86     (pi*346000675.0**2)
  88      89     (pi*346500675.0**2)
  89      88     (pi*346500675.0**2)
  90      91     (pi*347000675.0**2)
  91      90     (pi*347000675.0**2)
  92      93     (pi*347500675.0**2)
  93      92     (pi*347500675.0**2)
  94      95     (pi*348000675.0**2)
  95      94     (pi*348000675.0**2)
  96      97     (pi*348500675.0**2)
  97      96     (pi*348500675.0**2)
  98      99     (pi*349000675.0**2)
  99      98     (pi*349000675.0**2)
  100     101    (pi*349500675.0**2)
  101     100    (pi*349500675.0**2)
  102     103    (pi*350000675.0**2)
  103     102    (pi*350000675.0**2)
  104     105    (pi*350500675.0**2)
  105     104    (pi*350500675.0**2)
e-type = 3
ne = 50
emin = 3
emax = 3E5
part =  triton 3he
unit = 5
a-type = -2
na = 3
amin = 0
amax = 90
axis = reg
output = a-curr
file = flux_results_triton_he3.dat

[T-cross]
mesh = reg
reg = 126
 r-in   r-out   area
  3       4     (pi*338234250.0**2)
```

```
4        3     (pi*338234250.0**2)
4        5     (pi*338234275.0**2)
5        4     (pi*338234275.0**2)
5        6     (pi*338234300.0**2)
6        5     (pi*338234300.0**2)
6        7     (pi*338234325.0**2)
7        6     (pi*338234325.0**2)
7        8     (pi*338234350.0**2)
8        7     (pi*338234350.0**2)
8        9     (pi*338234375.0**2)
9        8     (pi*338234375.0**2)
9       10     (pi*338234400.0**2)
10       9     (pi*338234400.0**2)
10      11     (pi*338234425.0**2)
11      10     (pi*338234425.0**2)
11      12     (pi*338234450.0**2)
12      11     (pi*338234450.0**2)
12      13     (pi*338234475.0**2)
13      12     (pi*338234475.0**2)
13      14     (pi*338234500.0**2)
14      13     (pi*338234500.0**2)
14      15     (pi*338234525.0**2)
15      14     (pi*338234525.0**2)
15      16     (pi*338234550.0**2)
16      15     (pi*338234550.0**2)
16      17     (pi*338234575.0**2)
17      16     (pi*338234575.0**2)
17      18     (pi*338234600.0**2)
18      17     (pi*338234600.0**2)
18      19     (pi*338234625.0**2)
19      18     (pi*338234625.0**2)
19      20     (pi*338234650.0**2)
20      19     (pi*338234650.0**2)
20      21     (pi*338234675.0**2)
21      20     (pi*338234675.0**2)
21      22     (pi*338234700.0**2)
22      21     (pi*338234700.0**2)
22      23     (pi*338234725.0**2)
23      22     (pi*338234725.0**2)
23      24     (pi*338234750.0**2)
24      23     (pi*338234750.0**2)
24      25     (pi*338234775.0**2)
25      24     (pi*338234775.0**2)
25      26     (pi*338234800.0**2)
26      25     (pi*338234800.0**2)
26      27     (pi*338268425.0**2)
27      26     (pi*338268425.0**2)
28      29     (pi*338336950.0**2)
29      28     (pi*338336950.0**2)
30      31     (pi*338408075.0**2)
31      30     (pi*338408075.0**2)
32      33     (pi*338481962.5**2)
33      32     (pi*338481962.5**2)
34      35     (pi*338558862.5**2)
35      34     (pi*338558862.5**2)
36      37     (pi*338639025.0**2)
37      36     (pi*338639025.0**2)
38      39     (pi*338722725.0**2)
39      38     (pi*338722725.0**2)
40      41     (pi*338810300.0**2)
41      40     (pi*338810300.0**2)
42      43     (pi*338902125.0**2)
43      42     (pi*338902125.0**2)
44      45     (pi*338998637.5**2)
45      44     (pi*338998637.5**2)
46      47     (pi*339100362.5**2)
47      46     (pi*339100362.5**2)
48      49     (pi*339208250.0**2)
49      48     (pi*339208250.0**2)
50      51     (pi*339323600.0**2)
51      50     (pi*339323600.0**2)
52      53     (pi*339447900.0**2)
53      52     (pi*339447900.0**2)
54      55     (pi*339583087.5**2)
55      54     (pi*339583087.5**2)
56      57     (pi*339731712.5**2)
57      56     (pi*339731712.5**2)
```

```
  58      59     (pi*339898025.0**2)
  59      58     (pi*339898025.0**2)
  60      61     (pi*340088637.5**2)
  61      60     (pi*340088637.5**2)
  62      63     (pi*340314225.0**2)
  63      62     (pi*340314225.0**2)
  64      65     (pi*340593962.5**2)
  65      64     (pi*340593962.5**2)
  66      67     (pi*341000562.5**2)
  67      66     (pi*341000562.5**2)
  68      69     (pi*341500675.0**2)
  69      68     (pi*341500675.0**2)
  70      71     (pi*342000675.0**2)
  71      70     (pi*342000675.0**2)
  72      73     (pi*342500675.0**2)
  73      72     (pi*342500675.0**2)
  74      75     (pi*343000675.0**2)
  75      74     (pi*343000675.0**2)
  76      77     (pi*343500675.0**2)
  77      76     (pi*343500675.0**2)
  78      79     (pi*344000675.0**2)
  79      78     (pi*344000675.0**2)
  80      81     (pi*344500675.0**2)
  81      80     (pi*344500675.0**2)
  82      83     (pi*345000675.0**2)
  83      82     (pi*345000675.0**2)
  84      85     (pi*345500675.0**2)
  85      84     (pi*345500675.0**2)
  86      87     (pi*346000675.0**2)
  87      86     (pi*346000675.0**2)
  88      89     (pi*346500675.0**2)
  89      88     (pi*346500675.0**2)
  90      91     (pi*347000675.0**2)
  91      90     (pi*347000675.0**2)
  92      93     (pi*347500675.0**2)
  93      92     (pi*347500675.0**2)
  94      95     (pi*348000675.0**2)
  95      94     (pi*348000675.0**2)
  96      97     (pi*348500675.0**2)
  97      96     (pi*348500675.0**2)
  98      99     (pi*349000675.0**2)
  99      98     (pi*349000675.0**2)
  100     101    (pi*349500675.0**2)
  101     100    (pi*349500675.0**2)
  102     103    (pi*350000675.0**2)
  103     102    (pi*350000675.0**2)
  104     105    (pi*350500675.0**2)
  105     104    (pi*350500675.0**2)
e-type = 3
ne = 50
emin = 4
emax = 4E5
part = alpha
unit = 5
a-type = -2
na = 3
amin = 0
amax = 90
axis = reg
output = a-curr
file = flux_results_alpha.dat

[T-cross]
mesh = reg
reg = 126
 r-in   r-out   area
  3       4     (pi*338234250.0**2)
  4       3     (pi*338234250.0**2)
  4       5     (pi*338234275.0**2)
  5       4     (pi*338234275.0**2)
  5       6     (pi*338234300.0**2)
  6       5     (pi*338234300.0**2)
  6       7     (pi*338234325.0**2)
  7       6     (pi*338234325.0**2)
  7       8     (pi*338234350.0**2)
  8       7     (pi*338234350.0**2)
  8       9     (pi*338234375.0**2)
  9       8     (pi*338234375.0**2)
  9      10     (pi*338234400.0**2)
  10      9     (pi*338234400.0**2)
```

```
10      11      (pi*338234425.0**2)
11      10      (pi*338234425.0**2)
11      12      (pi*338234450.0**2)
12      11      (pi*338234450.0**2)
12      13      (pi*338234475.0**2)
13      12      (pi*338234475.0**2)
13      14      (pi*338234500.0**2)
14      13      (pi*338234500.0**2)
14      15      (pi*338234525.0**2)
15      14      (pi*338234525.0**2)
15      16      (pi*338234550.0**2)
16      15      (pi*338234550.0**2)
16      17      (pi*338234575.0**2)
17      16      (pi*338234575.0**2)
17      18      (pi*338234600.0**2)
18      17      (pi*338234600.0**2)
18      19      (pi*338234625.0**2)
19      18      (pi*338234625.0**2)
19      20      (pi*338234650.0**2)
20      19      (pi*338234650.0**2)
20      21      (pi*338234675.0**2)
21      20      (pi*338234675.0**2)
21      22      (pi*338234700.0**2)
22      21      (pi*338234700.0**2)
22      23      (pi*338234725.0**2)
23      22      (pi*338234725.0**2)
23      24      (pi*338234750.0**2)
24      23      (pi*338234750.0**2)
24      25      (pi*338234775.0**2)
25      24      (pi*338234775.0**2)
25      26      (pi*338234800.0**2)
26      25      (pi*338234800.0**2)
26      27      (pi*338268425.0**2)
27      26      (pi*338268425.0**2)
28      29      (pi*338336950.0**2)
29      28      (pi*338336950.0**2)
30      31      (pi*338408075.0**2)
31      30      (pi*338408075.0**2)
32      33      (pi*338481962.5**2)
33      32      (pi*338481962.5**2)
34      35      (pi*338558862.5**2)
35      34      (pi*338558862.5**2)
36      37      (pi*338639025.0**2)
37      36      (pi*338639025.0**2)
38      39      (pi*338722725.0**2)
39      38      (pi*338722725.0**2)
40      41      (pi*338810300.0**2)
41      40      (pi*338810300.0**2)
42      43      (pi*338902125.0**2)
43      42      (pi*338902125.0**2)
44      45      (pi*338998637.5**2)
45      44      (pi*338998637.5**2)
46      47      (pi*339100362.5**2)
47      46      (pi*339100362.5**2)
48      49      (pi*339208250.0**2)
49      48      (pi*339208250.0**2)
50      51      (pi*339323600.0**2)
51      50      (pi*339323600.0**2)
52      53      (pi*339447900.0**2)
53      52      (pi*339447900.0**2)
54      55      (pi*339583087.5**2)
55      54      (pi*339583087.5**2)
56      57      (pi*339731712.5**2)
57      56      (pi*339731712.5**2)
58      59      (pi*339898025.0**2)
59      58      (pi*339898025.0**2)
60      61      (pi*340088637.5**2)
61      60      (pi*340088637.5**2)
62      63      (pi*340314225.0**2)
63      62      (pi*340314225.0**2)
64      65      (pi*340593962.5**2)
65      64      (pi*340593962.5**2)
66      67      (pi*341000562.5**2)
67      66      (pi*341000562.5**2)
68      69      (pi*341500675.0**2)
69      68      (pi*341500675.0**2)
70      71      (pi*342000675.0**2)
```

```
  71      70     (pi*342000675.0**2)
  72      73     (pi*342500675.0**2)
  73      72     (pi*342500675.0**2)
  74      75     (pi*343000675.0**2)
  75      74     (pi*343000675.0**2)
  76      77     (pi*343500675.0**2)
  77      76     (pi*343500675.0**2)
  78      79     (pi*344000675.0**2)
  79      78     (pi*344000675.0**2)
  80      81     (pi*344500675.0**2)
  81      80     (pi*344500675.0**2)
  82      83     (pi*345000675.0**2)
  83      82     (pi*345000675.0**2)
  84      85     (pi*345500675.0**2)
  85      84     (pi*345500675.0**2)
  86      87     (pi*346000675.0**2)
  87      86     (pi*346000675.0**2)
  88      89     (pi*346500675.0**2)
  89      88     (pi*346500675.0**2)
  90      91     (pi*347000675.0**2)
  91      90     (pi*347000675.0**2)
  92      93     (pi*347500675.0**2)
  93      92     (pi*347500675.0**2)
  94      95     (pi*348000675.0**2)
  95      94     (pi*348000675.0**2)
  96      97     (pi*348500675.0**2)
  97      96     (pi*348500675.0**2)
  98      99     (pi*349000675.0**2)
  99      98     (pi*349000675.0**2)
  100     101    (pi*349500675.0**2)
  101     100    (pi*349500675.0**2)
  102     103    (pi*350000675.0**2)
  103     102    (pi*350000675.0**2)
  104     105    (pi*350500675.0**2)
  105     104    (pi*350500675.0**2)
e-type = 3
ne = 50
emin = 1
emax = 1E5
part = electron positron muon+ muon-
unit = 5
a-type = -2
na = 3
amin = 0
amax = 90
axis = reg
output = a-curr
file = flux_results_electron_muon.dat

[T-cross]
mesh = reg
reg = 126
 r-in   r-out   area
  3       4     (pi*338234250.0**2)
  4       3     (pi*338234250.0**2)
  4       5     (pi*338234275.0**2)
  5       4     (pi*338234275.0**2)
  5       6     (pi*338234300.0**2)
  6       5     (pi*338234300.0**2)
  6       7     (pi*338234325.0**2)
  7       6     (pi*338234325.0**2)
  7       8     (pi*338234350.0**2)
  8       7     (pi*338234350.0**2)
  8       9     (pi*338234375.0**2)
  9       8     (pi*338234375.0**2)
  9      10     (pi*338234400.0**2)
  10      9     (pi*338234400.0**2)
  10     11     (pi*338234425.0**2)
  11     10     (pi*338234425.0**2)
  11     12     (pi*338234450.0**2)
  12     11     (pi*338234450.0**2)
  12     13     (pi*338234475.0**2)
  13     12     (pi*338234475.0**2)
  13     14     (pi*338234500.0**2)
  14     13     (pi*338234500.0**2)
  14     15     (pi*338234525.0**2)
  15     14     (pi*338234525.0**2)
  15     16     (pi*338234550.0**2)
  16     15     (pi*338234550.0**2)
  16     17     (pi*338234575.0**2)
```

```
17      16      (pi*338234575.0**2)
17      18      (pi*338234600.0**2)
18      17      (pi*338234600.0**2)
18      19      (pi*338234625.0**2)
19      18      (pi*338234625.0**2)
19      20      (pi*338234650.0**2)
20      19      (pi*338234650.0**2)
20      21      (pi*338234675.0**2)
21      20      (pi*338234675.0**2)
21      22      (pi*338234700.0**2)
22      21      (pi*338234700.0**2)
22      23      (pi*338234725.0**2)
23      22      (pi*338234725.0**2)
23      24      (pi*338234750.0**2)
24      23      (pi*338234750.0**2)
24      25      (pi*338234775.0**2)
25      24      (pi*338234775.0**2)
25      26      (pi*338234800.0**2)
26      25      (pi*338234800.0**2)
26      27      (pi*338268425.0**2)
27      26      (pi*338268425.0**2)
28      29      (pi*338336950.0**2)
29      28      (pi*338336950.0**2)
30      31      (pi*338408075.0**2)
31      30      (pi*338408075.0**2)
32      33      (pi*338481962.5**2)
33      32      (pi*338481962.5**2)
34      35      (pi*338558862.5**2)
35      34      (pi*338558862.5**2)
36      37      (pi*338639025.0**2)
37      36      (pi*338639025.0**2)
38      39      (pi*338722725.0**2)
39      38      (pi*338722725.0**2)
40      41      (pi*338810300.0**2)
41      40      (pi*338810300.0**2)
42      43      (pi*338902125.0**2)
43      42      (pi*338902125.0**2)
44      45      (pi*338998637.5**2)
45      44      (pi*338998637.5**2)
46      47      (pi*339100362.5**2)
47      46      (pi*339100362.5**2)
48      49      (pi*339208250.0**2)
49      48      (pi*339208250.0**2)
50      51      (pi*339323600.0**2)
51      50      (pi*339323600.0**2)
52      53      (pi*339447900.0**2)
53      52      (pi*339447900.0**2)
54      55      (pi*339583087.5**2)
55      54      (pi*339583087.5**2)
56      57      (pi*339731712.5**2)
57      56      (pi*339731712.5**2)
58      59      (pi*339898025.0**2)
59      58      (pi*339898025.0**2)
60      61      (pi*340088637.5**2)
61      60      (pi*340088637.5**2)
62      63      (pi*340314225.0**2)
63      62      (pi*340314225.0**2)
64      65      (pi*340593962.5**2)
65      64      (pi*340593962.5**2)
66      67      (pi*341000562.5**2)
67      66      (pi*341000562.5**2)
68      69      (pi*341500675.0**2)
69      68      (pi*341500675.0**2)
70      71      (pi*342000675.0**2)
71      70      (pi*342000675.0**2)
72      73      (pi*342500675.0**2)
73      72      (pi*342500675.0**2)
74      75      (pi*343000675.0**2)
75      74      (pi*343000675.0**2)
76      77      (pi*343500675.0**2)
77      76      (pi*343500675.0**2)
78      79      (pi*344000675.0**2)
79      78      (pi*344000675.0**2)
80      81      (pi*344500675.0**2)
81      80      (pi*344500675.0**2)
82      83      (pi*345000675.0**2)
83      82      (pi*345000675.0**2)
```

```
  84      85     (pi*345500675.0**2)
  85      84     (pi*345500675.0**2)
  86      87     (pi*346000675.0**2)
  87      86     (pi*346000675.0**2)
  88      89     (pi*346500675.0**2)
  89      88     (pi*346500675.0**2)
  90      91     (pi*347000675.0**2)
  91      90     (pi*347000675.0**2)
  92      93     (pi*347500675.0**2)
  93      92     (pi*347500675.0**2)
  94      95     (pi*348000675.0**2)
  95      94     (pi*348000675.0**2)
  96      97     (pi*348500675.0**2)
  97      96     (pi*348500675.0**2)
  98      99     (pi*349000675.0**2)
  99      98     (pi*349000675.0**2)
  100     101    (pi*349500675.0**2)
  101     100    (pi*349500675.0**2)
  102     103    (pi*350000675.0**2)
  103     102    (pi*350000675.0**2)
  104     105    (pi*350500675.0**2)
  105     104    (pi*350500675.0**2)
e-type = 3
ne = 50
emin = 1
emax = 1E5
part = pion+ pion- pion0
unit = 5
a-type = -2
na = 3
amin = 0
amax = 90
axis = reg
output = a-curr
file = flux_results_pion.dat

[END]
```

# Appendix B

# Other Solar Particle Plots

## Datum

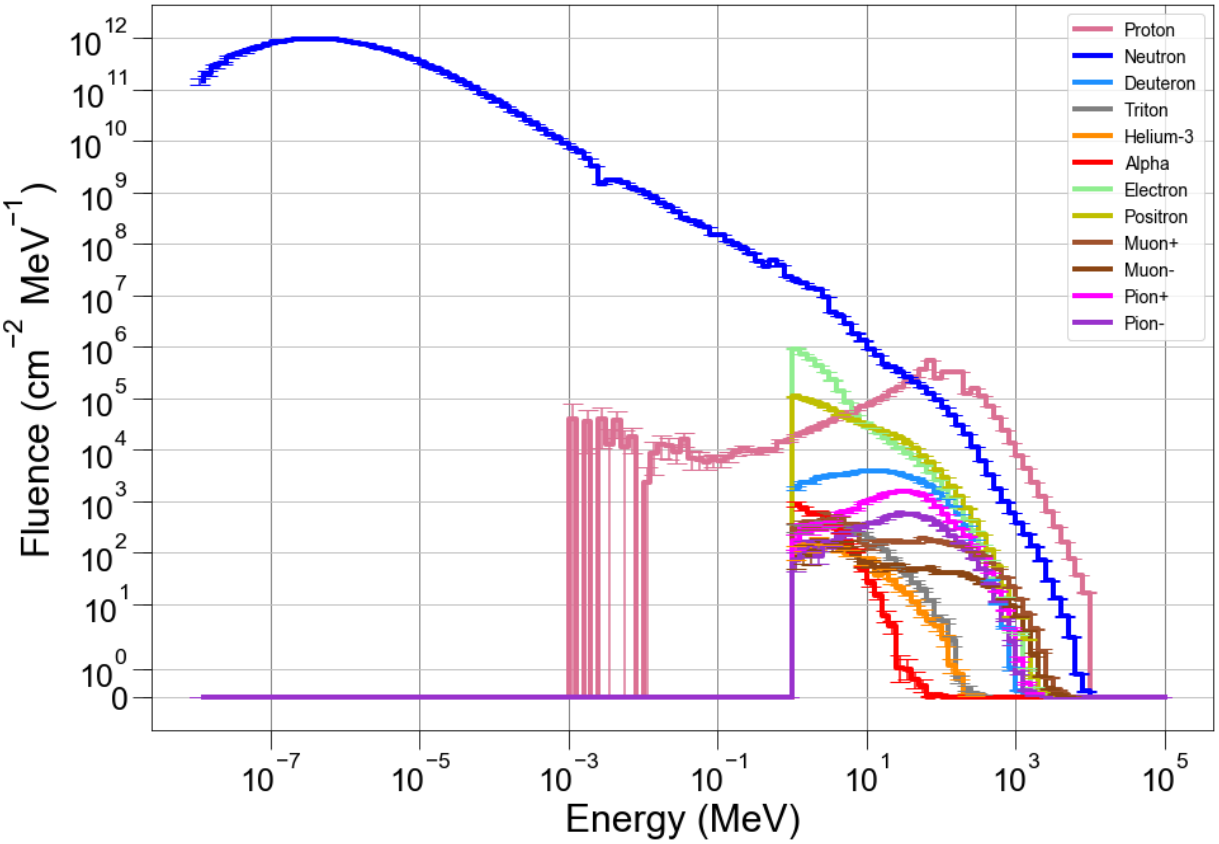


**Figure B.1**: *Total fluences for all tallied particles at 13.7 g cm$^{-2}$ for October 19, 1989, event.*

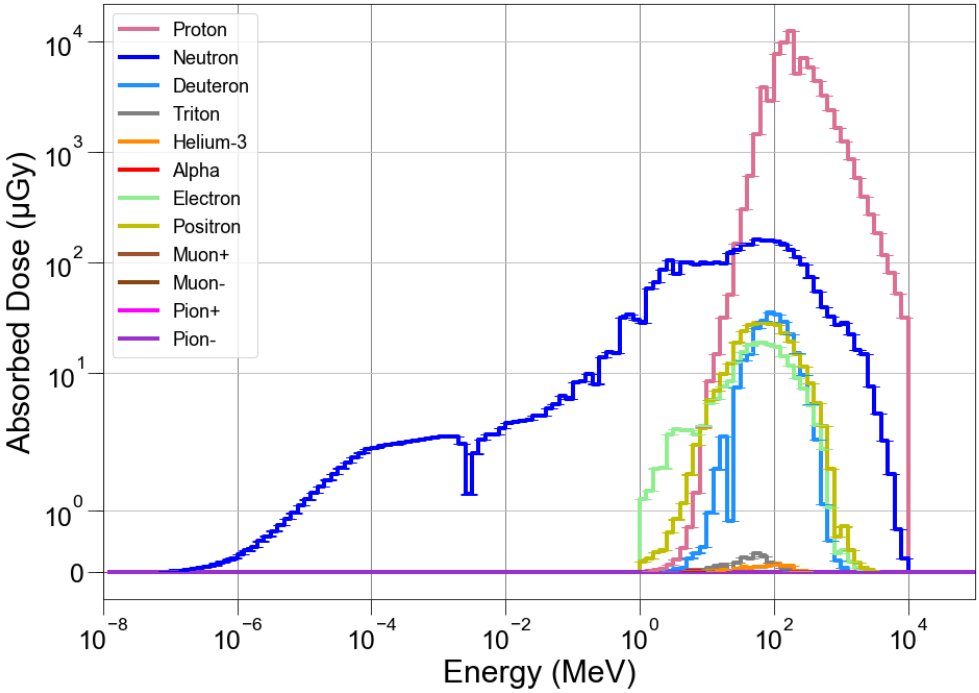


**Figure B.2**: *Absorbed dose for all tallied particles at 13.7 g cm$^{-2}$ for October 19, 1989, event.*

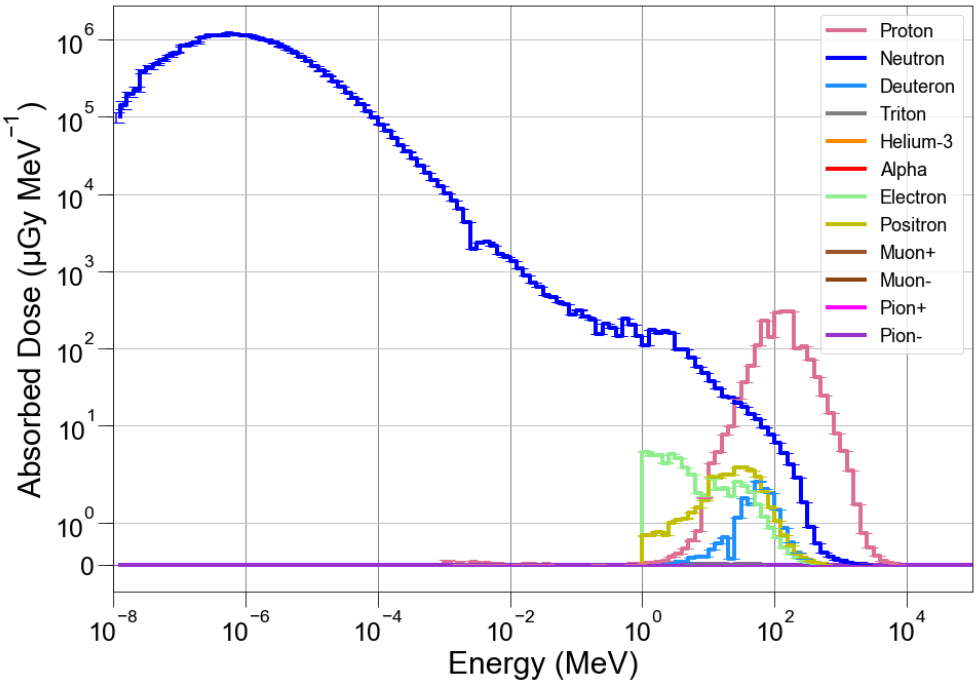


**Figure B.3**: *Absorbed dose per MeV for all tallied particles at 13.7 g cm$^{-2}$ for October 19, 1989, event.*

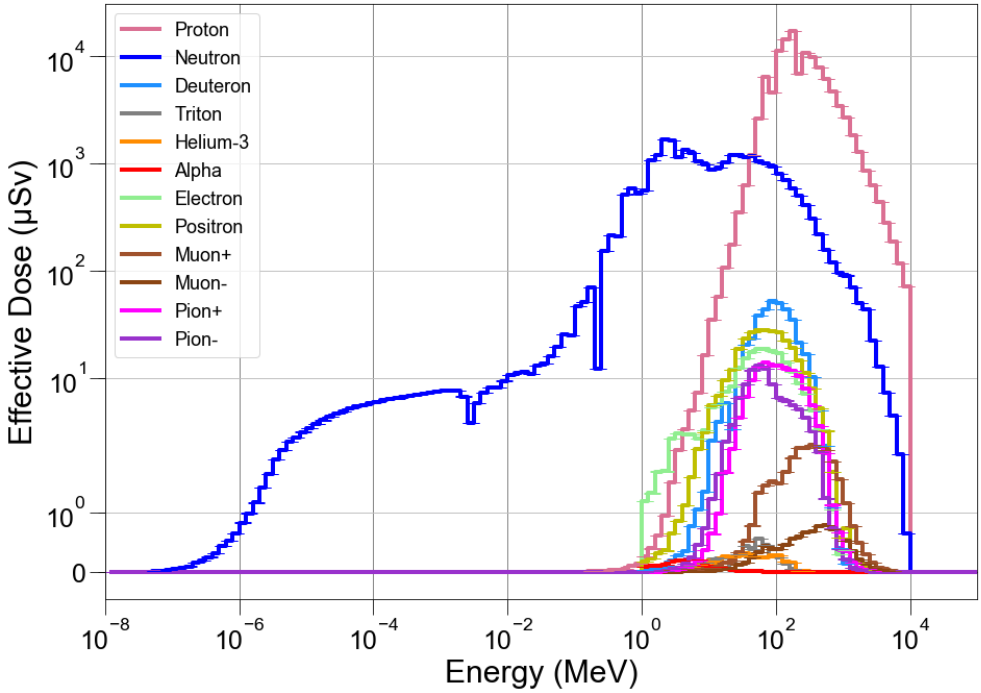


**Figure B.4**: *Effective dose for all tallied particles at 13.7 g cm$^{-2}$ for October 19, 1989, event.*

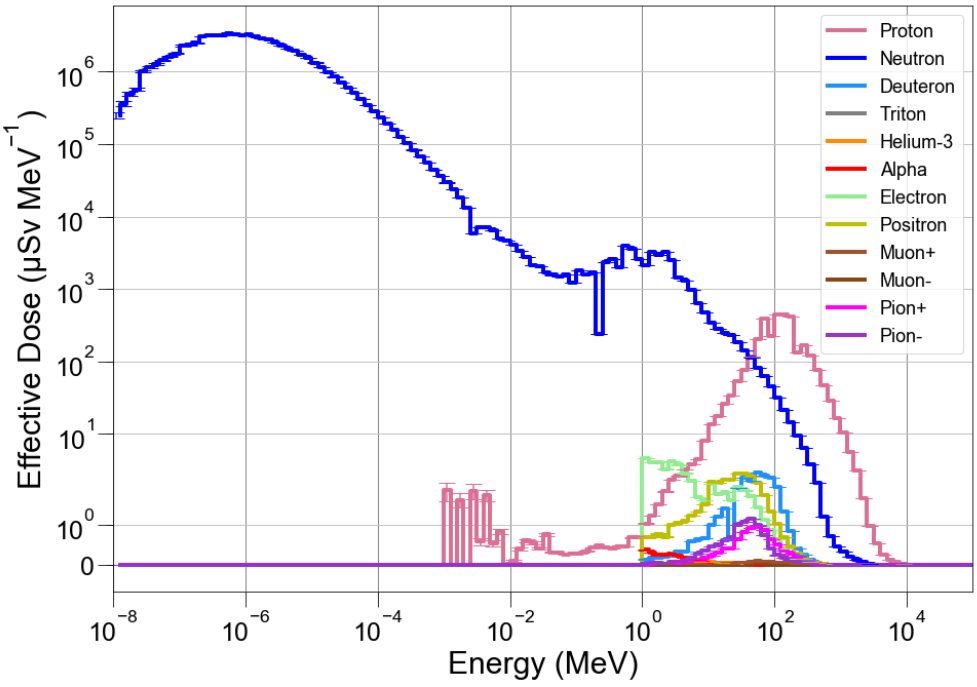


**Figure B.5**: *Effective dose per MeV for all tallied particles at 13.7 g cm$^{-2}$ for October 19, 1989, event.*

# Olympus Mons

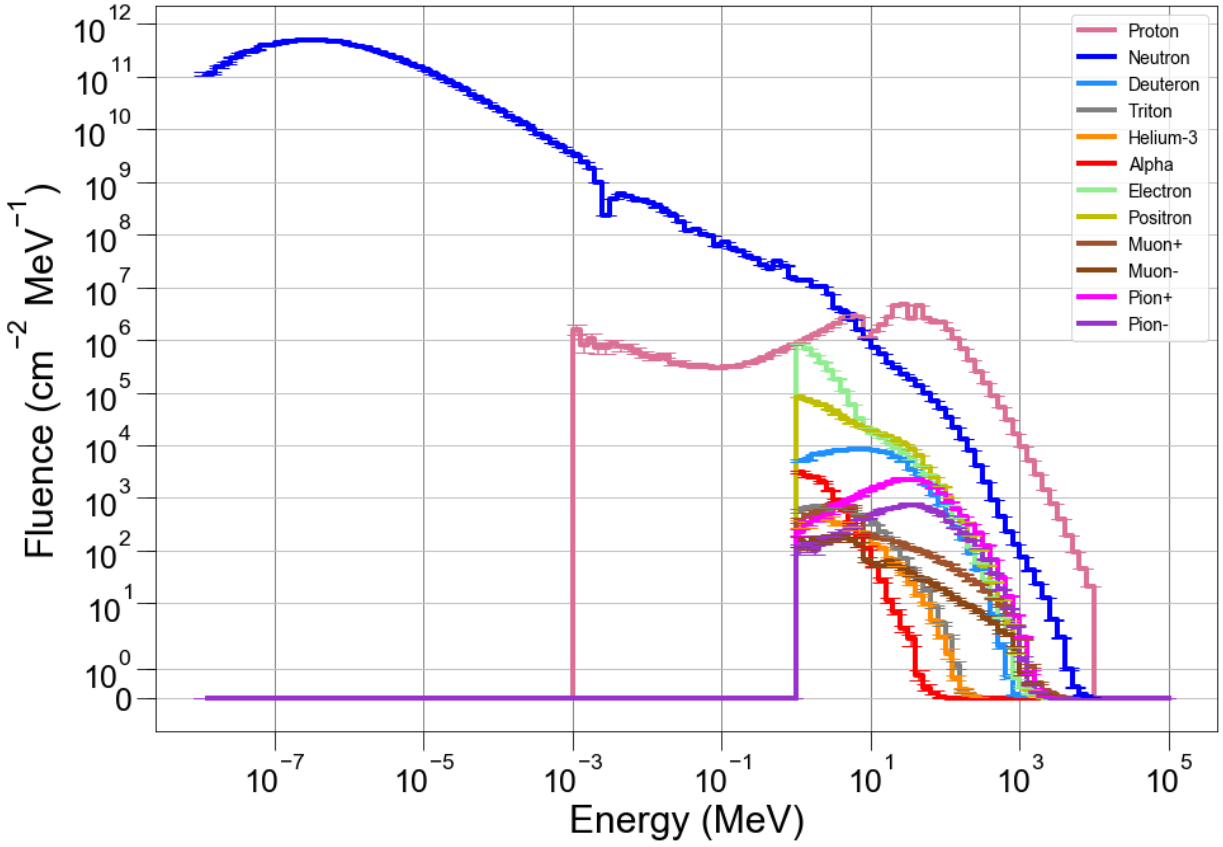


**Figure B.6**: *Total fluences for all tallied particles at 1.62 g cm$^{-2}$ for October 19, 1989, event.*

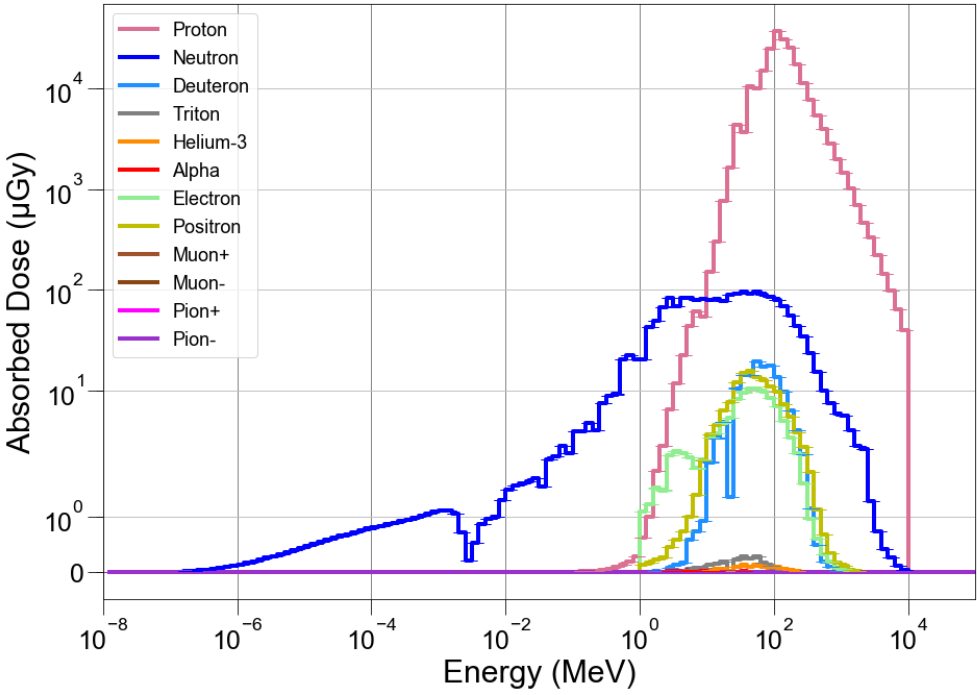


**Figure B.7**: *Absorbed dose for all tallied particles at 1.62 g cm$^{-2}$ for October 19, 1989, event.*

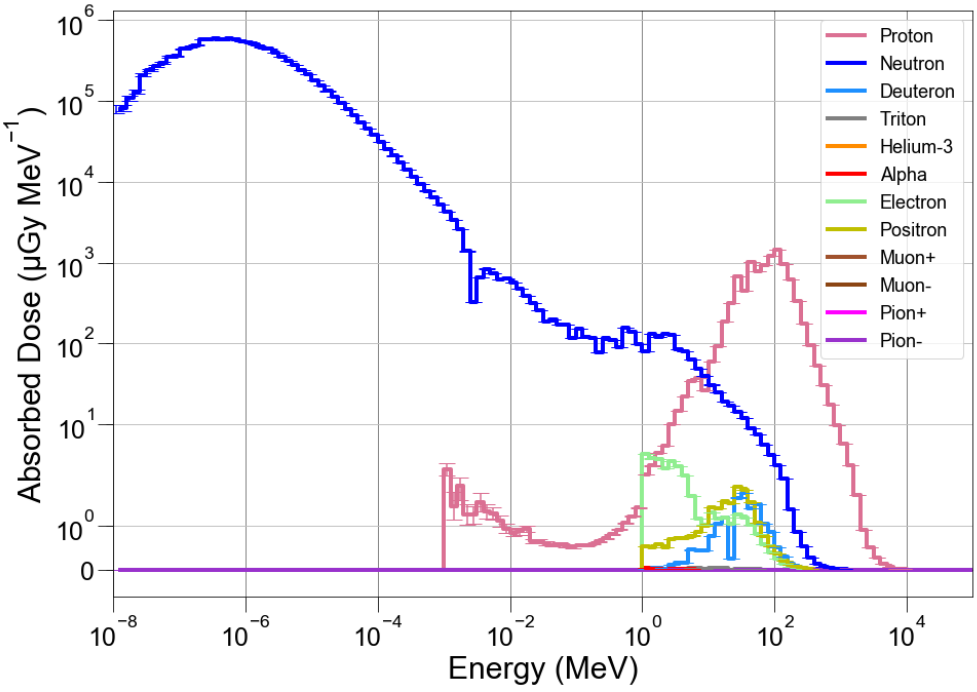


**Figure B.8**: *Absorbed dose per MeV for all tallied particles at 1.62 g cm$^{-2}$ for October 19, 1989, event.*

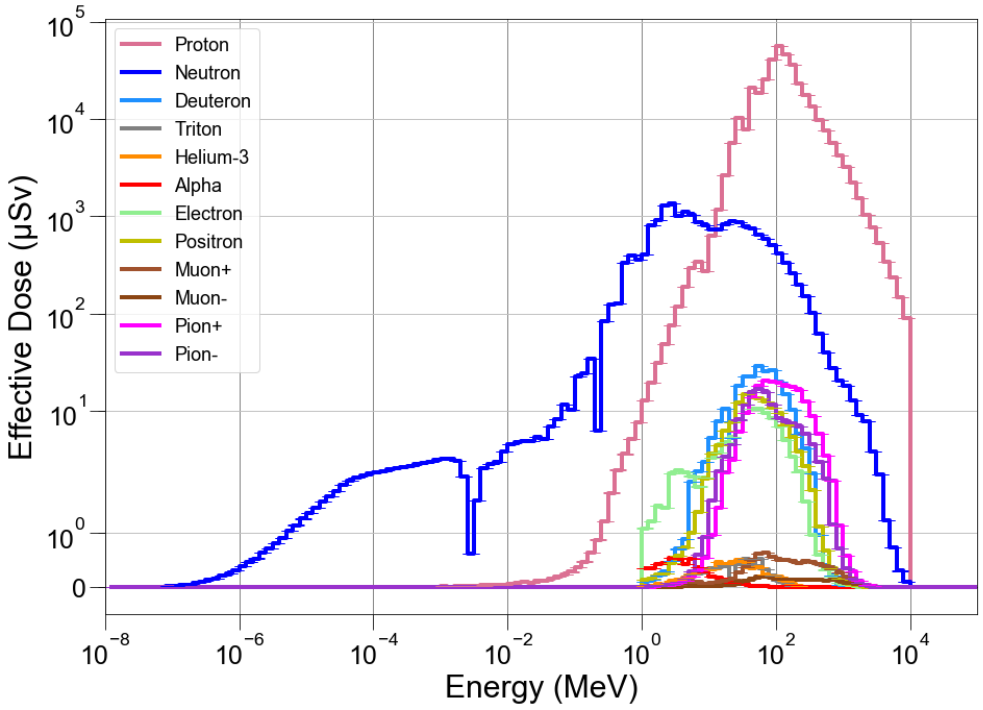


**Figure B.9**: *Effective dose for all tallied particles at 1.62 g cm$^{-2}$ for October 19, 1989, event.*

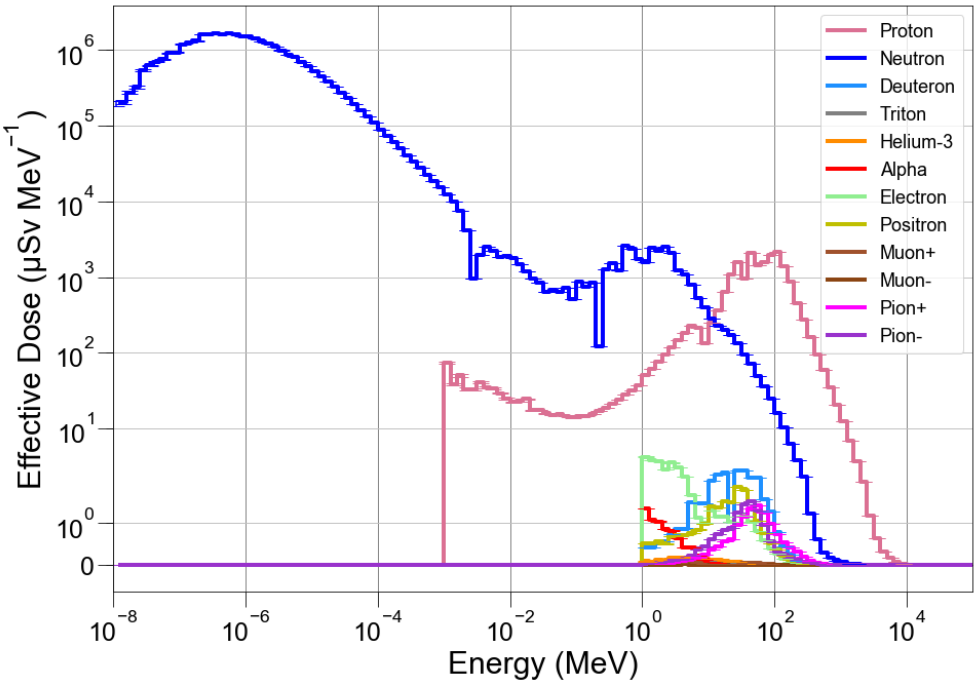


**Figure B.10**: *Effective dose per MeV for all tallied particles at 1.62 g cm$^{-2}$ for October 19, 1989, event.*

# Appendix C

# Comparison of Other GCR Particles

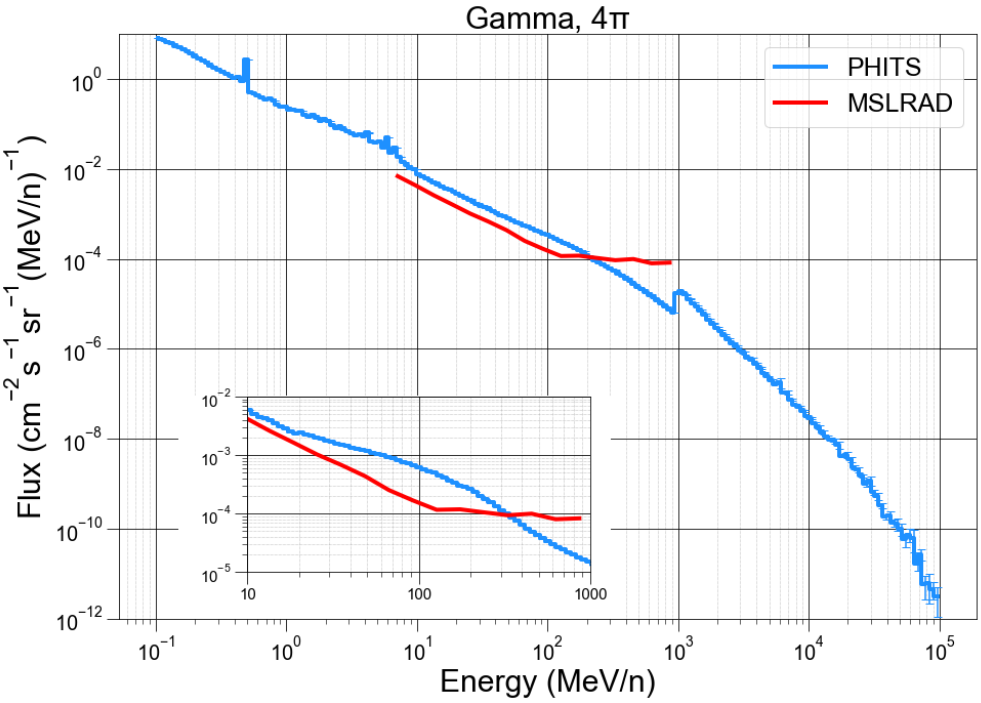


**Figure C.1**: *Comparison of simulated gamma particle flux with MSLRAD.*

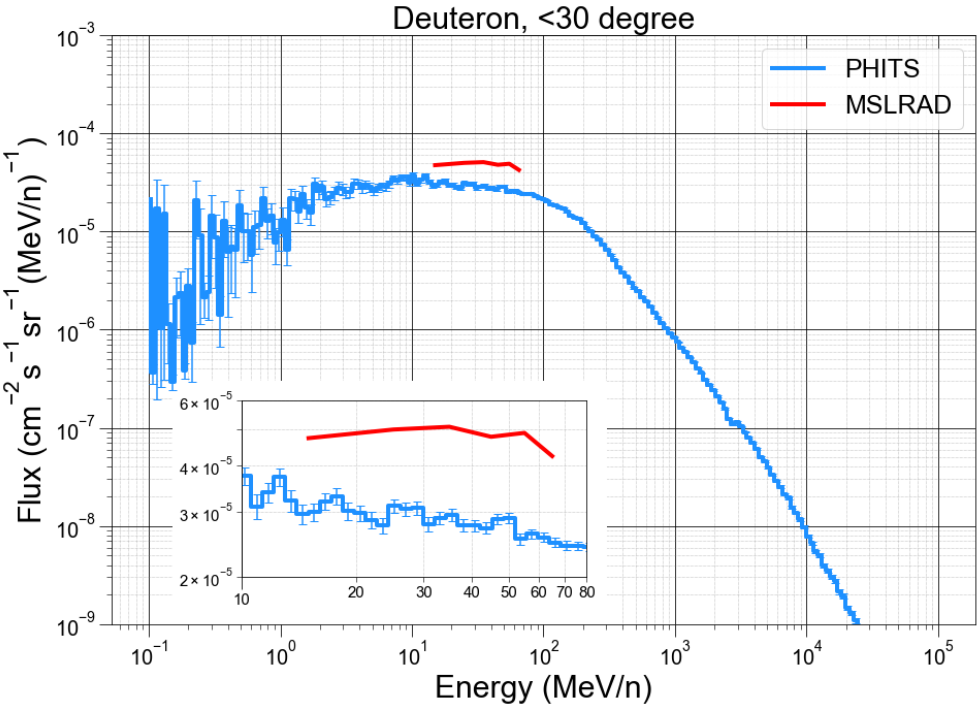


**Figure C.2**: *Comparison of simulated deuteron flux with MSLRAD.*

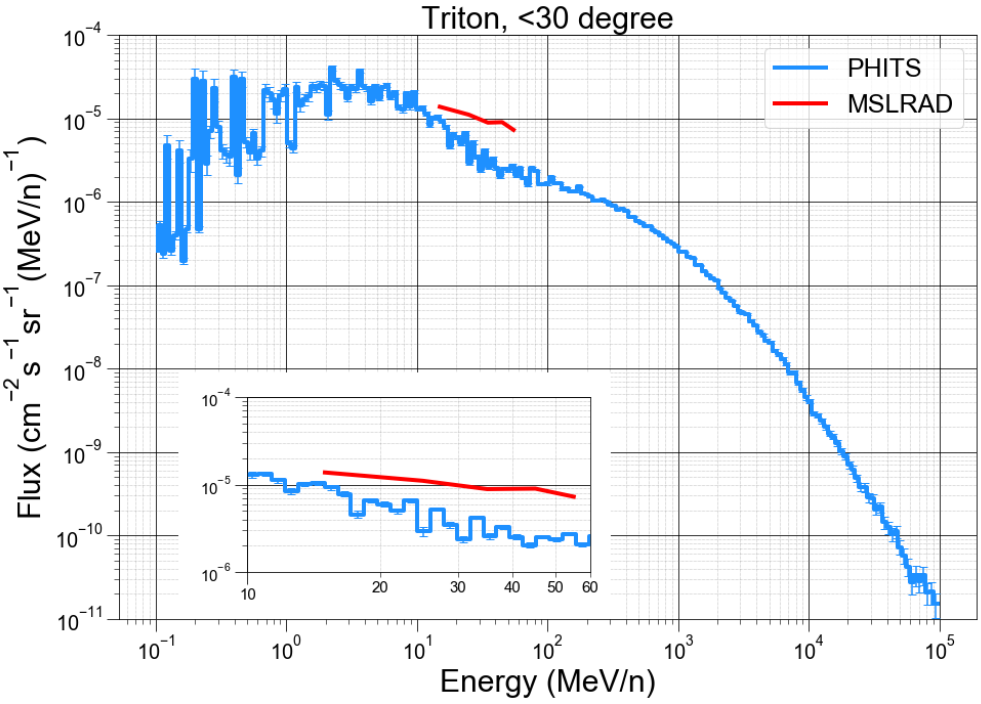


**Figure C.3**: *Comparison of simulated triton flux with MSLRAD.*

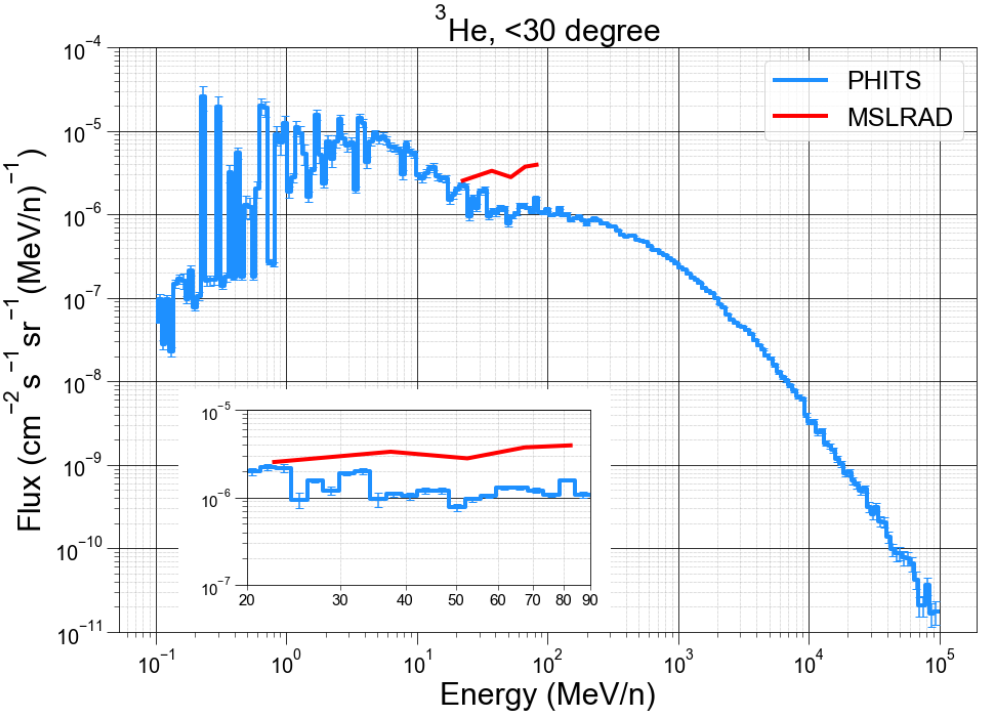


**Figure C.4**: *Comparison of simulated helium-3 flux with MSLRAD.*

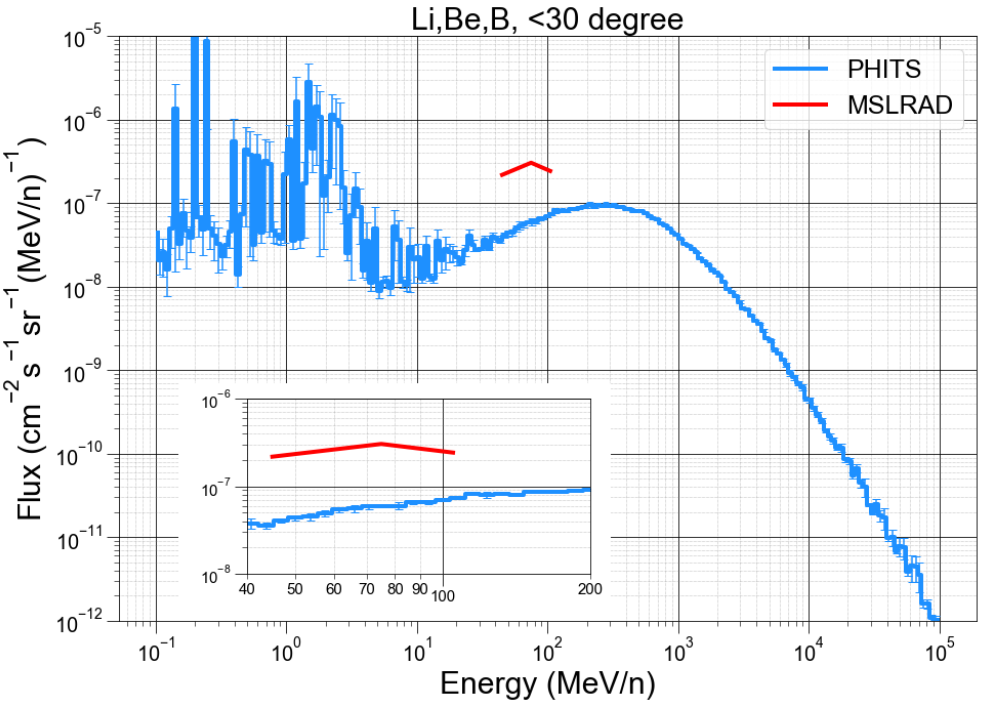


**Figure C.5**: *Comparison of simulated particles Z=3-5 flux with MSLRAD.*

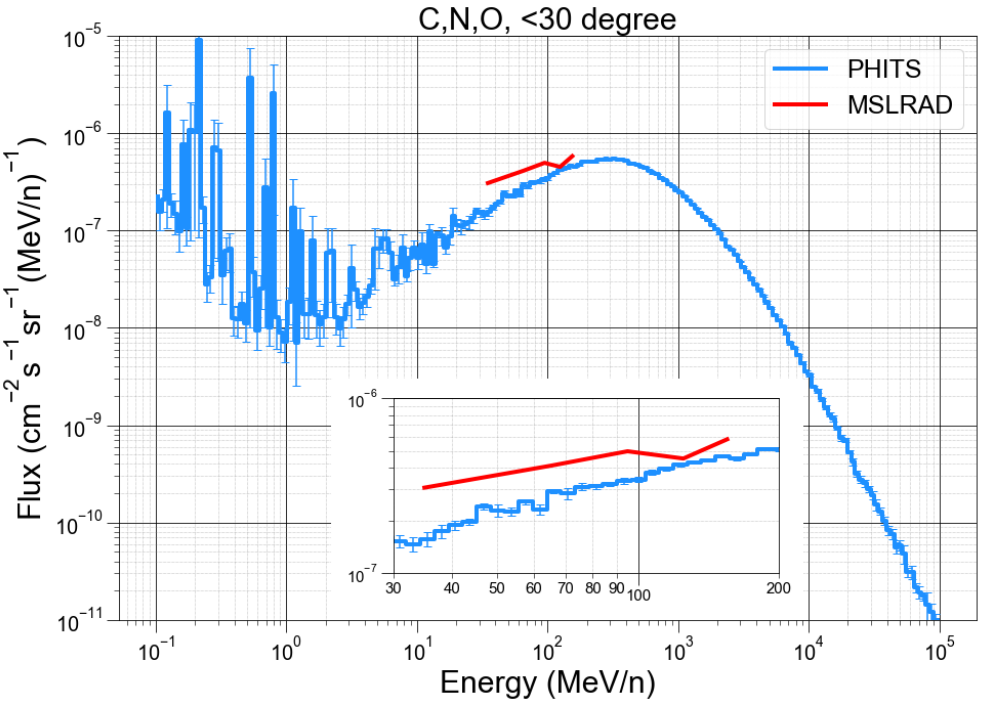


**Figure C.6**: *Comparison of simulated particles Z=6-8 flux with MSLRAD.*

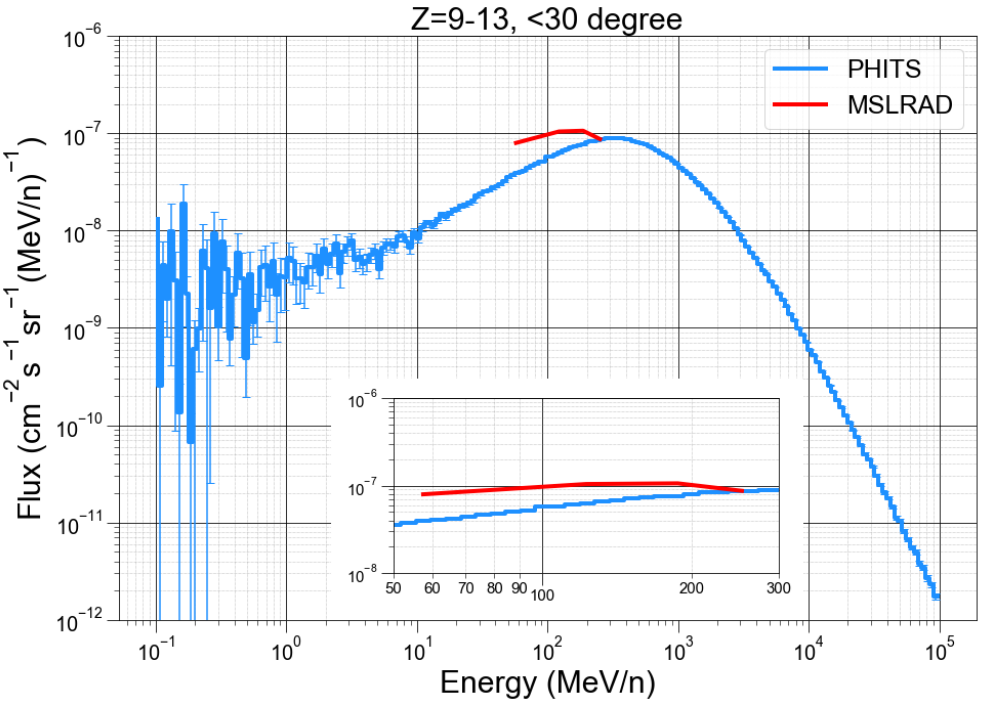


**Figure C.7**: *Comparison of simulated particles Z=9-13 flux with MSLRAD.*

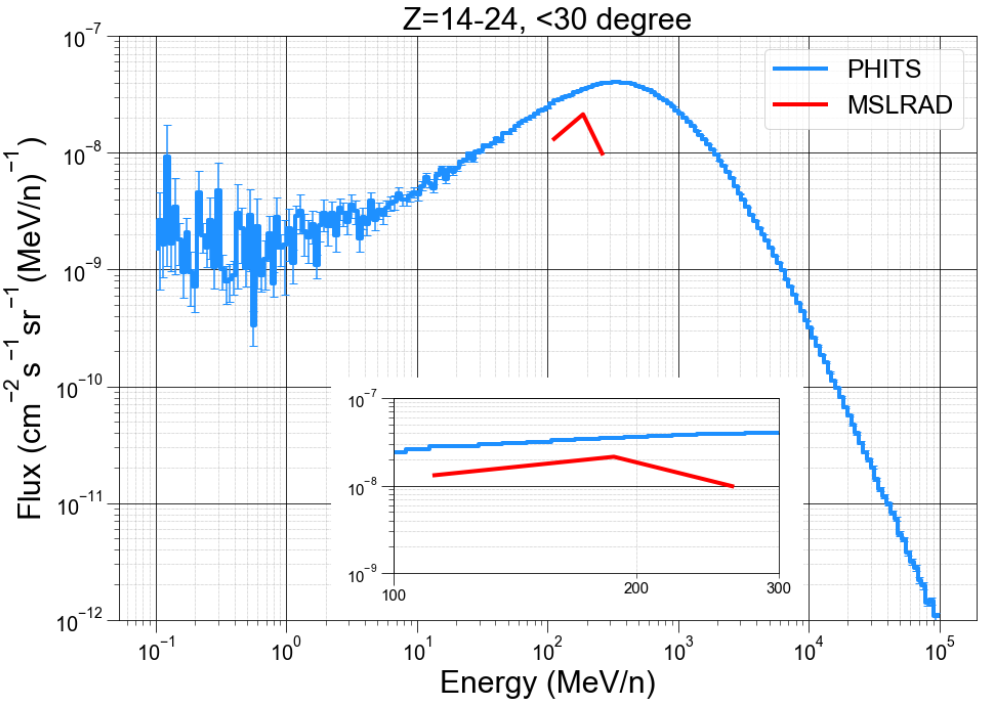


**Figure C.8**: *Comparison of simulated particles Z=14-24 flux with MSLRAD.*

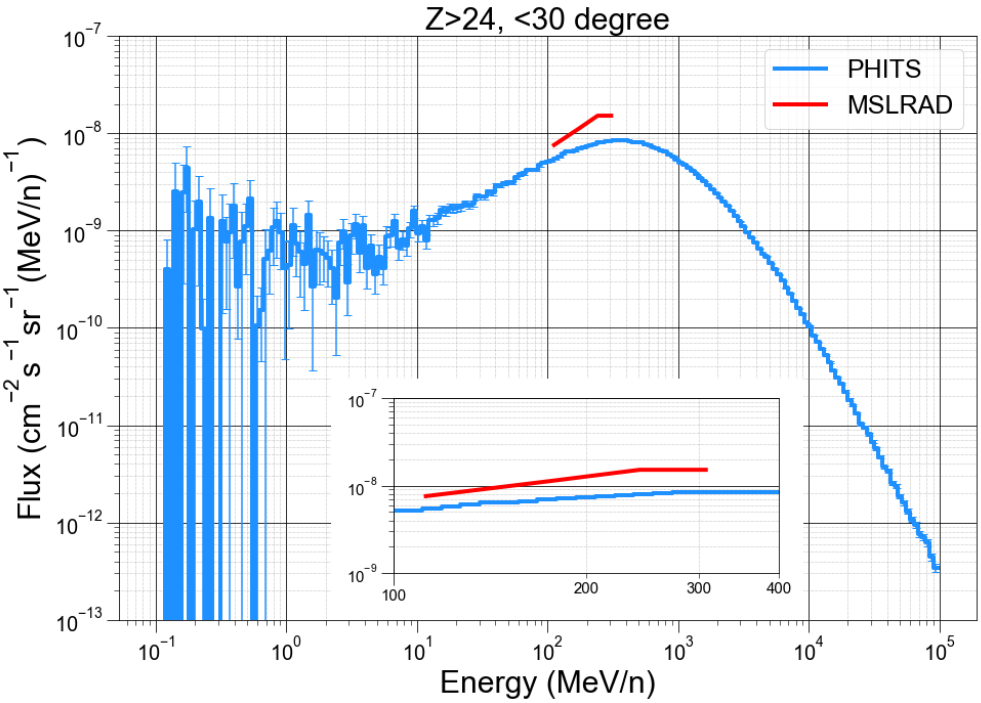


**Figure C.9**: *Comparison of simulated particles Z>24 flux with MSLRAD.*

# Appendix D

# Example Weibull Fitting

```
E=[0.009950331,0.246860078,0.470003629,0.703097511,0.963174318,1.272565596,1.515127233, \
   1.691939134,1.882513832,2.069391206,2.282382386,2.508785924,2.694627181,2.853592506, \
   3.086029912,3.271468275,3.458837161,3.659965444,3.845241972,4.039008017,4.270396506, \
   4.496582246,4.600057137,4.734266759,4.916397872,5.109394066,5.309949451,5.614003635,\
   5.987054839]

# Load the Data from Excel and Text
df = pd.read_excel("Weibull_Fluence.xlsx")
#E = pd.read_excel('Weibull_Energy.xlsx')
G=np.genfromtxt('Weib_Date_Time.txt', dtype=None)

E = np.exp(E)

# Choose Range of Wanted Events
#Wanted_Events=range(1,len(df)+1)
Wanted_Events=[106,221,303]


ChiData=[]
for Event in Wanted_Events:
    # Load Data and Scale it Accordingly
    y = df.loc[Event]
    y1 = y[y>0]
    Ey = E[0:len(y1)]
#    Ey = Ey[y>0]

    # Guess on the Weibull Parameters
    print (y1)
    Z=(y1[0],1,1)

    # Energies to evaluate function once parameters are known
    E2=np.logspace(0,5,500)

    ###############################################################################
    ####                    Define the Weibull Function
    ###############################################################################
    def f(x, q, k, a):
        return q*k*a*(x**(a-1))*np.exp(-((k*x)**a))
    y1=np.exp(y1[1:])

    # Least Squares Error Minimization Based on the Log of the Data
    def err(params, x):
        # Lower Bound for Curve fit Energy Cuttoff
        LB=0
#        if len(y1)>14:
```

```
#            LB=10
        q, k, a = params
        e=0
        y4 = f(x, q, k, a)
        for i in range(LB,len(y1)):
            e+=(np.log(y1[i])-np.log(y4[i]))**2
        return e

    # Chi Squared Minimization Based on the Data
    def chi(params, x):
        # Lower Bound for Curve fit Energy Cuttoff
        LB=0
#        if len(y1)>14:
#            LB=10
        q, k, a = params
        chi=0
        y4 = f(x, q, k, a)
        print (len(y4))
        print (len(y1))
        for i in range(LB,len(y1)):
            print (i)
            chi+=((np.log(y1[i])-np.log(y4[i]))/np.log(y1[i]))**2
        return chi

    ##############################################################################
    ####   Minimize Parameters and Apply Additional Settings for High Energies
    ##############################################################################
    # Minimize the Functions Based off the Nelder-Mead Method
    # ChiSquared
#    n = minimize(chi,Z,args=Ey, method='Nelder-Mead', tol=1E-12)
    # Standard Weibull
    m = minimize(err,Z,args=Ey, method='Nelder-Mead', tol=1E-12)

    #Append the Chi Squared Fit
    ChiData.append(m.x)
```